EXTERNALLY DISPERSED INTERFEROMETRY FOR TERRESTRIAL EXOPLANET DETECTION

A Dissertation

Presented to the Faculty of the Graduate School

of Cornell University

in Partial Fulfillment of the Requirements for the Degree of

Doctor of Philosophy

by

Philip Steven Muirhead

August 2011

EXTERNALLY DISPERSED INTERFEROMETRY FOR TERRESTRIAL

EXOPLANET DETECTION

Philip Steven Muirhead, Ph.D.

Cornell University 2011

Terrestrial exoplanets are observationally challenging to detect and characterize. Compared to gas giant exoplanets, terrestrial exoplanets introduce significantly smaller radial velocity signals and transit depths on their host stars. The signals are larger for terrestrial exoplanets orbiting M-dwarf stars, which have lower masses and radii than Sun-like F, G and K-type stars, and dominate stellar populations by number. Detecting exoplanets around M dwarfs is itself difficult because of their lower luminosities and lower flux at visible wavelengths, where most radial velocity and transit exoplanet surveys operate.

I present here the motivation, development and results from a radial velocity program conducted on M dwarfs using near-infrared wavelengths, where M dwarf spectra peak in flux. To achieve high radial-velocity precision, I have used a technique called externally dispersed interferometry. It involves the combination of an interferometer and a moderate-resolution spectrograph on the 200 inch (5.1 m) Hale Telescope at Palomar Observatory. The TripleSpec Exoplanet Discovery Instrument, or TEDI, is the first such instrument to operate at near-infrared wavelengths.

Our results indicate that contamination by narrow absorption lines introduced by the Earth's atmosphere limit radial velocity performance to that which can detect gas giant planets. I have conducted a survey of nearby M dwarfs, and can rule out with 3σ confidence the presence of short-period gas giant planets in

circular orbits around a few nearby M dwarfs. The results of this experiment direct future extrasolar planet instrumentation toward spectral regions with little telluric contamination and with higher resolution, to detect terrestrial exoplanets orbiting M dwarfs.

BIOGRAPHICAL SKETCH

I was born on January 14th, 1983, in Morristown, New Jersey, the second child of Susan Putnam Muirhead and E. Eric Muirhead, Jr. In August, 1983, when I was seven months old, my family moved to Los Angeles where my father had a teaching position at Chadwick School, a private K-12 school in Palos Verdes Peninsula. I lived in San Pedro until August, 1984, when my family moved to the Chadwick School campus. I attended pre-school at Broadacres from 1986 to 1988, and attended kindergarden, first and second grade at Chadwick. In June of 1989 my family moved to nearby Redondo Beach. In June of 1991, when I was 8 years old, my family moved to a suburb of Houston, Texas.

I lived in the Olde Oaks neighborhood in northwest Harris Country, and attended Oak Creek Elementary, Wells Middle School and Westfield High School from 1991 to 2001. Notable accomplishments include performing trombone in the Westfield High School Band, which won the Texas State Marching Championship in 1998 with a marching rendition of Leonard Bernstein's *Mass*, and won the Texas Music Educators Association Honor Band competition with a performance of Paul Hindemith's *Symphony in B-flat* in 1999. I do not recall being particularly interested in physics or astronomy before college; however, I was excited by calculus and statistics which I attribute to having a particularly engaging mathematics teacher, Mr. E. C. Hedstrom.

In 2001, I left Texas to begin undergraduate studies at the University of Michigan in Ann Arbor. I was enrolled in both the Residential College and the Honors Program within the College of Literature, Science and the Arts. I was a member of the Michigan Marching Band for two years, attending the 2006 Citrus Bowl and 2007 Capital One Outback Bowl. I became interested in physics during my first year, and took my first astronomy course during my second

year. By the end of my second year I had declared a double major in *Astronomy and Astrophysics* and *General Physics*. During my third and fourth years in college I worked with Professor John Monnier, assisting with the assembly and software design for the Michigan Infrared Combiner, a beam combiner at the CHARA array at Mt. Wilson Observatory capable of imaging the surfaces of main sequence stars at infrared wavelengths (Monnier et al., 2007). The experience was extremely fun and rewarding, and it convinced me to apply to Ph.D. programs in astronomy.

In 2005, I graduated from Michigan with a Bachelors of Science and moved to Ithaca, New York, to begin a Ph.D program in Astronomy and Space Sciences at Cornell University. I began research with my advisor, James Lloyd, in Spring of 2006. Since then, my Cornell and Ithaca experiences have been deeply rewarding. In 2007 I received a NASA Earth and Space Sciences Graduate Fellowship, supporting my dissertation research for 3 years. In 2009 I received the Cranson W. and Edna B. Shelley Award for Graduate Research in Astronomy. In 2010 I received a Z. Carter Patten '25 Graduate Fellowship, and a New York Space Grant Graduate Fellowship. I publicly defended my dissertation in May of 2011.

For my parents, Eric and Susan, and my brother, Elliot

ACKNOWLEDGEMENTS

in the simulations in this dissertation.

REFEREED PUBLICATIONS

Muirhead, P. S., Edelstein, J., Erskine, D. J., Wright, J. T., Muterspaugh, M. W., Covey, K. R., Wishnow, E. H., Hamren, K., Andelson, P., Kimber, D., Mercer, T., Halverson, S. P., Vanderburg, A., Mondo, D., Czeszumska, A., and Lloyd, J. P., "Precise Stellar Radial Velocities of an M Dwarf with a Michelson Interferometer and a Medium-Resolution Near-Infrared Spectrograph," *PASP in press*.

Miller, A. A., Hillenbrand, L. A., Covey, K. R., Poznanski, D., Silverman, J. M., Kleiser, I. K. W., Rojas-Ayala, B., **Muirhead, P. S.**, Cenko, S. B., Bloom, J. S., Kasliwal, M. M., Filippenko, A. V., Law, N. M., Ofek, E. O., Dekany, R. G., Rahmer, G., Hale, D., Smith, R., Quimby, R. M., Nugent, P., Jacobsen, J., Zolkower, J., Velur, V., Walters, R., Henning, J., Bui, K., McKenna, D., Kulkarni, S. R., Klein, C. R., Kandrashoff, M., and Morton, A., "Evidence for an FU Orionis-like Outburst from a Classical T Tauri Star," *ApJ* **730**, 80–+ (Apr. 2011).

West, A. A., Morgan, D. P., Bochanski, J. J., Andersen, J. M., Bell, K. J., Kowalski, A. F., Davenport, J. R. A., Hawley, S. L., Schmidt, S. J., Bernat, D., Hilton, E. J., **Muirhead, P.**, Covey, K. R., Rojas-Ayala, B., Schlawin, E., Gooding, M., Schluns, K., Dhital, S., Pineda, J. S., and Jones, D. O., "The Sloan Digital Sky Survey Data Release 7 Spectroscopic M Dwarf Catalog. I. Data," *AJ* **141**, 97–+ (Mar. 2011).

Rojas-Ayala, B., Covey, K. R., **Muirhead, P. S.**, and Lloyd, J. P., "Metal-rich M-Dwarf Planet Hosts: Metallicities with K-band Spectra," *ApJL* **720**, L113–L118 (Sept. 2010).

Monnier, J. D., Zhao, M., Pedretti, E., Thureau, N., Ireland, M., **Muirhead, P.**, Berger, J., Millan-Gabet, R., Van Belle, G., ten Brummelaar, T., McAlister, H., Ridgway, S., Turner, N., Sturmann, L., Sturmann, J., and Berger, D., "Imaging the Surface of Altair," *Science* **317**, 342– (July 2007).

NON-REFEREED PUBLICATIONS

Muirhead, P. S., Edelstein, J., Wright, J. T., Erskine, D. J., Muterspaugh, M. W., Covey, K. R., Marckwordt, M. R., Halverson, S., Mondo, D., and Lloyd, J. P., "Precise infrared radial velocimetry with the Triplespec Exoplanet Discovery Instrument: current performance and results," in [*Society of Photo-Optical Instrumentation Engineers (SPIE) Conference Series*], *Society of Photo-Optical Instrumentation Engineers (SPIE) Conference Series* **7735** (July 2010).

Edelstein, J., **Muirhead, P.**, Wright, J., Covey, K., Erskine, D., Muterspaugh, M., Lloyd, J., Halverson, S., Marckwordt, M., and Mondo, D., "Infrared radial velocimetry with TEDI: performance development," in [*Society of Photo-Optical Instrumentation Engineers (SPIE) Conference Series*], *Society of Photo-Optical Instrumentation Engineers (SPIE) Conference Series* **7735** (July 2010).

Muirhead, P. S., Erskine, D. J., Edelstein, J., Barman, T. S., and Lloyd, J. P., "Radial Velocity Precision in the Near-Infrared with T-EDI," in [*Precision Spectroscopy in Astrophysics*], N. C. Santos, L. Pasquini, A. C. M. Correia, & M. Romaniello , ed., 303–304 (2008).

Herter, T. L., Henderson, C. P., Wilson, J. C., Matthews, K. Y., Rahmer, G., Bonati, M., **Muirhead, P. S.**, Adams, J. D., Lloyd, J. P., Skrutskie, M. F., Moon, D., Parshley, S. C., Nelson, M. J., Martinache, F., and Gull, G. E., "The performance of TripleSpec at Palomar," in [*Society of Photo-Optical Instrumentation Engineers (SPIE) Conference Series*], *Society of Photo-Optical Instrumentation Engineers (SPIE) Conference Series* **7014** (Aug. 2008).

Edelstein, J., Muterspaugh, M. W., Erskine, D., Marckwordt, M., Feuerstein, W. M., Mercer, T., Czeszumska, A., Schwer, J., Halverson, S., Lloyd, J. P., **Muirhead, P. S.**, Wright, J. T., and Herter, T., "Dispersed interferometry for infrared exoplanet velocimetry," in [*Society of Photo-Optical Instrumentation Engineers (SPIE) Conference Series*], *Society of Photo-Optical Instrumentation Engineers (SPIE) Conference Series* **7014** (Aug. 2008).

Monnier, J. D., Zhao, M., Pedretti, E., Thureau, N., Ireland, M., **Muirhead, P.**, Berger, J., Millan-Gabet, R., Van Belle, G., ten Brummelaar, T., McAlister, H., Ridgway, S., Turner, N., Sturmann, L., Sturmann, J., Berger, D., Tannirkulam, A., and Blum, J., "Imaging the surface of Altair and a MIRC update," in [*Society of Photo-Optical Instrumentation Engineers (SPIE) Conference Series*], *Society of Photo-Optical Instrumentation Engineers (SPIE) Conference Series* **7013** (July 2008).

Edelstein, J., Muterspaugh, M. W., Erskine, D. J., Feuerstein, W. M., Marckwordt, M., Wishnow, E., Lloyd, J. P., Herter, T., **Muirhead, P.**, Gull, G. E., Henderson, C., and Parshley, S. C., "TEDI: the TripleSpec Exoplanet Discovery Instrument," in [*Society of Photo-Optical Instrumentation Engineers (SPIE) Conference Series*], *Society of Photo-Optical Instrumentation Engineers (SPIE) Conference Series* **6693** (Sept. 2007).

Erskine, D. J., Edelstein, J., Lloyd, J., and **Muirhead, P.**, "Noise studies of externally dispersed interferometry for Doppler velocimetry," in [*Society of Photo-Optical Instrumentation Engineers (SPIE) Conference Series*], *Society of Photo-Optical Instrumentation Engineers (SPIE) Conference Series* **6269** (July 2006).

Berger, D. H., Monnier, J. D., Millan-Gabet, R., ten Brummelaar, T. A., **Muirhead, P.**, Pedretti, E., and Thureau, N., "CHARA Michigan phase-tracker (CHAMP): design and fabrication," in [*Society of Photo-Optical Instrumentation Engineers (SPIE) Conference Series*], *Society of Photo-Optical Instrumentation Engineers (SPIE) Conference Series* **6268** (July 2006).

Monnier, J. D., Pedretti, E., Thureau, N., Berger, J., Millan-Gabet, R., ten Brummelaar, T., McAlister, H., Sturmann, J., Sturmann, L., **Muirhead, P.**, Tannirkulam, A., Webster, S., and Zhao, M., "Michigan Infrared Combiner (MIRC): commissioning results at the CHARA Array," in [*Society of Photo-Optical Instrumentation Engineers (SPIE) Conference Series*], *Society of Photo-Optical Instrumentation Engineers (SPIE) Conference Series* **6268** (July 2006).

SELECTED TALKS

"Precise Radial Velocimetry in the Near-Infrared with T-EDI." Student Talk. *VLTI Summer School: Circumstellar disks and planets at very high angular resolution.* Ofir, Portugal, 28 May - 8 June 2007.

"Precise Radial Velocities in the Infrared with T-EDI." Contributed Talk, member of the Science Organizing Committee. *2009 Palomar Science Meeting.* Pasadena, CA, USA, 30 April - 1 May 2009.

"Precise Radial Velocities in the Infrared with the TripleSpec EDI." Contributed Talk. *New Technologies for Probing the Diversity of Brown Dwarfs and Extrasolar Planets.* Shanghai, China, 19 - 24 July 2009.

"TripleSpec & TEDI." Contributed Talk. *2009 Keck Science Meeting*, Infrared Instrumentation Workshop. Pasadena, CA, USA, 16 - 18 September 2009.

"Precise Near-Infrared Radial Velocities with the TripleSpec Exoplanet Discovery Instrument (TEDI)." Colloquium, Space Sciences Laboratory, University of California. Berkeley, CA, USA, 5 November 2010.

"Precise Near-Infrared Radial Velocities with the TripleSpec Exoplanet Discovery Instrument (TEDI)." Seminar, Center for Exoplanets and Habitable Worlds, The Pennsylvania State University. State College, PA, USA, 19 November 2010.

"Precise Near-Infrared Radial Velocities with the TripleSpec Exoplanet Discovery Instrument (TEDI)." Lunch Talk, Carnegie Observatories. Pasadena, CA, USA, 22 November 2010.

"Precise Near-Infrared Radial Velocities with the TripleSpec Exoplanet Discovery Instrument (TEDI)." Tea Talk, Astronomy Department, California Institute of Technology. Pasadena, CA, USA, 6 December 2010.

"Precise Near-Infrared Radial Velocities with the TripleSpec Exoplanet Discovery Instrument (TEDI)." Dissertation Talk. *217th Meeting of the American Astronomical Society.* Seattle, WA, USA, 9-13 January 2011.

"Externally Dispersed Interferometry for Terrestrial Exoplanet Detection." Thesis Defense Seminar, Cornell University. Ithaca, NY, USA, 12 May 2011.

TABLE OF CONTENTS

LIST OF TABLES

CHAPTER 1

INTRODUCTION

The last decade of extrasolar planet research has witnessed many major scientific achievements. Efficient Doppler velocity surveys provided the statistics of gas-giant exoplanets in short-period orbits around Sun-like stars (e.g. Udry et al., 2003; Cumming et al., 2003; Marcy et al., 2005; Johnson et al., 2010; Howard et al., 2010), which have strongly influenced planet formation and evolution theories. In particular, the occurrence of close-in gas-giant planets around Sun-like stars brought newfound attention to the role of migration in gas-giant evolution (Goldreich & Tremaine, 1980; Lin & Papaloizou, 1986; Ward, 1997; Masset & Papaloizou, 2003). The discovery of the planet-metallicity correlation, which shows that Sun-like stars with higher heavy-element abundances are correspondingly more likely to host gas giant exoplanets (Santos et al., 2001; Fischer & Valenti, 2005), provided strong evidence for the core-accretion scenario of planet formation, wherein dust in a primarily gaseous protoplanetary disk settles to the mid-plane and forms rocky planetesimals, which eventually grow massive enough to rapidly accrete gas (Pollack et al., 1996).

In addition to statistics, the last decade has seen enormous strides in gas-giant characterization. Those gas giants which transit their host stars provide opportunities to broadly characterize individual exoplanets (e.g. Charbonneau et al., 2000; Henry et al., 2000; Brown et al., 2001). Combining transit photometry with radial velocity measurements accurately measures the exoplanet mass and radius, and therefor also the average density and surface gravity, which constrains the interior structure (e.g. Zapolsky & Salpeter, 1969; Burrows et al., 2000, 2007) and atmospheric scale height (e.g. Miller-Ricci & Fortney, 2010; Rogers &

Seager, 2010) . High precision infrared photometry during the entire exoplanet orbit, including secondary eclipse when the planet passes behind its host star, provides a measurement of the day-night temperature contrasts (Knutson et al., 2007; Agol et al., 2010), which constrains the winds and climate in the upper atmosphere of gas-giant exoplanets. Transit transmission spectroscopy of gas giants planets has identified molecular constituents in their atmospheres (e.g. Seager & Sasselov, 2000; Charbonneau et al., 2002; Swain et al., 2008), and even measured the speed of winds in a planet's upper atmosphere (Snellen et al., 2010).

The challenge to astronomers, astrophysicists and geoscientists over the *next* decade is to understand the statistics of *terrestrial* exoplanets, to probe their diversity and characteristics, and to understand how unique or ubiquitous Earth-like and potentially life-harboring planets are in the galaxy and the Universe. My dissertation involves using novel astronomical techniques and instrumentation to address this ambitious scientific charge, by focusing on the smallest, lightest, yet most numerous stars in the Universe: M Dwarfs.

1.1 Terrestrial Planets and M Dwarfs

M-dwarf stars are highly compelling targets for extrasolar planet surveys (Gaidos et al., 2007; Lunine et al., 2009; Charbonneau, 2009). Consider the following equations for the radial velocity semiamplitude introduced on a star by an orbiting exoplanet, K:

$$K = \sqrt{\frac{G\,(1 - e^2)}{(M_* + M_P)\,a}}\; M_P \sin i \qquad (1.1)$$

where G is Newton's gravitational constant, e is the eccentricity of the orbit, M_P is the mass of the exoplanet, i is the inclination, M_* is the mass of the host star and a is the semi-major axis of the orbit. Inputing the values for the Earth orbiting the Sun, and assuming circular orbits, the equation reduces to:

$$K \text{ [m s}^{-1}] = 0.09 \sqrt{\frac{1}{M_* [M_\odot] \, a \, [AU]}} \, M_P \sin i \, [M_E] \qquad (1.2)$$

The Earth introduces a 9 cm s^{-1} semiamplitude radial velocity variation on the Sun. Measuring 9 cm s^{-1} of radial velocity variation is extremely challenging. To date, the smallest K detected with 3σ confidence on a star–excluding pulsars–is 1.59 m s^{-1}, introduced by a 19 Earth-mass planet with a 1.42 AU semi-major axis on HD 10180 (Lovis et al., 2011). However, consider an M5 dwarf star, with a mass of 0.21 $M_\odot$ and a luminosity of 0.007 $L_\odot$. A planet receiving the same incident stellar flux as the Earth would orbit 0.08 AU from an M5V star. Plugging this reduced semi-major axis and the smaller host star mass into Equation 1.2, the radial velocity semiamplitude of an "Earth-like" exoplanet orbiting an M5 dwarf is 0.69 m s^{-1}. This is still a challenging signal to detect, but nearly an order of magnitude larger than the Earth-Sun signal, and nearly within reach of current radial velocity instrumentation.

As host stars for transiting exoplanets, M dwarfs provide opportunities to broadly characterize terrestrial exoplanets. The fractional decrease in stellar flux due to a transiting planet, D_T, is given by the ratio of the projected areas of the planet and star on the sky. Inputing values for the Earth and the Sun:

$$D_T = 8 \times 10^{-5} \left(\frac{R_P \, [R_E]}{R_* \, [R_\odot]} \right)^2 \qquad (1.3)$$

where R_P is the radius of the planet in Earth radii, and R_* is the radius of the host star in Solar radii. In the case of the Earth transiting the Sun, a 0.008 % depth is extremely difficult to measure, requiring space-based photometry with a long lifespan to measure multiple transits which occur only once per year. The Kepler Spacecraft is designed for this purpose (e.g. Koch et al., 2010). In the case of an Earth-like planet transiting an M5 dwarf star, with a radius of 0.27 $R_\odot$, the signal would be 0.1 %, and would occur once every 18 days. This is almost achievable with ground-based photometry which has measured 0.3 % transit depths (HD 149026 b; Sato et al., 2005). With a larger and more frequent signal, the radii of Earth-like exoplanets orbiting M dwarfs are easier to measure than for those orbiting Sun-like stars. More frequent transits enable repeated spectroscopic measurements during transit. Performing transit transmission spectroscopy on terrestrial planets will require spaced-based observations, and JWST is expected to have enough sensitivity to detect mid-infrared biosignatures in an Earth-like planet transiting an M dwarf, with hundreds of hours of transit observations (Charbonneau & Deming, 2007). An equivalent measurement for an Earth-Sun system is unreasonable given the lifetime of JWST.

The lower temperatures and radii of M dwarfs also increase the secondary eclipse signals from transiting Earth-like planets. At mid-infrared wavelengths, where both the planet and stellar emission is from the Rayleigh-Jeans tail of the blackbody distribution, the fractional decrease in flux due to the planet passing behind the host star, D_S, is given by:

$$D_S = 8 \times 10^{-5} \frac{(R_P \ [R_E])^2 \ T_P \ [K]}{(R_* \ [R_\odot])^2 \ T_* \ [K]} \tag{1.4}$$

where T_P and T_* are the surface temperatures of the exoplanet and host star,

respectively. For the Earth, with T_P = 300 K, orbiting the Sun, with T_* = 5770 K, D_S = 0.0004%, which requires a mid-infrared photometric precision which has yet to be demonstrated on stars. For an Earth-like planet orbiting an M dwarf, D_S = 0.01%, a precision which has been achieved with the Spitzer Space Telescope (Knutson et al., 2007). Secondary eclipse photometry at several infrared bands measures the *surface temperature* of a terrestrial exoplanet, which dramatically affects what types of surface features are possible, including liquid water, presumed to be a requirement for life.

Simply stated, terrestrial exoplanets orbiting M dwarfs will be much easier to characterize than terrestrial exoplanets orbiting Sun-like stars. However, it should not be assumed that M dwarfs are exotic or peculiar hosts for terrestrial, or Earth-like, exoplanets. M dwarfs dominate stellar populations by number, making up 70% of all main-sequence stars (Chabrier, 2003). If terrestrial exoplanets are common around M dwarfs, they will constitute the majority of terrestrial planets in the Universe. In this case, the statistical properties of terrestrial exoplanets orbiting M dwarfs would dominate the statistical properties of all terrestrial planets, including the propensity for harboring life. In order to understand the statistical properties of terrestrial planets in the Universe, we must understand the statistical properties of terrestrial planets orbiting M dwarfs.

It should be noted that terrestrial exoplanets orbiting M dwarfs with Earth-like or warmer equilibrium temperatures are expected to become tidally locked to their host stars after a few billion years (Peale, 1977; Burns, 1986; Kasting et al., 1993). However, this does not detract from the importance of understanding the prevalence of terrestrial planets orbiting M dwarfs.

1.2 The Challenges of Detection

Unfortunately, the advantages M dwarf hosts provide for characterizing low-mass exoplanets come with the challenges of initial detection. M dwarfs are upwards of 5 magnitudes fainter in M_V than Sun-like stars, significantly reducing the efficiency of visible-wavelength radial velocity planet surveys. Being intrinsically fainter, fewer bright M dwarfs occupy a single field on the sky, which reduces the efficiency of single-field transit surveys. This is true despite the fact that M dwarfs dominate stellar populations (Chabrier, 2003). Combining the M_V luminosity function for single main-sequence field stars (Wielen et al., 1983) with the distance modulus, one can calculate the relative number of single main-sequence stars in a magnitude-limited wide-field transit survey. Comparing the number of single, main sequence stars with M_V from 2.5 to 8.5, corresponding to F, G and K dwarfs, to the number with M_V from 8.5 to 18.5, corresponding to M-type dwarfs, one finds that F, G and K dwarfs outnumber M dwarfs in magnitude-limited wide-field survey by more than 1000 to 1. To overcome this limitation, the MEarth transit survey is individually targeting bright M dwarfs, rather than staring at a single field (Nutzman & Charbonneau, 2008) at the expense of continuous coverage.

Despite the challenges, both visible-wavelength radial velocity surveys and transit surveys have had success with M dwarfs. As of now, 27 planets have been detected around 21 M dwarfs, and two are known to transit their host stars: GJ 1214 b and GJ 436 b. All hosts have a spectral type earlier than M5. Statistical analysis of radial velocity surveys indicate that gas giant exoplanets are rare around M dwarfs (Endl et al., 2003; Johnson et al., 2007). Of the transiting exoplanets, GJ 1214 b was initially detected by the MEarth transit survey,

then confirmed by radial velocity measurements (Charbonneau et al., 2009), and GJ 436 b was initially discovered by a radial velocity survey (Butler et al., 2004) with the transit detection occurring later (Gillon et al., 2007). At this stage it is unclear whether the majority of future M dwarf transiting planets will be detected first by transit surveys then followed up with radial velocity measurements, or vice-versa, given that both individually target M dwarfs. However, the Kepler Mission is a sensitive wide-field transit survey observing approximately 2500 M dwarfs brighter than V = 14. If low-mass planets are common around M dwarfs, Kepler will potentially detect dozens of transiting candidates around M dwarfs which are bright enough for follow up radial velocity measurements. Recent statistical analysis of Kepler planet candidates indicates that short period planets are, in fact, more common around low-mass dwarfs than high mass dwarfs (Howard et al., 2011), although this analysis did not include stars later than M0. Measuring precise radial velocities of dozens of faint M dwarf hosts will prove a difficult challenge. The effort to detect and confirm more transiting terrestrial exoplanets can be accelerated by improving radial velocity precision at near-infrared wavelengths. M dwarf spectral energy distributions peak in the near infrared, and the many absorption lines from molecular transitions in near-infrared M dwarf spectra provide rich structure for measuring radial velocity signals (Jones et al., 2009). Precise near-infrared radial velocities will increase the efficiency of exoplanet detection and transit verification around early M dwarfs, and will enable the detection and transit verification of exoplanets orbiting M dwarfs later than M5, which have yet to be discovered.

1.3 Activity and M Dwarfs

Precise radial velocity measurements of M dwarfs must contend with activity-related radial velocity "jitter," introduced by temperature inhomogeneities such as spots or flares on the rotating photosphere (Saar & Donahue, 1997). G- and K-type stars show a correlation between radial velocity jitter and Ca II emission, an indicator of surface activity (Wright, 2005). The "jitter metric" is as an additional white noise term, which when added to that which is expected from photon noise for each radial velocity measurement, replicates the measured RMS of the radial velocity residuals on a given star (Saar et al., 1998) . Typically, the radial velocity jitter component is between 5 and 100 m s^{-1} per measurement. For M dwarfs Hα emission is a typical indicator of surface activity, and has been shown to correlate with Ca II emission (Walkowicz & Hawley, 2009). Using spectra of M dwarfs in the Sloan Digital Sky Survey, West et al. (2004) found the fraction of M dwarfs with Hα emission rises steeply with later spectral type, from less than 5% for M0 dwarfs, to over 70% for M8 dwarfs (West et al., 2004). This could present a challenge for precise radial velocimetry of mid-to-late M dwarfs.

However, less than 10 m s^{-1} of long-term, root-mean-square (RMS) visible-wavelength radial velocity performance has been achieved on early M dwarfs which show Hα emission (Endl et al., 2003; Reiners, 2009). Also, radial velocity jitter is expected to be significantly reduced at near-infrared wavelengths because temperature inhomogenieties on the stellar surface have lower flux contrast (Barnes et al., 2010). For this reason precise near-infrared radial velocities provide an important tool for verifying planetary candidates identified around active stars (Prato et al., 2008). For example, visible-wavelength radial velocity measurements of the young, active star TW Hydra indicated the presence of

a planet (Setiawan et al., 2008), but infrared radial velocity measurements did not (Huélamo et al., 2008), leading to the conclusion that the visible-wavelength Doppler signal was likely due to rotating spots.

1.4 Near-Infrared Radial Velocimetry

Measuring precise near-infrared radial velocities is challenging because of the lack of available high resolution spectrographs, the difficulty of calibration, and interference from absorption lines introduced by the Earth's atmosphere, called telluric lines. Several groups have had success using the telluric lines to calibrate high resolution spectrographs, similar to the iodine cell technique (Butler et al., 1996): Blake et al. (2010) achieved $50 \, \mathrm{m \, s^{-1}}$ of precision on an M dwarf over several years with the NIRSPEC spectrograph (R=25000) on the Keck II telescope, Figueira et al. (2010) achieved $6 \, \mathrm{m \, s^{-1}}$ on an Sun-like star over one week with the CRIRES spectrograph (R=100000) on the European Southern Observatory's Very Large Telescope, and Crockett et al. (2011) achieved $58 \, \mathrm{m \, s^{-1}}$ with CSHELL on the NASA IRTF Telescope. So far, the best precision has been achieved by calibrating CRIRES with an ammonia gas cell, where Bean et al. (2010) achieved $5 \, \mathrm{m \, s^{-1}}$ of long term precision on an M dwarf. Blake et al. (2010), Crockett et al. (2011) and Bean et al. (2010) focus on the CO band head in M dwarfs, a dense forest of stellar absorption lines near 2.3 μm.

High resolution near-infrared spectroscopy is becoming an important technique for M dwarf exoplanet science, but in order to significantly impact the field it must be competitive with visible-wavelength spectroscopy on M dwarfs. Consider GJ 1214, a V=15.1, M4.5 dwarf on which HARPS achieved $5 \, \mathrm{m \, s^{-1}}$ of

1σ radial velocity uncertainty with a 40 minute integration time (Charbonneau et al., 2009). Scaling the CRIRES result to GJ 1214, the ammonia-cell technique would achieve 15 m/s of 1σ radial velocity uncertainty with the same exposure time as HARPS. This is because current high-resolution near-infrared spectrographs suffer from limited simultaneous bandwidth, with NIRSPEC covering 400 nm at one time and CRIRES covering 80 nm. To overcome this, several groups have proposed or are developing high-resolution near-infrared echelle spectrographs with large simultaneous bandwidth, such as the Precision Radial Velocity Spectrograph (Jones et al., 2008), the Habitable-Zone Planet Finder (Mahadevan et al., 2010; Ramsey et al., 2008), and CARMENES (Quirrenbach et al., 2010).

High precision velocimetry and large simultaneous bandwidth can also be obtained by introducing a Michelson interferometer into the optical path between a telescope and an existing *medium*-resolution spectrograph, a method known as externally dispersed interferometry (Erskine, 2003), dispersed fixed delay interferometry (Ge et al., 2006; van Eyken et al., 2010) and also dispersed Fourier transform spectroscopy (Hajian et al., 2007; Behr et al., 2009). The interferometer multiplies the stellar spectrum by a sinusoidal transmission comb before being dispersed by the spectrograph, which creates a moiré fringe pattern highly sensitive to Doppler shifts. Medium-resolution near-infrared spectrographs are becoming widely available on 4-to-6 meter-class telescopes (e.g. Wilson et al., 2004; Simcoe et al., 2010) because of their smaller size and complexity compared to high-resolution spectrographs. The availability of medium-resolution near-infrared spectrographs makes externally dispersed interferometry a promising technique for broad implementation to search for these most interesting low-mass exoplanets.

In this dissertation I present results from the TripleSpec Exoplanet Discovery Instrument, or TEDI, designed to measure precise near-infrared radial velocities of nearby M dwarfs. TEDI is the combination of a Michelson interferometer and TripleSpec, a facility near-infrared spectrograph on the Palomar 200 inch Hale Telescope that simultaneously covers 1.00 to 2.46 μm at a resolution of 2700. The results of this exoplanet program have informed the direction of future exoplanet instrumentation, and highlight the importance of adequate telluric calibration and high throughput in infrared radial velocimetry.

CHAPTER 2

EXTERNALLY DISPERSED INTERFEROMETRY

The theory behind externally dispersed interferometry is described in several previous papers (e.g. Erskine, 2003; Hajian et al., 2007; van Eyken et al., 2010). These treatments are often specific to the instruments involved, and do not account for some of the effects that we encounter with TEDI. Here I provide a theoretical accounting of the TEDI data product and an explanation of how that product is converted into a measured change in radial velocity.

2.1 The Data Product

Given wavenumber $v = 1/\lambda$, an intrinsic stellar spectrum S_v, spectrograph line-spread function R_v (defined below), and an interferometer optical path difference of τ, an individual EDI spectrum, $I_{v,\tau}$, can be described as (Erskine, 2003):

$$I_{v,\tau} = [S_v(1 + \cos(2\pi\tau v))] * R_v \tag{2.1}$$

where $*$ indicates a convolution and $(1 + \cos(2\pi\tau v))$ represents the effect of the sinusoidal transmission comb introduced by the interferometer *before* convolution with the spectrograph line-spread function. The spectrograph line-spread function is a kernel specific to the spectrograph, not the interferometer, and has a width corresponding to the resolution of the spectrograph. It mathematically represents the broadening of spectral lines by the spectrograph. The shape of the line-spread function depends on many factors including the seeing, telescope focus, slit size, spectrograph dispersive properties, and also the data analysis

technique, all of which can effect the final 1-dimensional spectra. It is assumed to vary slowly with wavelength.

In order to get moiré fringes, the delay τ must be slightly varied by $\Delta\tau$ to modulate the resultant spectra. This can be done by either positioning one of the interferometer mirrors such that different delays appear perpendicular to the dispersion direction of the spectrograph (e.g. Erskine, 2003; Zhao et al., 2009), or by actively moving one of the interferometer mirrors with a piezo actuator and taking an individual spectrum at each position. With TEDI, we use the latter approach, moving the mirror to keep the interferometer modulation within a pixel rather than across several pixels. This dramatically reduces the effects of pixel-to-pixel calibration errors, such as effects from poor flat-fielding and/or background subtraction.

If I rewrite τ as a *bulk delay* plus a small *phase shift* ($\tau_0 + \Delta\tau$) and assume that $1/\Delta\tau$ is large compared to a resolution element of the spectrograph, then I can remove $\Delta\tau$ from the convolution integral. In TEDI, $1/\Delta\tau$ is 3 orders of magnitude larger than a resolution element. Applying this and rearranging Equation 1 using trigonometric identities, I can express an individual TEDI spectrum as a function of the bulk delay and phase shift:

$$I_{\nu,\tau_0,\Delta\tau} = A_\nu + B_\nu \cos(2\pi\Delta\tau\nu) - C_\nu \sin(2\pi\Delta\tau\nu) \tag{2.2}$$

where:

$$A_\nu = S_\nu * R_\nu \tag{2.3}$$

$$B_\nu = [S_\nu \cos(2\pi\tau_0\nu)] * R_\nu \tag{2.4}$$

$$C_\nu = [S_\nu \sin(2\pi\tau_0\nu)] * R_\nu \qquad (2.5)$$

A_ν is the spectrum of the star at the native-resolution of the spectrograph, referred to as the "conventional" spectrum. B_ν and C_ν describe the moiré fringes that contain the signal from the high-resolution stellar features. By slightly changing the delay of the interferometer by steps of $\Delta\tau$, and taking spectra at each step, I can fit A_ν, B_ν and C_ν to the modulation at each pixel according to Equation 2. I can then construct the *complex visibility*:

$$B_\nu - iC_\nu = [S_\nu e^{-i2\pi\tau_0\nu}] * R_\nu \qquad (2.6)$$

The complex visibility contains a real and imaginary component which can also be described by a phase, $\phi_\nu = \arctan(B_\nu/C_\nu)$, and a visibility, $V_\nu = \sqrt{B_\nu^2 + C_\nu^2}$. Under a small Doppler shift of the stellar spectrum $S_\nu \rightarrow S_{\nu+\Delta\nu}$, where $\Delta\nu = (\Delta RV\nu)/c$, and assuming that $\Delta\nu$ and $1/\tau_0$ are small compared to a resolution element of the spectrograph, $\Delta\nu$ can be transferred to the exponent by treating the convolution as a Fourier transform integration and applying the Fourier shift theorem. In this case, the Doppler-shifted complex visibility, $B_\nu^1 - iC_\nu^1$, at a given *epoch* is related to an unshifted *template* complex visibility, $B_\nu^0 - iC_\nu^0$, by:

$$B_\nu^1 - iC_\nu^1 = [B_\nu^0 - iC_\nu^0]e^{-i2\pi\tau_0\Delta\nu} \qquad (2.7)$$

Thus, a small Doppler shift causes a change of the phase of the complex visibility. Since all wavelengths receive the same radial velocity shift, the change in phase versus wavelength is expected to follow a simple curve:

$$\Delta\phi = 2\pi\tau_0\Delta\nu = 2\pi\tau_0(\Delta\mathrm{RV})\nu/c \tag{2.8}$$

where $\Delta\mathrm{RV}$ is the change in the radial velocity of the star. However, the motion of the telescope relative to the barycenter of the Solar System introduces large Doppler shifts on the order of 10 km s^{-1} on most stars, which is a significant fraction of a TripleSpec pixel. In this case, the convolution cannot be treated as a Fourier transform and the Fourier shift theorem is not applicable. To accurately account for a large change in the radial velocity of a star, I define a complex line-spread function as $\tilde{R}_\nu = e^{-i2\pi\tau_0(\nu)}R_\nu$. I can now rewrite Equation 2.6 as:

$$B_\nu - iC_\nu = e^{i2\pi\tau_0\nu}[S_\nu * \tilde{R}_\nu] \tag{2.9}$$

Shifting a function before a convolution is equivalent to shifting after a convolution; therefore, a Doppler shift in S_ν will cause the quantity $[S_\nu * \tilde{R}_\nu]$ to shift by the same amount. The Doppler shifted epoch complex visibility, $B_\nu^1 + iC_\nu^1$ relates to an unshifted template complex visibility, $B_\nu^0 + iC_\nu^0$, by:

$$B_\nu^1 - iC_\nu^1 = e^{i2\pi\tau_0\nu}[(B_\nu^0 - iC_\nu^0)e^{-i2\pi\tau_0\nu}]_{\nu\to\nu+\Delta\nu} \tag{2.10}$$

The change in radial velocity, $\Delta\mathrm{RV}$, between the template and epoch can be measured by multiplying the template $B_\nu^0 - iC_\nu^0$ by $e^{-i2\pi\tau_0\nu}$, interpolating the product onto a Doppler-shifted $\nu + \Delta\nu$ grid, multiplying that by $e^{i2\pi\tau_0\nu}$, and then comparing the resulting complex visibility to an epoch complex visibility ($B_\nu^1 - iC_\nu^1$). The visibilities, V_ν, of the template and epoch measurements depend on the quality of interference or contrast in the interferometer in addition to the radial

15

velocity shift, but the phases ϕ_v only depend on the radial velocity shift. For this reason, I fit a shifted template to an epoch measurement with ΔRV as a free parameter, using the error-weighted difference in *phases* as the goodness-of-fit statistic.

In configuring TEDI for a particular target, the value of the bulk delay τ_0 is chosen to produce the largest radial velocity signal in B_v and C_v. This depends on several factors with the rotational broadening of the target's absorption lines playing the largest role. The rotational broadening relates to the rotation of the star, V_{rot}, projected along the angle of the rotation axis with respect to the line of sight, i, such that $\Delta v_{rot} = V_{rot} \sin i v / c$. The radial velocity signal is maximized when the periodicity of the interferometer comb, $1/\tau_0$, matches the width of the stellar lines, Δv_{rot}, causing the largest modulation of spectra, $I_{v,\tau_0,\Delta\tau}$, with $\Delta\tau$. Rotational broadening increases linearly with wavenumber, but the period of the comb does not. This means that each wavelength has a different optimal bulk delay; optimizing the bulk delay across an entire spectrum is typically done by choosing the bulk delay corresponding to the spectral region with the highest line density and highest flux, both of which depend on the spectral type. For these reasons, the bulk delays available in TEDI were chosen based on performance simulations using rotationally broadened high-resolution model spectra of late-type stars calculated using the PHOENIX model (e.g. Fuhrmeister et al., 2005). We used a bulk delay of 4.6 cm for the results in this paper, corresponding to a projected rotational velocity of 1 to 5 km s^{-1} for a mid-M star.

Figure 2.1 simulates the effect of the interferometer and spectrograph on a model stellar spectrum, showing the resultant moiré fringes.

A: Model Stellar Spectrum

B: Model Stellar Spectrum, as an Image

C: Interferometer Transmission Comb

D: Stellar Spectrum times Interferometer Transmission Comb

E: Broadened by Spectrograph Line-Spread Function
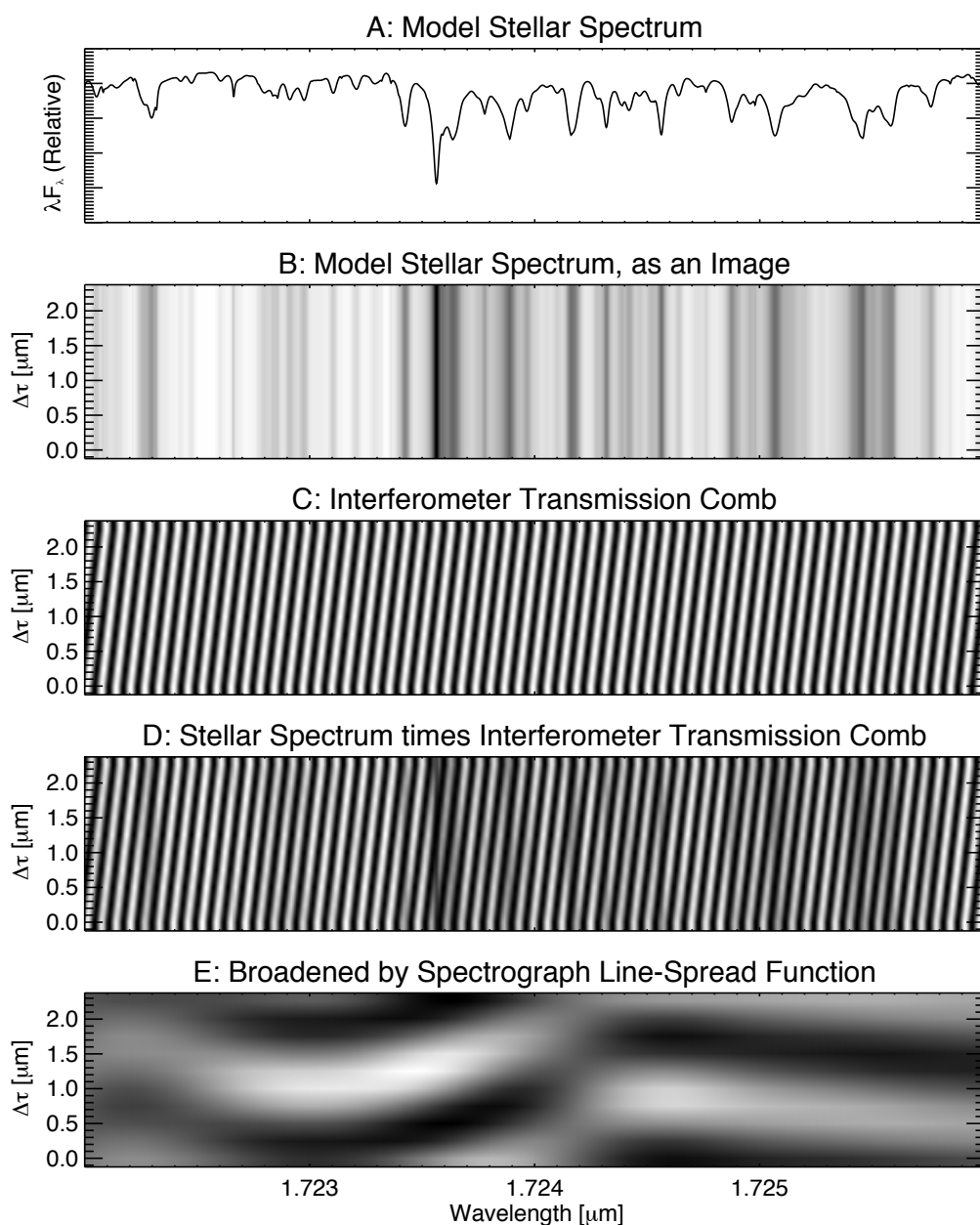
Figure 2.1 – Simulated data showing the effect of the interferometer and spectrograph on a model stellar spectrum. *A*: High-resolution late-type stellar model calculated using PHOENIX model atmosphere code versus wavelength (e.g. Fuhrmeister et al., 2005), for a small region of H band. *B*: Same, but plotted as an image. *C*: Image of the interferometer transmission comb, versus wavelength and phase step $\Delta\tau$. *D*: Product of the stellar spectrum and the interferometer transmission comb. *E*: Same as *D*, but after the spectra are broadened by the spectrograph line-spread function, and each wavelength channel has been renormalized to enhance the fringe features. The phases of the resultant moiré fringes versus phase step are highly sensitive to a Doppler shift of the original spectrum.

17

2.2 Description in Fourier Space

The effect of the interferometer on radial velocity performance can also be described in Fourier space. Figure 2.2 plots the Fourier transform of a high-resolution model spectrum used in the performance calculations. Included in the plot is the expected Doppler content for each Fourier frequency, and the response functions of TEDI and a theoretical R=100,000 spectrograph. By multiplying the stellar spectrum by the sinusoidal interferometer transmission comb before convolution with the spectrograph, the interferometer shifts the response window of TripleSpec alone to those Fourier frequencies with the highest Doppler content. The Doppler content of a particular Fourier component is computed as the average derivative of that component, equal to the Fourier power times the Fourier frequency.

2.3 Determining the Interferometer Delay

In my account of the TEDI data product and ΔRV measurement, I have relied on accurate knowledge of the bulk delay and phase steps, which together make up the interferometer delay. However, errors in these quantities will result in errors in the measured change in radial velocity. An error in the estimation of the bulk delay will appear as a proportional error in ΔRV. For example, a 1% error in τ_0 will correspond to a 1% error in ΔRV. These errors can be calibrated by observing radial velocity standard stars, and changing the bulk delay to minimize the residuals between the ΔRV measurements and those expected from the motion of the telescope relative to the Solar System barycenter.
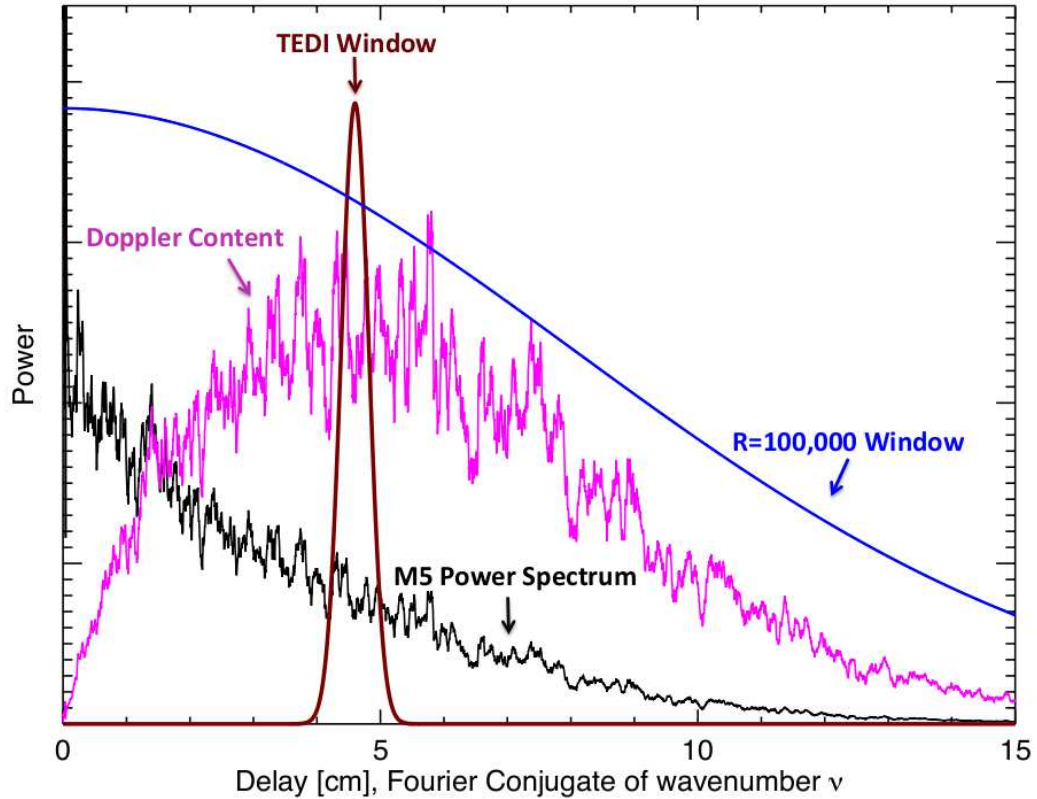
Figure 2.2 – Fourier transform of a high-resolution late-type stellar model calculated using PHOENIX model atmosphere code (e.g. Fuhrmeister et al., 2005). Included is the expected Doppler content for each Fourier frequency, and the response functions of TEDI and a theoretical R=100,000 spectrograph, versus delay in cm (the Fourier conjugate of wavenumber v). By multiplying the stellar spectrum by the sinusoidal interferometer transmission comb before convolution with the spectrograph, the interferometer shifts the response window of TripleSpec alone to those Fourier frequencies with the highest Doppler content. The Doppler content of a particular Fourier component is calculated as the average derivative of that component, equal to the Fourier power times the Fourier frequency, or the delay.

An error in the estimation of the phase steps is much more severe. If all of the phase steps used to construct the complex visibility are incorrectly estimated by an offset, $\delta(\Delta\tau)$, this will correspond to an offset in the radial velocity change, $\delta(\Delta\text{RV})$, of

$$\delta(\Delta\text{RV}) = \frac{\delta(\Delta\tau)}{\tau_0}c \qquad (2.11)$$

With a bulk delay of 4.6 cm, a 1 nm offset in the phase steps corresponds to a 7 m s^{-1} error in the measured change in radial velocity.

Ensuring that the interferometer has a specific delay with 1 nm of accuracy for every epoch observation is extremely challenging. Instead, with TEDI we calibrate the bulk delay and phase steps with emission lines from a ThAr hollow cathode lamp, and use the modulation of the emission lines to correct for delay differences after the data have been collected. Since the delay is not accurately reproduced for each measurement, we cannot use radial velocity standard stars for delay calibration; however, they can be used for roughly measuring the change in delay between observing nights, with ThAr lines used for precise measurements.

2.4 Telluric Calibration

Spectroscopic observations at near-infrared wavelengths must contend with telluric absorption lines introduced by the Earth's atmosphere. Telluric lines are caused by many species of molecules in the Earth's atmosphere, and the largest contributors at near-infrared wavelengths are H_2O, CO_2 and CH_4. Telluric lines

are numerous across near-infrared wavelengths and will contaminate the stellar complex visibility. In conventional spectroscopy the standard method for removing telluric lines is to observe a featureless star with a known spectrum, such as a rapidly rotating B star or an A0, Vega-like star, at a similar airmass, and divide that into the target spectrum (e.g. Vacca et al., 2003). Unfortunately, the complex visibility is not amenable to a simple division, necessitating a more complex and less robust calibration technique. Simulations of telluric contamination and removal indicate the best method to empirically calibrate telluric lines in TEDI observations is to *subtract* the complex visibility of a calibrator from that of the target, normalized to the conventional spectrum A_ν of the target. However, incomplete or inaccurate telluric calibration will introduce an error into the measured radial velocity. Simulations indicate that telluric calibration currently limits TEDI performance, which I address in Section 6.

CHAPTER 3

THE TRIPLESPEC EXOPLANET DISCOVERY INSTRUMENT

The TripleSpec spectrograph was commissioned in October of 2007 (Wilson et al., 2004; Herter et al., 2008). TripleSpec is a cross-dispersed, long-slit near-infrared echelle spectrograph, dispersing a 1 x 30 arcsecond slit from 1.0 to 2.5 μm across 5 orders at resolution 2700 onto 2 quadrants of a Rockwell Scientific[1] Hawaii-2 HgCdTe detector.

In December of 2007, we attached an interferometer to TripleSpec to form TEDI (Edelstein et al., 2010). The original design used a mirror to redirect the telescope beam toward the interferometer, with a pellicle beam splitter used to simultaneously inject ThAr emission light. The design suffered from non-common path errors between the starlight and ThAr light, described in Appendix A and Muirhead et al. (2010). In December of 2009, we removed the interferometer from TripleSpec and upgraded the design to eliminate the non-common path behavior. The overlapping starlight and ThAr light is now focused onto a fiber before the interferometer, which ensures common path and common delay between the two. The new design includes two fibers; nodding the target between the fibers nods the target on the TripleSpec detector, allowing for efficient background subtraction. The upgraded interferometer was attached to TripleSpec in June 2010.

---

[1]Now Teledyne Technologies

3.1 The TEDI Beam Path

Figure 3.1 depicts the beam path through the interferometer before entering TripleSpec. First we describe the injection of starlight and ThAr light into the science fibers: (1) A mirror mounted on a removable swing arm deflects the f/16 telescope beam that would otherwise go to TripleSpec. (2) A mirror mounted on a 3-axis, tip/tilt/piston piezo actuator directs the beam towards the two science fibers. (3) A visible/near-infrared dichroic reflects the visible light to the CCD camera (4) and transmits the near-infrared light to the science fibers. Once a star has been placed on a science fiber, the CCD camera (4) is used to monitor the location of the star's visible image, and tip/tilt commands are sent to the piezo actuator in (2), ensuring that the star does not drift off of the science fiber. To introduce the ThAr calibration light a small telescope (5) images a 1 mm fiber core carrying the ThAr emission light to the science fibers at f/16, matched to the telescope beam. The magnified 4 mm fiber core illuminates both science fibers with ThAr light. (6) A flat window mixes the ThAr light into the science beam by reflection. (7) The science fibers accept the starlight and ThAr light via glued-on microlenses, which convert the f/16 beam to an f/4 beam.

Next we describe the interferometer: (8) Starlight and ThAr light exit the fibers via an identical set of microlenses at f/16, with an additional single-mode fiber carrying He-Ne laser light mounted nearby. (9) An off-axis parabola collimates the beams. (10) The beam splitter directs half of the beam to a fixed mirror, and the other half through one of several etalons (11) to a mirror mounted on a second 3-axis piezo actuator and an adjustable linear stage (12) used in combination with the etalon to introduce the delay. (13) One interferometer output is directed to another visible/near-infrared dichroic (14), which sends the near-

23

infrared light to a chopper/photodiode system to actively monitor throughput (15). The second dichroic sends visible light to a second CCD camera (16). The second CCD camera images the interference pattern produced by the He-Ne laser light. The pattern is altered by adjusting the tip/tilt/piston piezo actuator in (12). When the interference pattern contains no fringes, the interferometer is well aligned and produces the highest stellar moiré visibilities. The other interferometer output is directed back toward the TripleSpec window via a fold mirror (17), with an adjustable mirror located at the pupil (18) for positioning the image of the fiber on the TripleSpec slit. A mirror underneath the removable swing arm (19) redirects the beam down into TripleSpec at f/16. The entire interferometer assembly sits above TripleSpec at the Cassegrain focus and fits inside the 39 inch (1.0 m) diameter hole in the 200 inch primary mirror of the Palomar Hale Telescope.

3.2   TEDI Operations Software

The TEDI operations software was assembled using National Instruments LabVIEW^{TM} software and designed to acquire a target and take a series of spectra. It sends TCP/IP commands to the native TripleSpec software which operates TripleSpec in the conventional mode. In addition to the 2048 x 1024 Hawaii-2 detector for taking spectra, TripleSpec has a 1024 x 1024 detector which images the slit in K band. The imaging detector is used for focusing the telescope, acquiring a target through the slit, and sending telescope pointing corrections using nearby stars for guiding. The native TripleSpec software operates both the spectrograph detector and the imaging detector, and runs on computers in the Palomar computer room linked to TripleSpec via fiber optics.
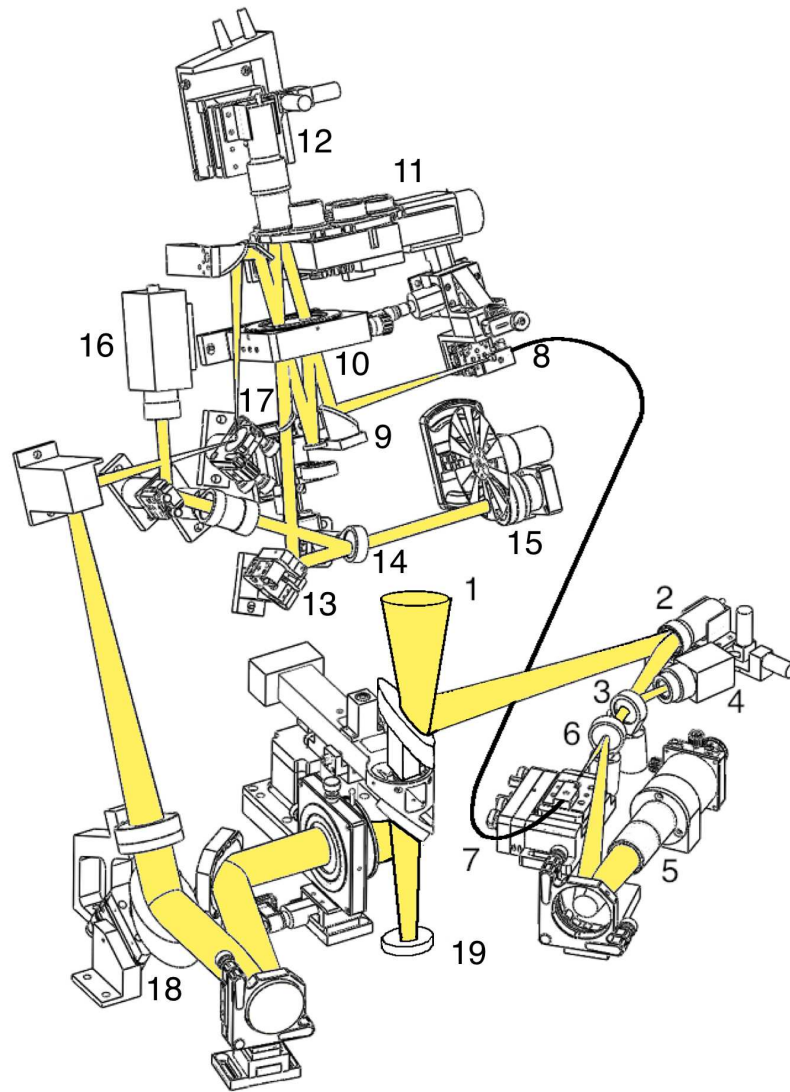
Figure 3.1 – Schematic and beam path of the TEDI Interferometer, described in detail in Section 3.1. The yellow shaded region corresponds to the beam path. The pick-off mirror at (1) directs starlight to a guider system which injects the starlight and ThAr calibration light into fibers at (7). The fibers lead to the interferometer at (8), and eventually to a mirror which redirects the beam down to TripleSpec at (19). This entire assembly sits above TripleSpec at the Cassegrain focus and fits inside the 39 inch diameter hole in the 200 inch primary mirror.

The TEDI software operates the elements in the interferometer depicted in Figure 3.1. The elements require many different connections, requiring the control computer reside near the instrument, mounted in an electronics rack near the Cassegrain focus. The TEDI software acquires a target through the system, and sends commands to the native TripleSpec software via TCP/IP for exposing with the spectrograph detector, and adding and changing the values of the headers.

The original TEDI software (2007-2009) relied on the native TripleSpec software for acquiring a target and guiding the telescope. This proved to be inefficient at acquisition and ineffective at guiding for several reasons. The pick-off mirror in TEDI blocks the slit and roughly half of the native TripleSpec field-of-view, and there was no equivalent of a slit-imager inside TEDI to ensure that the starlight was aligned with the interferometer path. Acquisition involved moving a target into the viewable portion of the TripleSpec slit-imager, then offsetting the telescope by at least 2 arcminutes to move the starlight into position. More often than not, the errors in the offset led to a misalignment, in which case we had to jog the telescope around until starlight was seen spilling over the slit. This procedure introduced 10s of minutes of overhead for target acquisition.

As stated earlier, nearby bright M dwarfs are spread across the entire sky, and not localized to the galactic plane. Many of the TEDI targets are at high galactic latitude and do not have bright guide stars available. We rarely if ever have a guide star bright enough to guide with > 0.1 Hz of corrections. Without the guiding corrections, the target would fall off of alignment within 10s of minutes, requiring re-acquisition and the corresponding overhead.

When the interferometer was removed and redesigned in the first half of

2010, I built an internal guiding system for the TEDI interferometer. As depicted in Figure 3.1, a dichroic splits the near-infrared and visible light of the star, and sends the visible light to a high-speed readout CCD and the near-infrared light to the science fibers. This provides a constant image of the target at visible wavelengths which is used for guiding. Instead of issuing guiding commands to the telescope, we use a 3-axis piezo actuator attached to a fold mirror (Element 2 in Figure 3.1) capable of high-speed tip and tilt corrections to direct the telescope beam into the fibers. This enables guiding corrections of 5 to 10 Hz.

To acquire the star before guiding, we installed a near-infrared photodiode on the backend of the interferometer to measure the infrared flux through the system in real time. By correlating the location of the star on the CCD with the flux monitor, the location of the star with the highest flux can be determined and guided on. Figure 3.2 shows the TEDI guider software for acquiring a target, peaking the flux, and guiding the star to the peak position.

Once a target is acquired and guiding is on, the TEDI fringe tracking software is used. With the fringe tracking software, the user operates a second 3-actuator piezo attached to one of the interferometer cavity mirrors to align the beams and introduce phase steps ($\Delta\tau$). A second CCD camera images fringes created by a HeNe laser injected by a single-mode fiber through the interferometer. The single-mode fiber spatially filters the HeNe light to produce high visibility fringes on the second CCD. Tip and tilt commands are sent to the second 3-actuator piezo until the fringes are removed, at which point the user can initiate a sequence whereby the piezo is stepped 10 times a distance of 0.125 μm, and at each position a TCP-IP signal is sent to the TripleSpec software to take a spectrograph exposure. The TEDI fringe tracking software is also used to acti-
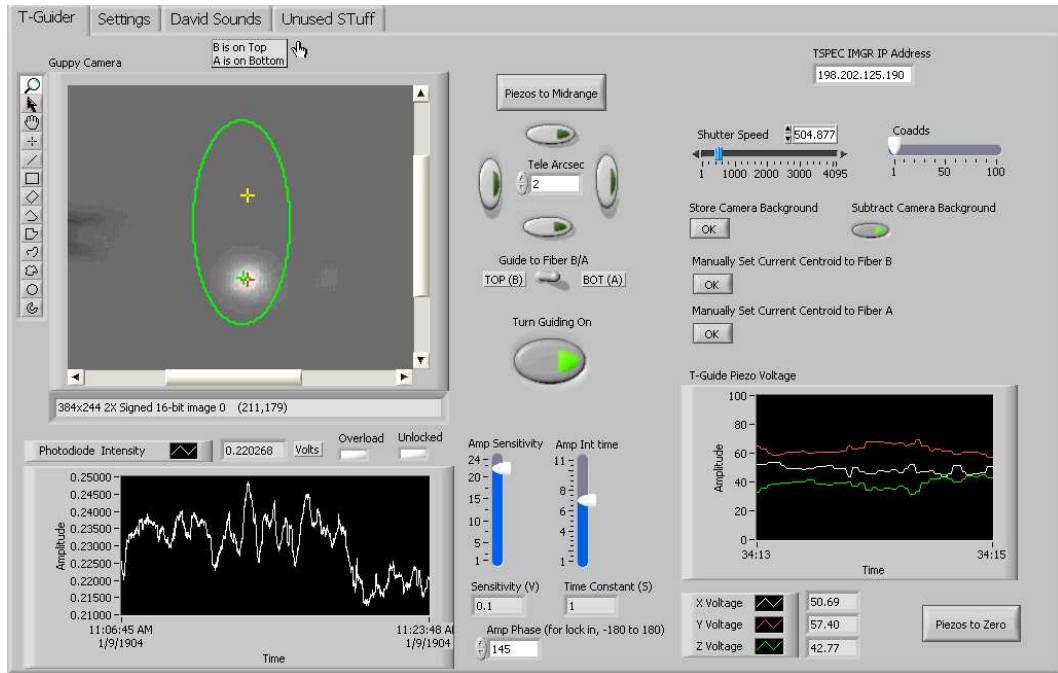
Figure 3.2 – A screen shot of the TEDI guider software, with a target acquired on a fiber and actively guiding with the piezo tip/tilt actuator. *Upper left:* The CCD images the visible light from a target. The yellow and green crosshairs indicate the location of the fibers, as determined by correlating the center-of-light of the target with the peak readout on the infrared flux monitor. The red crosshair is the centroid of the target, and the difference between that and the fiber location is used to send guiding corrections to a tip-tilt piezo actuator using a PID control loop. *Lower left:* The chart displays the real-time infrared flux through TEDI as reported by the infrared photodiode on the back-end of the interferometer. *Lower right:* The chart displays the voltages applied to the 3-axes of the tip/tilt piezo actuation. This is displayed to make sure the piezo voltages are within their limits and that the control loop is performing correctly. *Upper right*: Controls for acquiring and guiding on a target.

vate various pico motors which control steering mirrors to direct the starlight to the spectrograph slit in the case of flexure in the instrument. The mirror at (18) in Figure 3.1 is used to position starlight on the slit, and pico motor commands to this mirror are necessary with each target acquisition.

The fringe tracking software was originally written by Tony Mercer under the supervision of Jerry Edelstein and Matthew Muterspaugh. When the interferometer was removed and redesigned in the first half of 2010, Dr. Edelstein and I supervised students Philip Andelson and David Kimber, who upgraded the software to work with the new design. Figure 3.3 displays an image of the current fringe tracking software.

3.3   Throughput

TEDI adds many optical surfaces into the beam path prior to entering TripleSpec–26 surfaces for one interferometer arm and 30 for the other–and uses 50% of the starlight for monitoring throughput. This is necessitated by the geometry of adding the interferometer to TripleSpec at its existing Cassegrain mount, but results in significant throughput loss. With 1 arcsecond seeing, the total throughput of the system–including the atmosphere, telescope, interferometer and TripleSpec–peaks at 1.5% at 1.68 μm. Without the interferometer, the throughput peaks at 30%. Focal ratio degradation in the optical fibers also contributes to the lower throughput. TripleSpec contains a Lyot stop which, when combined with the slit, matches the seeing-limited etendue of the telescope. Focal ratio degradation in the fibers will effectively increase the etendue of the beam, and introduce irrevocable losses at either the Lyot stop or the slit,

29
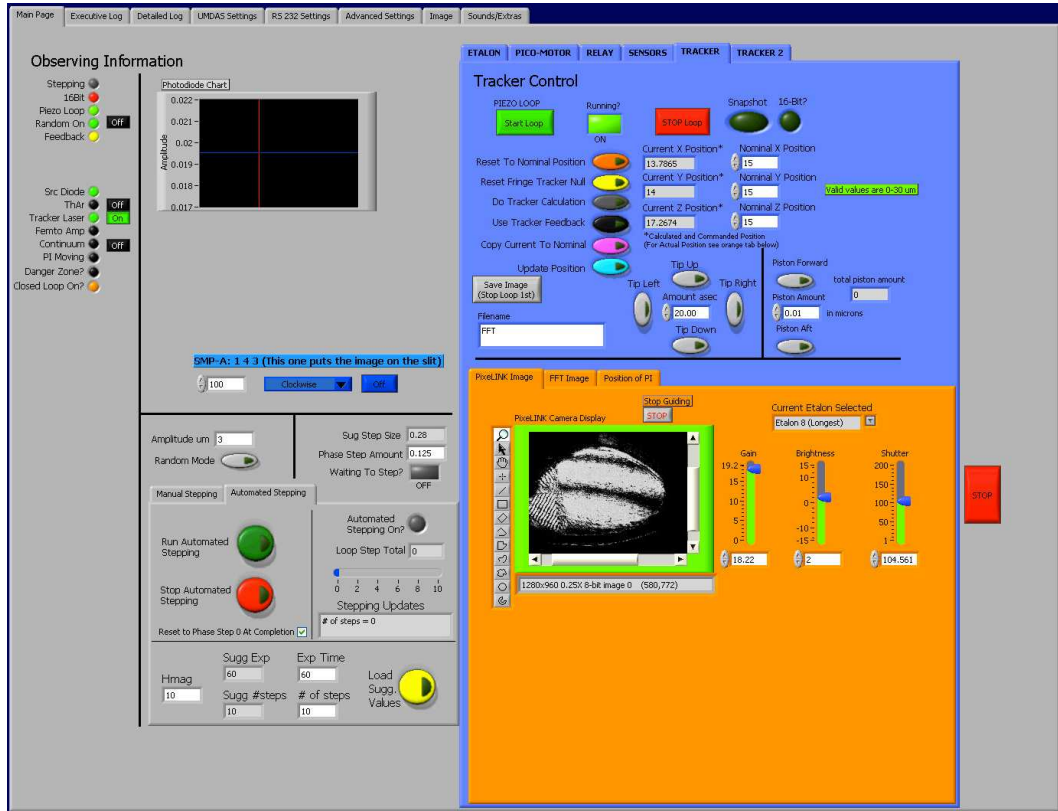
Figure 3.3 – A screen shot of the TEDI fringe tracking software. The image at the center of the screen displays the fringe pattern created by HeNe laser light injected through the interferometer via a single-mode fiber. The controls above are used to tip and tilt the cavity mirror and eliminate the fringes.

depending on the focus.

3.4   Fiber Scrambling

The output illumination of a multimode fiber is dependent on various factors including the input illumination geometry. Methods can be applied to reduce this dependence so that the output fiber illumination is less affected by changes in seeing, telescope pointing or telescope focus, called "fiber scrambling." Methods include an optical double scrambler (Hunter & Ramsey, 1992; Lovis et al., 2006) or a mechanical fiber agitator (Baudrand & Walker, 2001; Ramsey et al., 2008), though the methods are not equivalent and produce different fiber output illumination. TEDI does not use supplemental fiber scrambling methods.

Partial fiber scrambling is achieved by the microlenses attached to the science fibers, which image the telescope pupil onto the fiber core and act as an image pupil exchanger (Figure 3.4), similar to a "double-scrambler" (Hunter & Ramsey, 1992). However, without identical input illumination, the ThAr and stellar cavity illumination will behave slightly differently. The ThAr injection is mechanically fixed while the stellar injection will change depending on seeing, guiding and focus fluctuations. This could introduce errors into the calibration of τ_0 and $\Delta\tau$, if the slightly different illumination through the interferometer results in different optical paths. I measured this effect experimentally by simulating fiber illumination fluctuations and believe it is not a significant source of radial velocity fluctuations. I discuss the experiment and results in Chapter 6.2.
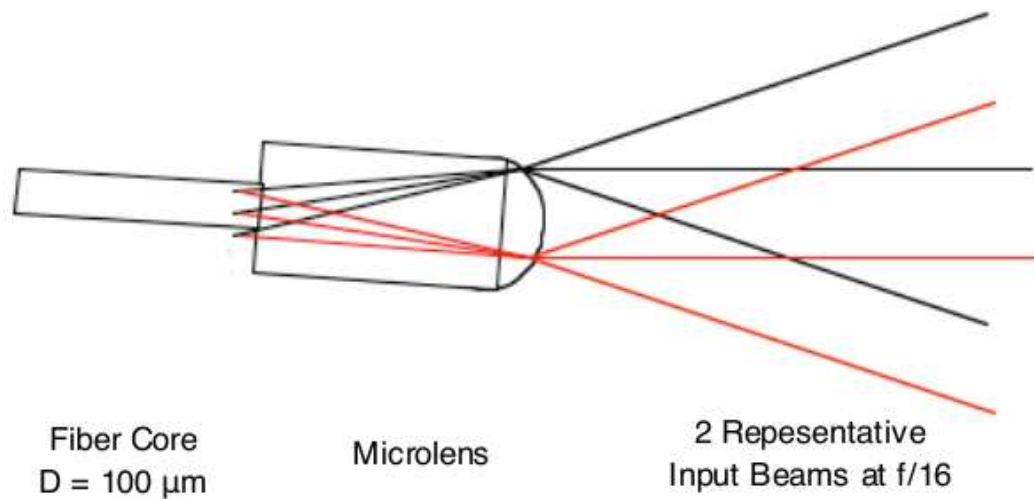
Figure 3.4 – Schematic of the input illumination into the TEDI science fibers. Microlenses glued to the tip of the fibers match the incoming f/16 beam to the 100 μm fiber core. The microlenses image a pupil onto the fiber core, such that changes in the position of the image on the tip of the microlenses do not dramatically change the illumination on the fiber tip. In this way, the microlenses help to scramble the input illumination. Image provided by Jerry Edelstein.

CHAPTER 4

OBSERVATIONAL PROCEDURE AND DATA ANALYSIS

Figure 4.1 shows a sample TEDI exposure with both mixed star-ThAr light and ThAr light alone. A single TEDI measurement of the complex visibility in one fiber consists of 20 nonsimultaneous spectra: 10 of mixed star-ThAr light, and 10 of ThAr alone. After 10 exposures with the star focused on one fiber, the star is nodded to a second fiber. Since both fibers receive constant ThAr light, the nodding procedure efficiently provides 10 mixed star-ThAr and 10 ThAr alone spectra on both fibers. Between each of the 10 exposures we change the delay by 0.25 μm using a closed-loop Piezo actuator (element #12 in Figure 3.1). In order to fit the coefficients A_ν, B_ν, and C_ν in Equation 2, $\Delta\tau$ must Nyquist sample $I_{\nu,\tau_0,\Delta\tau}$ for all ν. Ten spectra with steps of 0.25 μm ensures this condition for the full TEDI bandwidth, and we refer to this set of 10 spectra as a *phase set*.

Converting 20 exposures, and 40 spectra, into complex visibilities for both fibers involves several steps: spectral extraction, deconvolution of the ThAr lines from the mixed star-ThAr spectra, fitting A_ν, B_ν and C_ν to both the ThAr and stellar spectra, accounting for changes in the start delay between template and epoch by referencing A_ν, B_ν and C_ν to the same start delay, and subtracting the complex visibility of a telluric calibration star. With the complex visibilities measured for a template and an epoch, we measure the radial velocity change between the two by fitting a shift as in Equation 9. We treat each fiber independently, with independent template and epoch measurements.
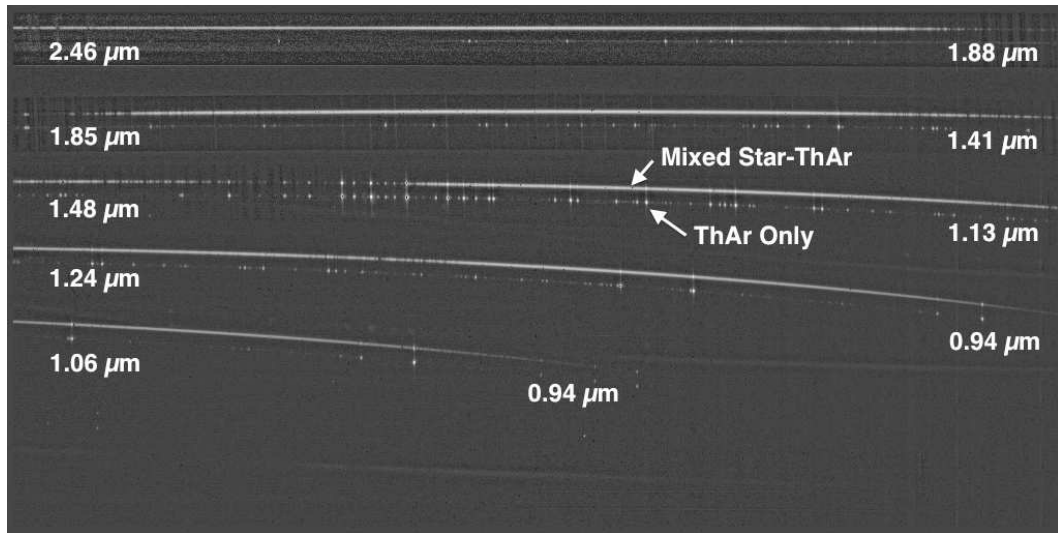
Figure 4.1 – An example TEDI exposure, flat-fielded and dark-subtracted, show-ing mixed starlight-ThAr lines on the upper fiber, and ThAr lines alone on the lower fiber, annotated to show wavelengths. Each fiber receives constant ThAr emission light to measure the changes in delay introduced by stepping one of the cavity mirrors with a piezo actuator, with the starlight nodded between the two fibers. The starlight and ThAr light is cross-dispersed across 5 orders onto 2 quadrants of a Hawaii-2 HgCdTe detector. Background effects such as thermal emission and OH emission lines from the Earth's atmosphere are removed by subtraction after the spectra have been extracted.

4.1 Spectral Extraction

Each TripleSpec exposure contains several electronic anomalies which were removed during data processing by modeling the effects and subtracting them out. An IDL routine for removing the electronic anomalies in TripleSpec exposures is available on the author's website,[1] and this routine has been used in previous TripleSpec results (Miller et al., 2011; Rojas-Ayala et al., 2010; Martinache et al., 2009). The details of the electronic anomalies are beyond the scope of this paper, but they involve crosstalk of signals between the detector quadrants, and capacitive coupling of signals between the channels within each quadrant. For a discussion of crosstalk and capacitive coupling in nondestructive arrays, including Hawaii-2 HgCdTe detectors, we refer the reader to Chapter 6.6.4 of Rieke (2002).

The TripleSpec detector is subject to a variable electronic background, which changes slowly across the detector and slowly with time. The electronic background is mostly removed by subtracting multiple correlated readouts (Garnett & Forrest, 1993). However, correlated sampling does not fully remove the electronic background in the detector, which persists and changes with each exposure. To remove the fluctuating electronic background, we subtract the median of a 20 x 20 pixel box centered around the extraction point. Each exposure was filtered for cosmic rays and hot pixels using the IDL routine `sigma_filter.pro`, available from the IDL Astronomy User's Library (Landsman, 1993), which locates pixels significantly brighter than their neighbors. We flag these pixels as bad, and they are not used in any further analysis.

Individual exposures are flat-fielded and dark subtracted using dome flats

---

[1]`http://astrosun2.astro.cornell.edu/~muirhead/tspec_clean.pro`

and dome darks taken before an observing night. It is difficult to attain a true estimate of the read noise because TripleSpec does not have the capability to take a "cold dark," wherein a cryogenic mask fully occults the detector. Instead, we use the dome darks to construct an image of the read noise of the detector, as well as flag any hot or variable pixels. Dome darks contain significant background emission in K band, and subtracting them from target exposures leaves a negative K band background. We remove the negative background after the spectra are extracted, however the photon noise from the thermal emission in the dome dark inflates the estimate of the read noise.

We extract the spectra by (non-optimally) summing pixels across the slit image on the TripleSpec detector. The TripleSpec slit is tilted on the detector by different amounts at different wavelengths, and summing pixels in this fashion slightly degrades spectral resolution. The tilt is nowhere more than 10 degrees; as such the resolution loss is less than 3%. We chose to sum pixels along the slit to avoid aliasing effects introduced when interpolating the slit onto a rectilinear grid, or interpolating a profile onto the non-rectilinear detector. We replace bad pixels with the value of a profile fit to the slit image, where the profile is constructed from nearby slit images. For slit images where more than 40% of the pixels are flagged, the entire wavelength channel is flagged as bad. For each extracted wavelength channel, we subtract the median of a 20 x 20 box centered on those pixels to eliminate a fluctuating electronic background in the TripleSpec detector.

A two-dimensional polynomial wavelength solution for the TripleSpec detector was determined using gas discharge lamps and a slit mask during commissioning of the spectrograph. TripleSpec has no internal moving parts, which

minimizes flexure and changes in the wavelength solution. However, large changes in the gravity vector of TripleSpec result in illumination shifts of approximately 1 pixel. After extraction, Gaussian profiles are fit to bright, isolated ThAr lines, and the profile centroids are used to offset to the original wavelength solution to account for flexure. Figure 4.2 plots example mixed star-ThAr TEDI spectra, in units of signal-to-noise.

In order to measure radial velocity changes, it is more important that the wavelength solutions of the spectra are the same for every measurement, rather than accurate for every measurement. This is ensured by cross-correlating the A_v's of the ThAr-alone spectra of the epoch measurements onto the A_v of the ThAr-alone spectra of the template measurement. The shift applied to the epoch ThAr spectra is then applied to the corresponding mixed Star-ThAr epoch spectra. For sub-pixel shifts, the spectra are shifted using spline interpolation.

4.2   Star-ThAr Separation

To measure the set of phase steps introduced into a mixed star-ThAr phase set, the ThAr lines must be separated from the mixed star-ThAr spectra. This is done by interpolating the stellar spectrum underneath the ThAr lines and then subtracting that interpolated spectrum. The locations of the ThAr lines are determined using the ThAr-alone phase set taken immediately before or after the mixed spectra on the same pixels using the nodding scheme. From here on, we make the distinction between ThAr-alone and ThAr-separated phase sets, the former being the phase set of ThAr alone immediately preceding or following the mixed star-ThAr phase set, and the latter being separated from the mixed
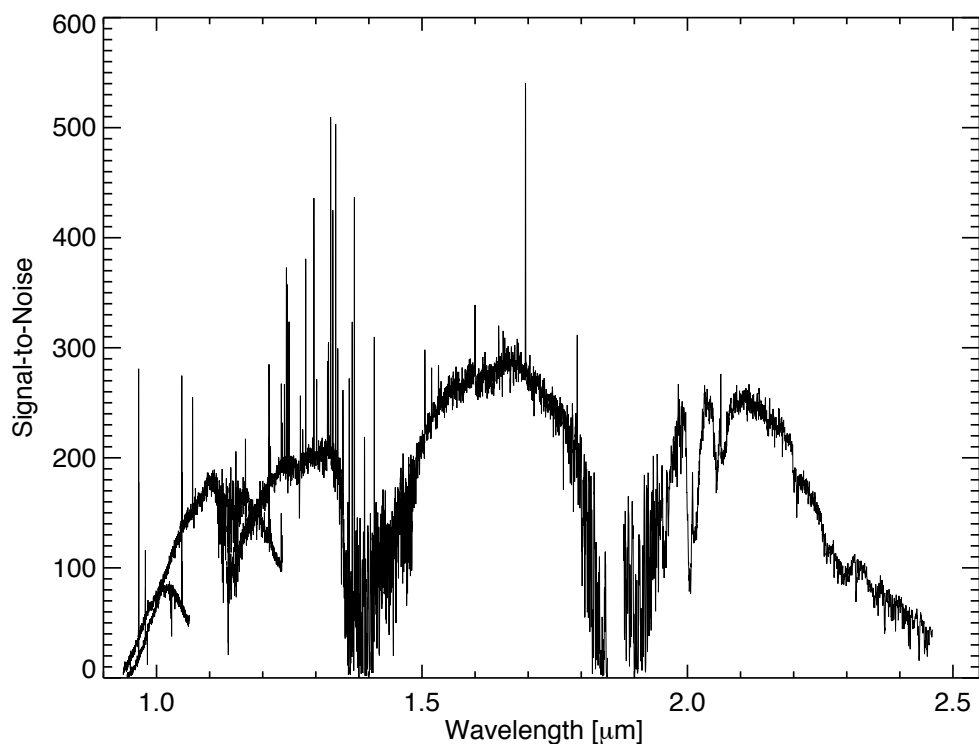
Figure 4.2 – A typical TEDI spectrum of mixed stellar (GJ 699) and ThAr light in units of signal-to-noise. The TripleSpec orders are plotted independently, and they overlap around 1.00 and 1.25 μm. Ten spectra, called a "phase set", are combined to form the complex visibility (see Figure 4.3). The extracted spectra are not corrected for instrument efficiency or telluric transmission, since the radial velocity signal is in the moiré modulation of the spectra, not the overall shape. Telluric effects are calibrated out after modeling the moiré fringes. The steep drop in signal-to-noise at 2.2 μm is due to the combination of higher background and lower transmissivity of the dichroic used for guiding (element 3 in Figure 3.1).

star-ThAr spectra. Figure 4.3 plots images of the 10 mixed and separated stellar and ThAr spectra, and shows the resultant moiré fringes, to which A_ν, B_ν and C_ν are fit.

4.3 Fitting A_ν, B_ν and C_ν

In order to fit the coefficients A_ν, B_ν and C_ν to the stellar spectra, we first fit them to the ThAr-alone and ThAr-separated phase sets, which determines the sizes of the phase steps, $\Delta\tau$. The model for the data is Equation 2, with A_ν, B_ν, C_ν and 9 of the 10 phase steps, $\Delta\tau$, as the free parameters. The first phase step is fixed at 0. The fitting procedure is a joint non-linear Levenberg-Marquardt (LM) fit for the phase steps and a linear fit for A_ν, B_ν and C_ν at each wavelength channel. For each LM iteration of the 9 phase steps, a linear fit of A_ν, B_ν and C_ν is performed for each wavelength channel of the phase set. The best-fit delays, and best fit A_ν, B_ν and C_ν, are found when the error-weighted χ^2 residuals between the model and data are minimized. The fitting procedure adjusts the phase steps to ensure that the ThAr lines fluctuate sinusoidally. This method was chosen over a fully non-linear fit to increase computational efficiency, since there are over 10000 wavelength channels in a given phase set. A general description of the joint LM-linear fitting method is available in Wright & Howard (2009).

When fitting A_ν, B_ν and C_ν to the *stellar* spectra, the phase steps are fixed since they are determined by the separated ThAr lines. Therefore, only the linear portion of the fitting routine is used. Before fitting the stellar coefficients, the ThAr-alone coefficients are used to create a model of the background at the phase steps of the mixed star-ThAr phase set, and that is subtracted from the
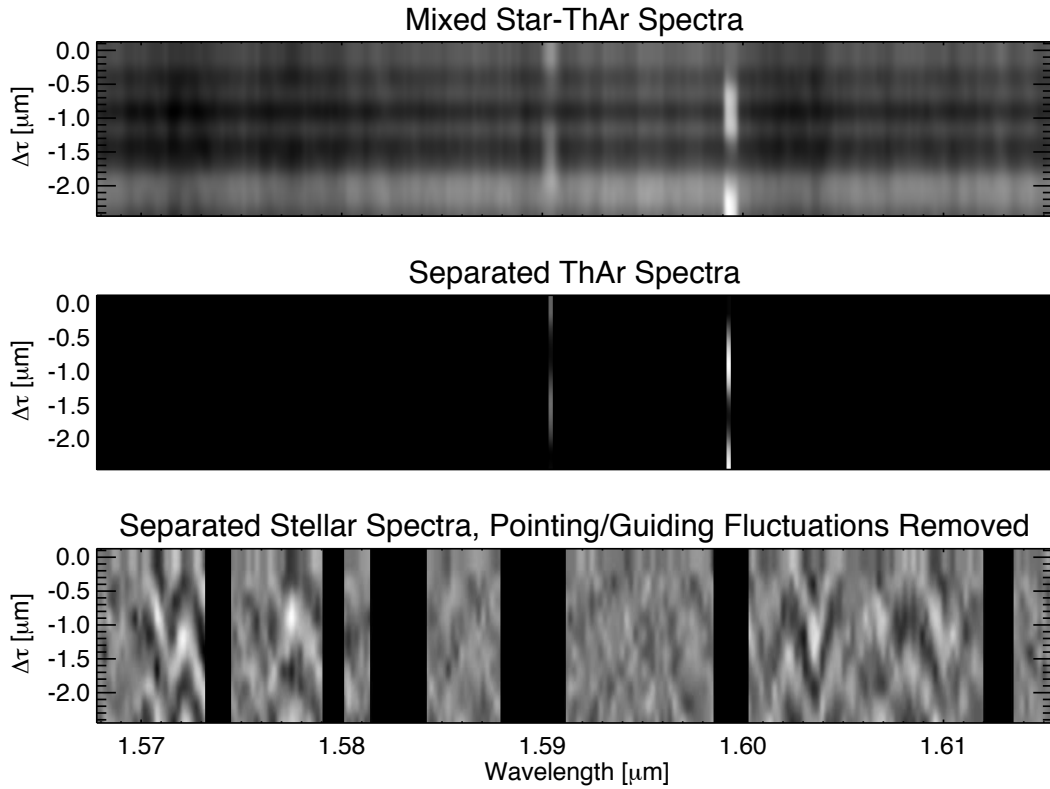
Figure 4.3 – TEDI spectra versus wavelength and $\Delta\tau$ for a small region in H-band. *Top:* Mixed stellar (GJ 699) and ThAr light. The ThAr emission lines dominate the signal, but underneath them lie the stellar spectra. *Middle:* Separated ThAr lines used to accurately and precisely determine the values of τ_0 and $\Delta\tau$. *Bottom:* The stellar spectra separated from the ThAr lines, after being normalized to remove effects from pointing/guiding fluctuations. The moiré fringes are most evident between 1.57 and 1.58 μm and between 1.60 and 1.61 μm, and these are due to two CO_2 absorption bands in the Earth's atmosphere. The less distinct fringes between 1.585 and 1.60 are due to the stellar absorption lines, and the phase of the stellar moiré fringes is highly sensitive to a Doppler shift. A_ν, B_ν and C_ν are fit to each wavelength channel to model the moiré pattern. Regions with strong ThAr lines or a poor fit to the complex visibility have been blocked out.

mixed star-ThAr spectra. This removes the thermal background and OH air-glow lines present in the spectra, and is equivalent to subtracting a nodded pair of exposures while still accounting for the effect of the interferometer.

The stellar spectra fluctuate due to changes in seeing and telescope guiding errors, which introduce flux variations that are a function of wavelength. To correct for this, the average shape of each of the 10 spectra is found by convolving each spectrum with a running boxcar mean filter. The shapes are used to normalize each of the ten spectra and remove these fluctuations. Various widths for the filter were tested to find that which produced the lowest radial velocity residuals. If the width of the filter is too large, it will not correct for fast fluctuations versus wavelength, and if it is too narrow it will remove the modulation introduced by the interferometer, which is the signal itself. We found the width with the lowest residuals to be 11 wavelength channels, or 4 resolution elements. After the stellar spectra are normalized, A_ν, B_ν and C_ν are linearly fit to each wavelength channel.

4.4 Referencing Delays

The LM-linear fitting routine determines the sizes of the phase steps between each spectrum, by ensuring sinusoidal variation of the ThAr lines, but does not determine the difference between the start delay of one set and the start delay of another set, where the start delay is the delay of the interferometer during the first exposure. To reference a complex visibility to a different start delay, we multiply it by an exponential phase change:

$$[B_v + iC_v] \rightarrow [B_v + iC_v]e^{2\pi\delta\tau v} \qquad (4.1)$$

where $\delta\tau$ is the change in delay. To correct for the difference in start delays between two complex visibility measurements, we fit for the $\delta\tau$ which reduces the phase difference between the separated ThAr complex visibilities of a template and epoch measurement. That $\delta\tau$ is then applied to the epoch stellar complex visibility, such that the template and epoch are referenced to the same start delay.

4.5   Telluric Calibration

Telluric calibration is performed by measuring the complex visibility of a rapidly rotating A-type or earlier "standard" star near the target, where only the telluric lines will contribute to the complex visibility, and subtracting the telluric complex visibility from that of the target. The standard complex visibility must be normalized to the target to account for the differences in flux, interferometer visibility and airmass, which will change the visibility as the telluric lines change in depth.

To normalize the standard star's complex visibility, it is first referenced to the same delay as the target, then divided by A_v of the standard and multiplied by A_v of the target, which accounts for the change in flux. Then, a boxcar filter versus wavelength fits a running multiplicative offset to the standard complex visibility to best match the target complex visibility for a given wavelength bin. A boxcar width of 51 pixels was found to give the lowest radial velocity residuals.

4.6   Measuring Radial Velocity Changes

As mentioned previously, a radial velocity change is measured between a template and an epoch measurement. The template measurement is identical to an epoch measurement, and is simply chosen as a radial velocity zero-point. With template and epoch A_ν, B_ν and C_ν, all referenced to the same delay start point, and the telluric effects at least partially removed, the radial velocity difference ΔRV can be measured using the procedure outlined in Section 2.1. This requires knowledge of the bulk delay τ_0. In order to measure the bulk delay, the phase of the complex visibility of the ThAr spectra must be modeled, which requires accurate knowledge of the wavelengths of the ThAr lines. Using a high-resolution spectrum of a ThAr emission lamp obtained for calibrating the CRIRES spectrograph (Kerber et al., 2008), we directly model the phase of B_ν and C_ν using several well-separated ThAr lines in J band, with the bulk delay as the only free parameter. The delay of the ThAr alone set for the template, which all subsequent sets are referenced to, is chosen for calculating the bulk delay. As stated in Section 2.3, any residual errors in the bulk delay can be corrected using radial velocity standard stars.

With τ_0 known, the template complex visibility is resampled onto a finer wavelength grid and multiplied by $e^{-i2\pi\tau_0\nu}$, then shifted by $\Delta\nu = \frac{\Delta\mathrm{RV}}{c}\nu$ using spline interpolation. The resulting complex visibility is multiplied by $e^{i2\pi\tau_0\nu}$, returning it to a slowly varying function of wavelength. This is then resampled onto the original wavelength grid, and the phase ϕ_ν, is compared to an epoch measurement. The ΔRV which minimizes the χ^2 of the phase difference between template and epoch, weighted by the formal uncertainty in the phase σ_{ϕ_ν}, is recorded as the measured change in radial velocity.

Instead of using the full TripleSpec bandwidth of 1.00 to 2.46 μm for measuring ΔRV, we currently limit our measurements to 1.48 to 2.15 μm. This bandpass has the highest instrument throughput, strong stellar absorption lines, and was found empirically to deliver lower residuals than when including the full bandwidth. Figure 4.4 plots the difference in phase converted to radial velocity between a ΔRV-shifted template complex visibility and a typical epoch complex visibility of GJ 699 for each wavelength channel in TripleSpec, and a high-resolution model of the Earth's telluric transmission function provided by Henry Roe using custom BFATS code (Roe, 2002). The 3 regions with the strongest ΔRV signal are in or near the water bands of the Earth's atmosphere near 1.45, 1.75, and 2.0 μm. The region near 1.45 μm was found to have large systematic errors, likely due to the heavy influence of telluric lines. Figure 4.5 plots the same phase difference, but for the reduced bandwidth. The clustering of residuals in the y-axis indicates spectral regions with narrow stellar features and strong radial velocity signal, with 1.7 to 1.8 μm containing the most signal in this bandpass, and the least telluric contamination. The measured ΔRV is that which shifts the template to minimize the weighted χ^2 value of these residuals.

4.7   Formal Uncertainties

Formal uncertainties for each ΔRV measurement are found by carrying the per pixel errors in each exposure through the reduction process. The error in each wavelength channel of each spectrum is calculated by summing in quadrature the read noise and photon noise in each contributing pixel. Formal uncertainties in A_ν, B_ν and C_ν are calculated during the linear portion of the combined linear-LM fitting routine. The uncertainties in B_ν and C_ν are passed to the ΔRV
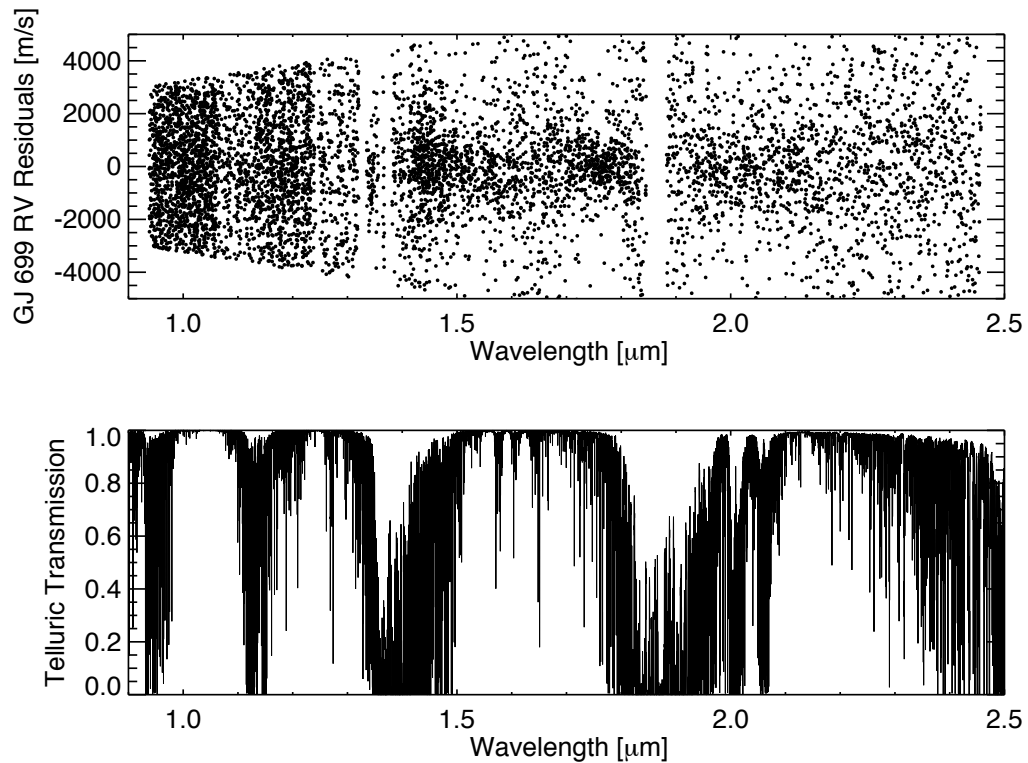
Figure 4.4 – Plot showing the radial velocity content of GJ 699 compared to the telluric absorption lines in the Earth's atmosphere. *Top*: Scatter plot of the phase differences for each wavelength channel between the ΔRV-shifted template complex visibility and an epoch complex visibility of GJ 699. For clarity, the phase differences have been converted to radial velocity differences using Equation 2.8. The clustering of residuals indicates regions with high radial velocity content, associated with spectral regions with many features. *Bot*: Synthetic transmission spectrum of the Earth's atmosphere provided by Henry Roe using custom BFATS code (Roe, 2002). The 3 regions of with the strongest ΔRV signal are in or near the water bands of the Earth's atmosphere near 1.45, 1.75, and 2.0 μm.
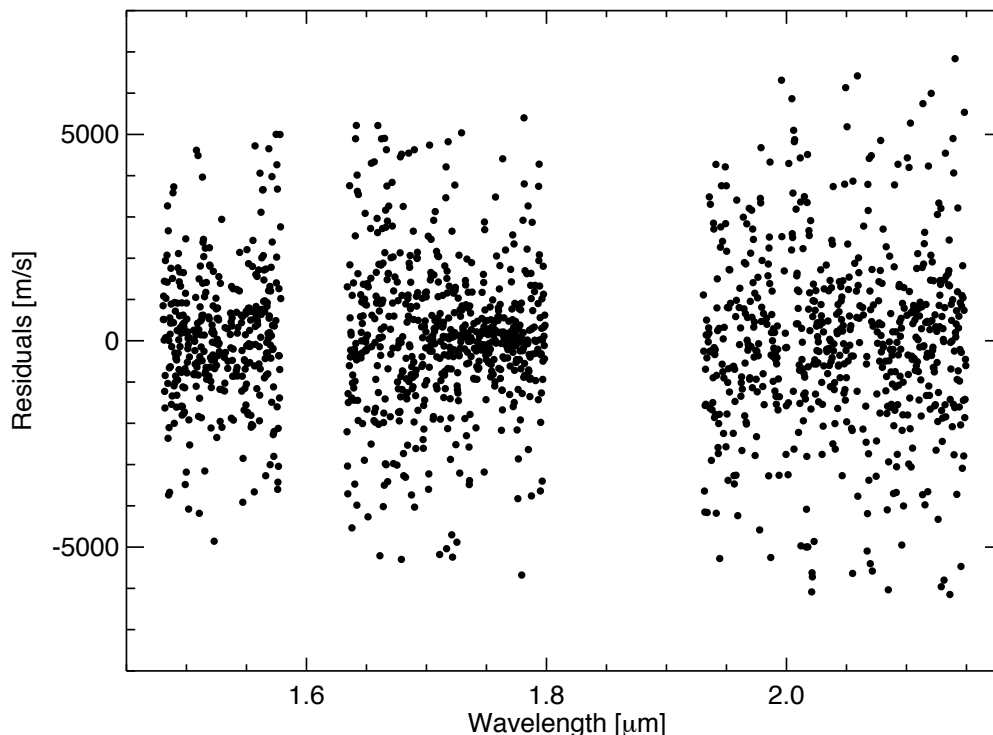
Figure 4.5 – Same as Figure 4.4, but for the reduced bandwidth used for the estimation of ΔRV of the target. The scatter is roughly 1 km s^{-1}, but the measured radial velocity depends on the weighted average of *all* of the wavelength channels. The clustering of points indicates spectral regions with narrow stellar features and strong radial velocity signal, with 1.7 to 1.8 μm containing the most signal in this bandpass. We currently limit the bandpass to 1.48 to 2.15 μm. The two gaps in coverage are from excessive telluric contamination near 1.62 μm, due to CO^2 in the Earth's atmosphere, which is intentionally ignored, and a gap in TripleSpec's wavelength coverage around 1.95 μm. The measured ΔRV is that which shifts the template to minimize the weighted χ^2 value of these residuals.

fitting routine and included to weight the phase difference between the shifted template and epoch. The formal uncertainty in ΔRV, $\sigma_{\Delta\mathrm{RV}}$, is calculated by converting the formal uncertainty in the phase of the complex visibility to an uncertainty in the radial velocity, and summing the radial velocity uncertainties in each wavelength channel in inverse quadrature:

$$\sigma_{\Delta\mathrm{RV}_\nu} = \frac{\sigma_{\phi_\nu} c}{2\pi\tau_0 \nu} \tag{4.2}$$

$$\sigma_{\Delta\mathrm{RV}} = \sqrt{\frac{1}{\sum \frac{1}{\sigma_{\Delta\mathrm{RV}_\nu}^2}}} \tag{4.3}$$

Figure 4.6 plots a histogram of the residuals and the cumulative distribution function of the radial velocities in Figure 4.5, normalized to their 1σ uncertainties. The cumulative distribution function indicates significant outliers. To reduce the effect of wavelength channel outliers, we remove those wavelength channels with the highest 3% of residuals and repeat the ΔRV fit. Currently, errors in the estimates of $\Delta\tau$ and errors in the delay referencing of complex visibilities are not included in the calculation of $\sigma_{\Delta\mathrm{RV}}$. Errors introduced by these effects are presumed to be small, given the high signal-to-noise of the ThAr calibration lines compared to that of starlight.
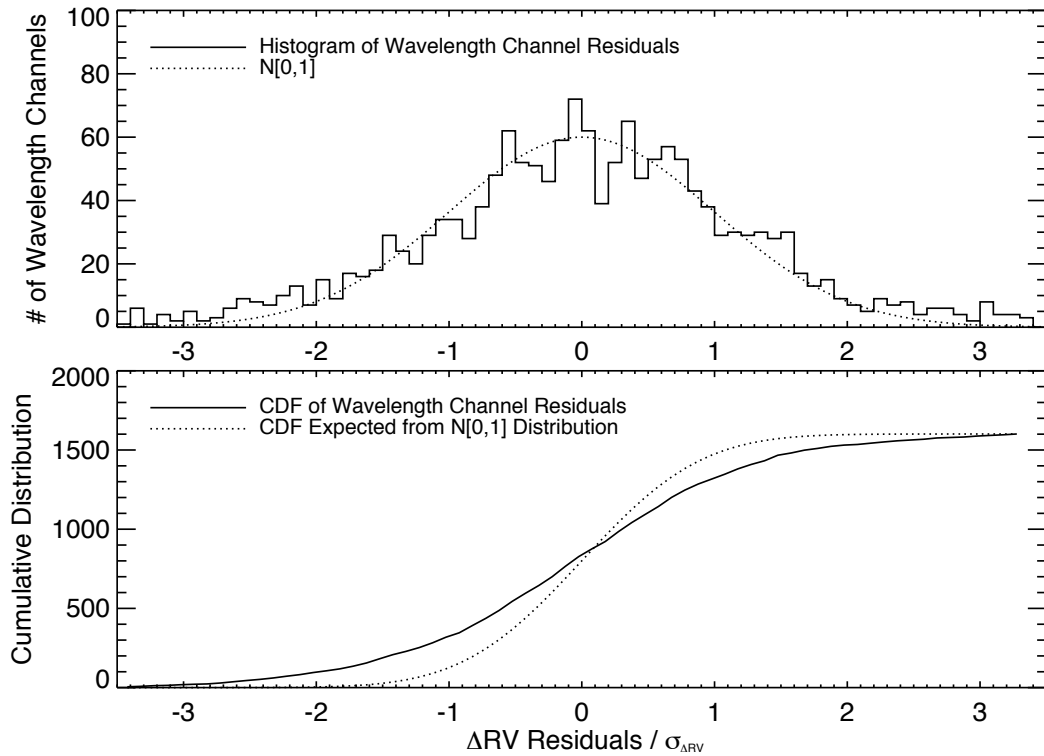
Figure 4.6 – *Top*: Histogram of the residuals in Figure 4.5 normalized to their
1σ uncertainties, with a normal distribution of mean 0 and standard deviation 1
included (N[0,1]). *Bottom*: Cumulative distribution function (CDF) of the resid-
uals, including that expected from the normal distribution. The difference indi-
cates significantly more outliers than expected from a Gaussian distribution. We
remove those wavelength channels with the highest 3% of residuals and repeat
the ΔRV fit to reduce the effect of outliers.

PERFORMANCE VERIFICATION

To test the precision of the TEDI radial velocity measurements, we conducted a commissioning campaign on GJ 699, also known as Barnard's Star. GJ 699 is a bright (*J*=5.24, *H*=4.83, *K*=4.52; Skrutskie et al., 2006), slowly rotating ($V_{rot} \sin i < 2.5$ km s^{-1}; Browning et al., 2010) M4 dwarf. Visible-wavelength radial velocity measurements limit potential radial velocity variations to less than 7.2 m s^{-1} (Endl et al., 2003), making it an ideal candidate for testing the radial velocity precision of TEDI.

5.1 Observations

Each of the 20 exposures which make up two ΔRV measurements of GJ 699, one for each fiber, was 30 seconds long, achieving a median signal-to-noise per wavelength channel of roughly 250 in H band for each spectrum. The 20 exposures took approximately 15 minutes of total observing time including exposure time, read time, time used to nod the star between fibers, and time between exposures used to change the delay and communicate between the TEDI control computer and TripleSpec control computer. We used the highest bulk delay available in TEDI of 4.6 cm, optimized for low projected rotational velocity.

We took 53 such observations of GJ 699, spread over 11 nights in June, July, August and September of 2010. That is, 53 ΔRV measurements with fiber A, and 53 with fiber B over 4 observing runs. For telluric calibration, we observed γ Ophiuchi, a V=3.75 A0V star 3.17 degrees away from GJ 699, with a projected rotational velocity of 210 km s^{-1} (Royer et al., 2007). At such a high projected

rotational velocity, any spectral features of the star are significantly broader than the interferometer comb spacing and do not contribute to the measured moiré pattern and complex visibility. We observed γ Ophiuchi roughly once for every 4 measurements of GJ 699, or once every hour.

Initially, the ΔRV residuals correlated proportionally with the expected ΔRV from the motion of the telescope relative to the barycenter of the Solar System. This is a consequence of applying an incorrect value for the bulk delay τ_0 in the data reduction procedure, as described in Section 2.3. To compensate we altered the τ_0 used in the reduction to minimize the ΔRV residuals, and found a best value of 4.654 cm. For future measurements, ΔRV measurements of known radial velocity standard stars will be used to measure the bulk delay for science targets.

5.2 Measurements

Figure 5.1 plots expected and measured ΔRV of GJ 699 over 11 nights in June, July, August and September of 2010, as well as the residuals. The radial velocities are expected to match the motion of the observatory with respect to the Solar System barycenter. The fibers are treated independently, with independent template measurements. The template measurements, used as the zero point for radial velocity changes, were taken on June 17, 2010 and have roughly the same signal-to-noise as the epoch measurements. Figure 5.2 plots the residuals for each fiber including the 1σ formal uncertainties, and Figure 5.3 plots a histogram of residuals, normalized to the formal uncertainties.

The root-mean-square (RMS) of the residuals is 36 m s^{-1} in fiber A and 37 m
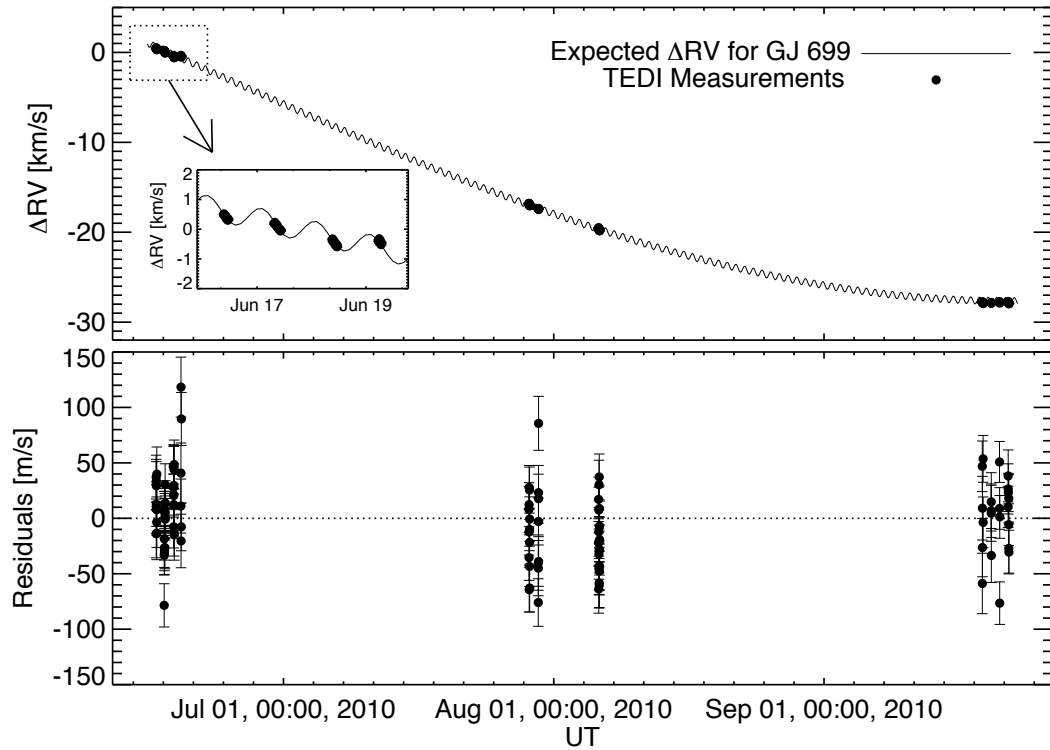
Figure 5.1 – *Top*: Expected and measured ΔRV's of GJ 699 with TEDI. The expected ΔRV's are calculated as the motion of the telescope relative to the Solar System barycenter. This includes a 30 km s^{-1} semiamplitude component from the Earth's orbit about the Sun, and a 300 m s^{-1} semiamplitude component from the Earth's rotation. *Top insert*: Detail of 4 nights in June, indicating clear recovery of the Earth's rotation. *Bottom*: Residuals including formal 1σ uncertainties.
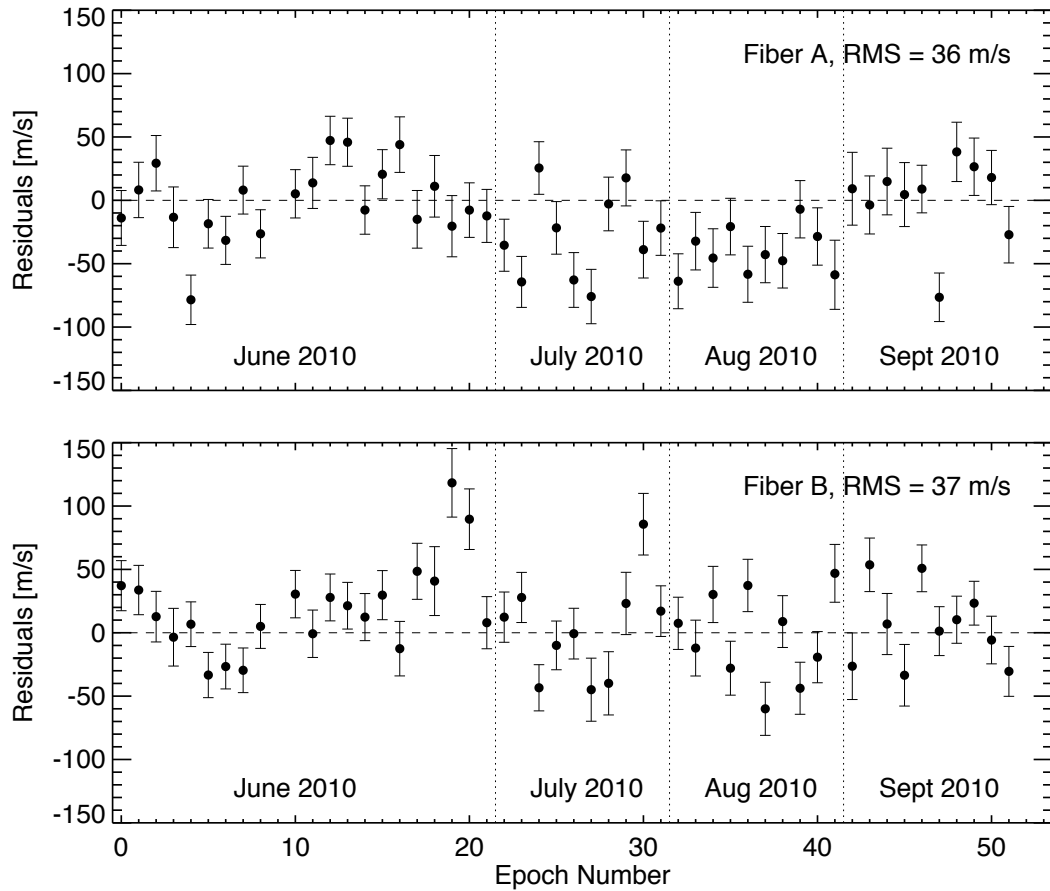
Figure 5.2 – Residuals for each TEDI ΔRV measurement of GJ 699 with formal 1σ uncertainties, equally spaced in order of observation, and grouped by observing run. The median 1σ uncertainty of the measurements is 21 m s^{-1}. *Top:* Residuals for fiber A, with a RMS variation of 36 m s^{-1}. *Bot:* Residuals for fiber B, with a RMS variation of 37 m s^{-1}. The fibers are treated independently, each with its own template measurement taken during the June run.

s^{-1} in fiber B. This is 1.76 times larger than the median formal uncertainty of 21 m s^{-1}. Figure 5.3 plots the distribution of residuals, including Normal distributions with standard deviations matched to the median formal uncertainty, and 1.76 times the median formal uncertainty. After inflating the formal uncertainties of the measurements by 1.76, and calculating the one-sided Kolmogorov-Smirnov (KS) statistic between the residuals and a normal distribution of mean 0 and standard deviation 1 (N[0,1]), we found the significance of the KS statistic to be 0.94. This indicates that the residuals are not significantly different from a normal distribution. The cumulative probability distributions of the normalized residuals and a N[0,1] distribution are plotted in Figure 5.4.

For purely photon noise, I expect the residuals 5.2 to be *white*; that is to say, a periodogram of the residuals should have equal power at all periods. A visual inspection of the residuals in Figure 5.2 indicates non-white behavior in the residuals. Figure 5.5 plots the Lomb-Scargle periodogram of the TEDI ΔRV residuals for fiber A and B, and for simulated residuals. The simulated residuals are randomly chosen from a Gaussian distribution with a standard deviation equal to the RMS of the TEDI measurements, meaning that the simulated residuals are white. The Lomb-Scargle Periodogram measures the power at various frequencies and periods for unevenly sampled data (Press & Rybicki, 1989), and is typically used for detecting planetary signals in radial velocity measurements (e.g. Wright & Howard, 2009). Unfortunately, the structure of the power in the Lomb-Scargle Periodogram depends highly on the cadences of measurements, making it difficult to asses whether the noise is purely white, or whether it is correlated. The power in the TEDI residuals and simulated white residuals is qualitatively similar for periods of an hour to a few hours, but for longer periods the TEDI residuals appear to have more power. This indicates the presence
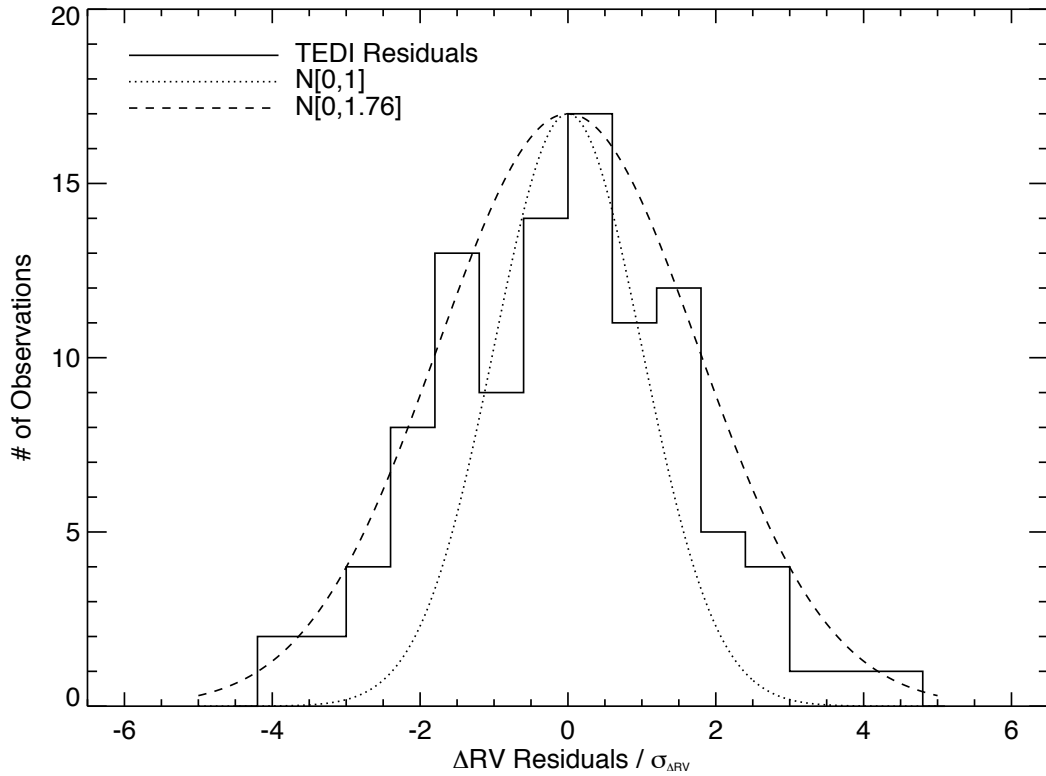
Figure 5.3 – Distribution of the ΔRV residuals for GJ 699, normalized by their formal 1σ uncertainties. The median formal uncertainty of the measurements is 21 m s^{-1}, however the RMS is 37 m s^{-1}. Normal distributions of mean 0 and standard deviations 1 and 1.76 are also shown. We include a Normal distribution with a standard deviation of 1.76 to account for the difference between the RMS and median formal uncertainty, and this distribution shows significantly better correspondence with the data.
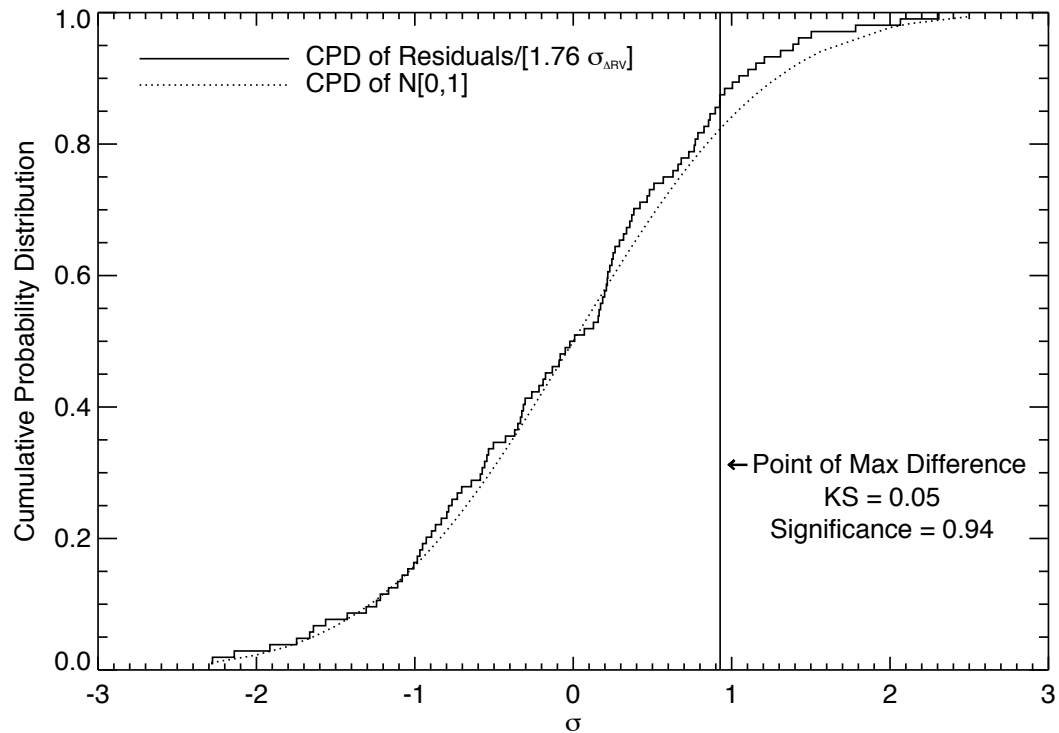
Figure 5.4 – Cumulative probability distribution (CPD) of the ΔRV residuals for GJ 699, normalized to the formal errors multiplied by 1.76, which is the ratio of the RMS of the residuals to the median formal uncertainty. This accounts for the difference between the median formal error and the measured RMS of 21 m s^{-1} and 37 m s^{-1}, respectively. The CPD of a Normal distribution with mean 0 and standard deviation of 1 (N[0,1]) is also shown. The one-sided Kolmogorov-Smirnov statistic is shown, and has a corresponding probability of 0.94, indicating that the distribution of residuals does not differ significantly from a Normal distribution.

of *correlated* noise in addition to white noise.

To address the presence of correlated noise, I divided the measurements into bins of various temporal widths, and calculate the sample standard deviation of the residuals within each bin. For a given bin width in days, I take the mean of the sample standard deviations of each of the bins which contain at least 2 measurements within them. This procedure is similar to the one developed by (Shannon & Cordes, 2010) for analyzing timing noise in radio pulsars. Figure 5.2 plots the mean sample standard deviation for a given bin width, for both fiber A and B measurements, with error bars indicating the standard deviation of the mean. For purely white noise, I expect the mean standard deviation to be constant with bin width. The trend in both fibers suggests *stationary correlated noise* in addition to white noise in the GJ 699 residuals. The rising mean sample standard deviation with bin width shows that the errors are correlated, and the plateau past 1 day shows that the errors are stationary. The trend in fiber B is similar, but with larger variation short of 0.01 days (15 minutes). Figure 5.2 establishes the performance of TEDI for different timescales.

The individual ΔRV measurements can be averaged together by epoch number to reduce the residuals. Figure 5.7 plots the RMS of the residuals versus averaging bin size, in units of number of epochs. The reduction in RMS is not as fast as would be expected from white noise only. We model the reduction in RMS as a function of white noise σ_W and correlated component σ_F, such that RMS $= \sqrt{\sigma_W^2/N_{bins} + \sigma_F^2}$. The correlated noise σ_F indicates the best precision achievable over these timescales which cannot be reduced by binning measurements. We calculate a best fit where $\sigma_W = 33$ m s^{-1}, and $\sigma_F = 15$ m s^{-1}.

The source of the correlated noise is unlikely to be astrophysical, since prior
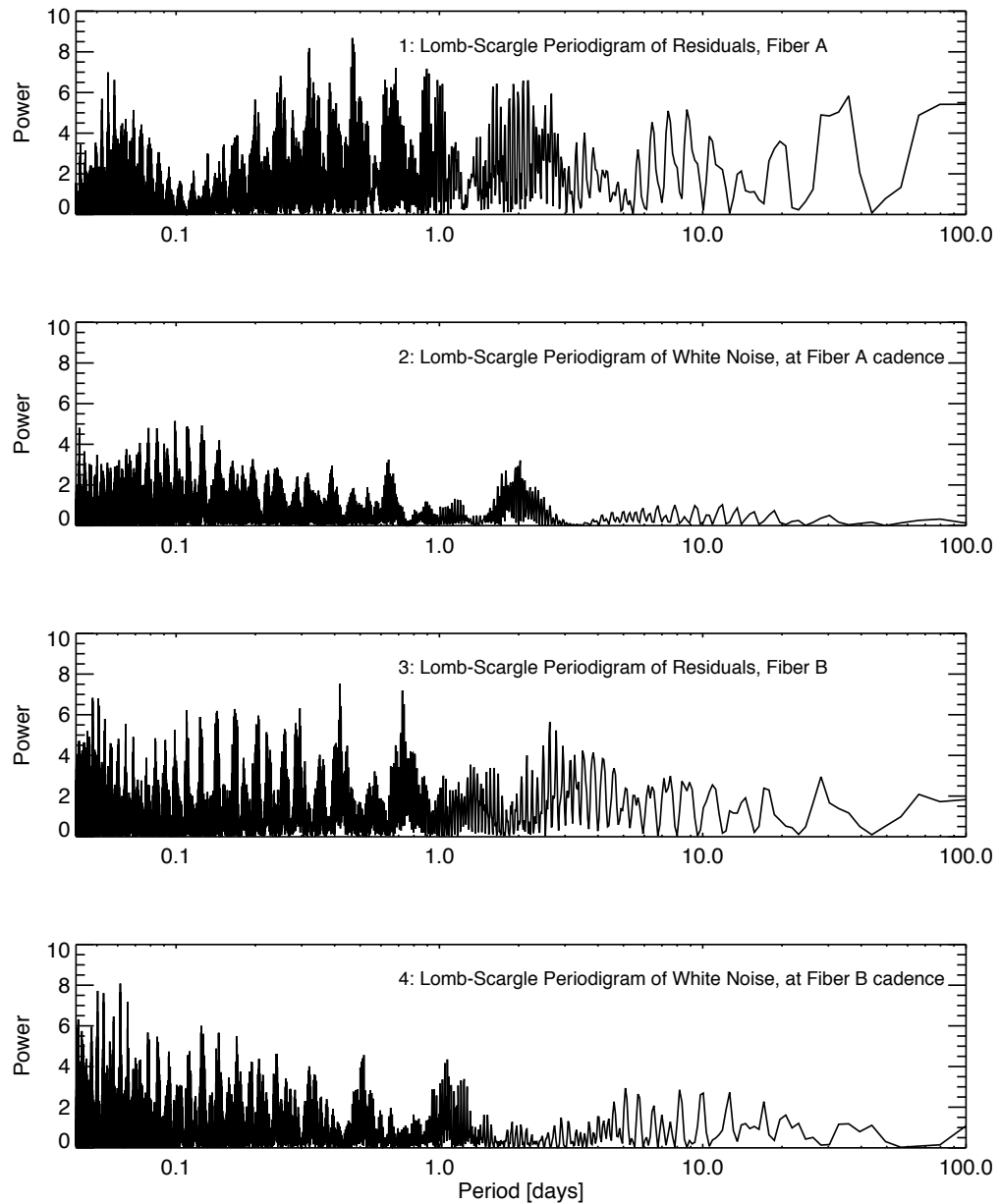
Figure 5.5 – Lomb-Scargle periodograms of TEDI residuals, and simulated residuals. The simulated residuals are randomly chosen from a Gaussian distribution with a standard deviation equal to the RMS of the TEDI measurements, meaning that the simulated residuals are white and stationary.
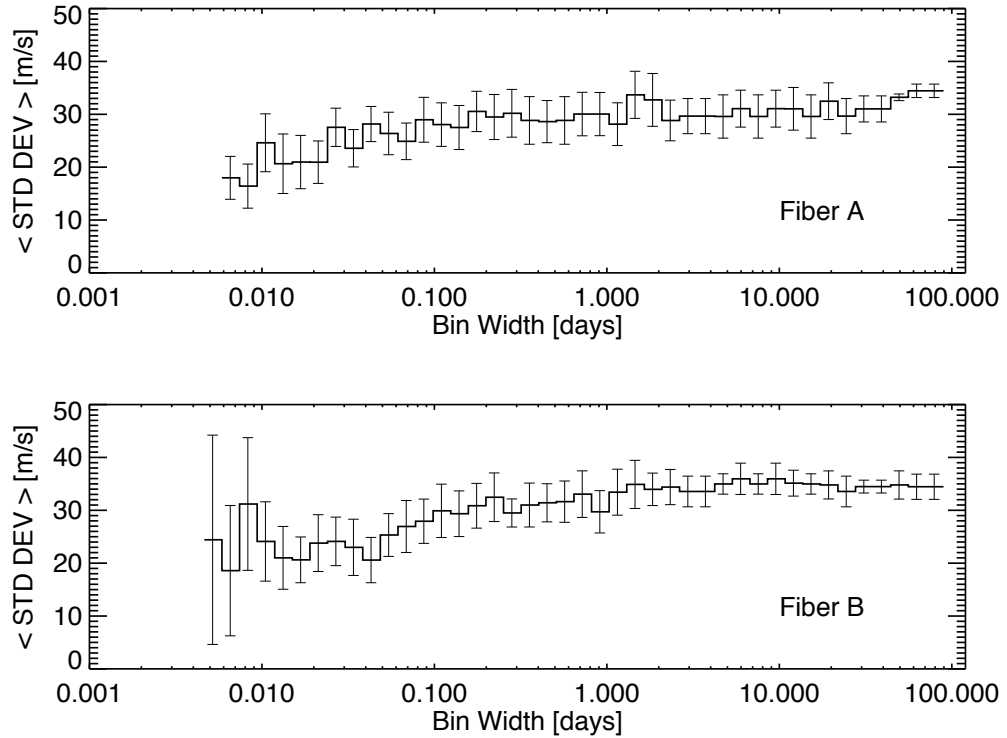
Figure 5.6 – Plot of the performance of TEDI ΔRV on GJ 699 for different timescales. The residuals of the GJ 699 measurements are binned into bins of different widths in units of days (x axis). For each bin width and set of corresponding bins, the sample standard deviation is calculated within every bin which has at least 2 residual measurements within it. The mean of the sample standard deviations of the bins is plotted, and the error bars indicate the standard deviation of that mean. The trend in fiber A is consistent with *stationary correlated noise*: increasing residuals for larger bin widths, then plateauing. The trend in fiber B is similar, but with larger variation short of 0.01 days (15 minutes). For purely white noise, the mean standard deviation is expected to be constant with bin width.

ΔRV measurements at visible wavelengths show less than 10 m s^{-1} of variation of long timescales. TEDI has many moving parts, and is attached to a moving telescope, with the airmass and humidity of the Earth atmosphere changing and the telluric absorption lines also changing. The ΔRV measurements are also changing due to the motion of the telescope around the Solar System barycenter. In the following chapter I simulate TEDI data, simulating the expected ΔRV measurements. I find that incomplete calibration of the telluric lines combined with barycentric motions produces qualitatively similar residuals to those measured on GJ 699. This is true even if the telluric transmission spectrum is not changing.
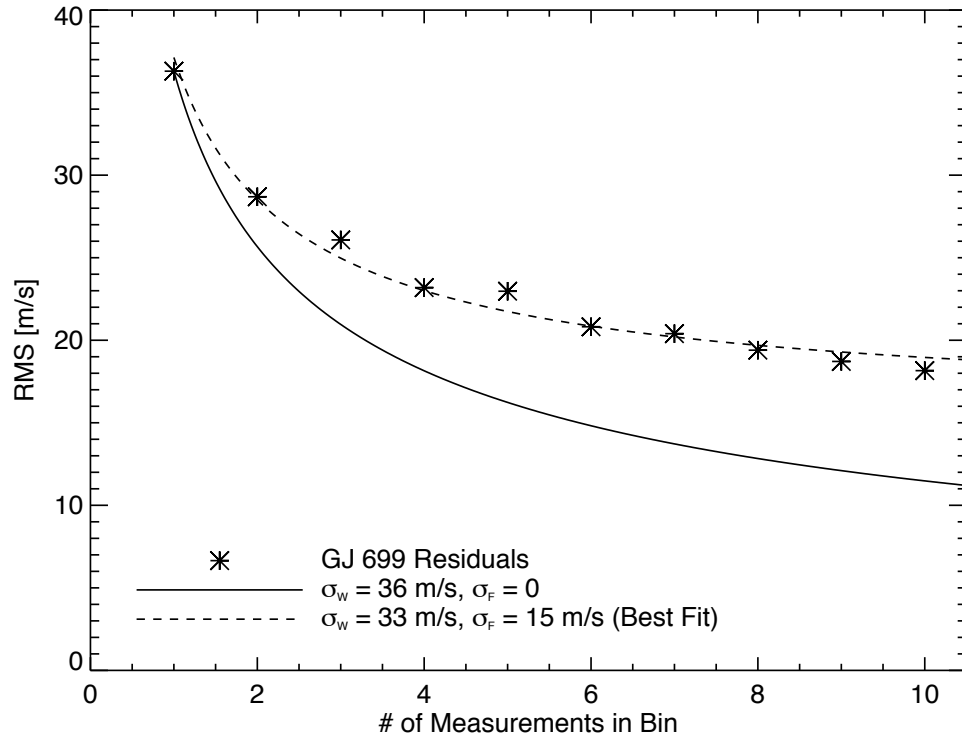
Figure 5.7 – RMS of the ΔRV residuals for GJ 699 as a function of number of measurements binned together. Included are plots indicating what is expected from a white noise component σ_W and a correlated noise component σ_F: $\mathrm{RMS}(N_{\mathrm{Bins}}) = \sqrt{\sigma_W^2/N_{\mathrm{Bins}} + \sigma_F^2}$, where N_{Bins} is the bin size. The solid line indicates that which would be expected from only white noise matched to the RMS when $N_{\mathrm{Bins}} = 1$. The dashed line is fit to the $\mathrm{RMS}(N_{\mathrm{Bins}})$ and indicates a white noise component 33 m s^{-1} which can be reduced by binning, and a correlated noise component of 15 m s^{-1} which cannot.

CHAPTER 6

SYSTEMATIC ERRORS

6.1 Telluric Calibration Errors

I expect the largest source of error in the measurements to be due to insufficient removal of telluric contamination in the complex visibilities. TEDI does not fully resolve the narrowest features of either the stellar or telluric lines. When unresolved, high resolution features of the stellar and telluric spectrum will mix and alias to lower resolution features which will contaminate the complex visibilities. For small ΔRV changes, the aliased spectrum is not expected to introduce a significant effect, but for large changes, such as the motion of the telescope relative to the Solar System barycenter, the aliased spectrum is expected to introduce errors. The effect of the telluric and stellar mixing on the ΔRV measurement will depend on stellar type, projected rotational velocity, radial velocity, airmass of the target, and the telluric line strengths, as all of these parameters will change the aliased spectrum, and contaminate the complex visibilities differently.

To investigate this effect, I simulated mixed stellar and telluric spectra and telluric calibration spectra, and carry them them through the analysis procedure including the expected changes in radial velocity of GJ 699. I used a high-resolution model spectrum of a main-sequence star with a 3200 K effective temperature provided calculated using the PHOENIX model atmosphere code (e.g. Fuhrmeister et al., 2005), and a high-resolution model of the telluric transmission spectrum calculated for Palomar Observatory by Roe (2002). Figure 6.1 plots the model spectra used in the simulation.
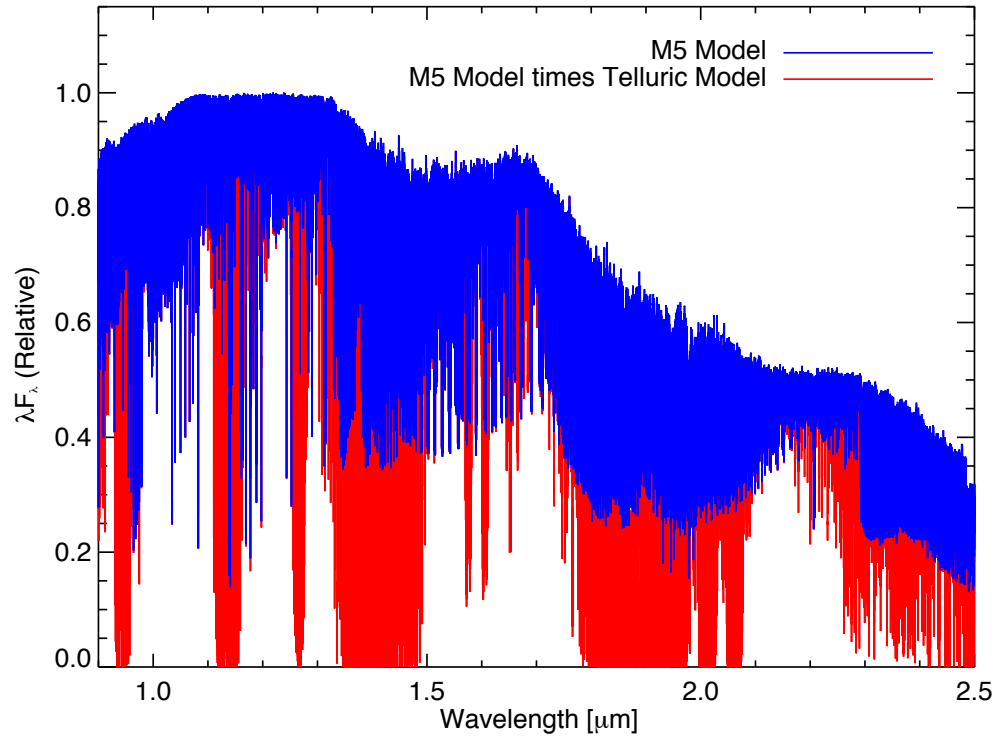
Figure 6.1 – High resolution model spectra used in the simulation of TEDI data. *Blue*: Flux from the PHOENIX model stellar spectrum (e.g. Fuhrmeister et al., 2005). The spectrum simulates a main-sequence star with a 3200 K effective temperature, corresponding roughly to an M5 dwarf. *Red*: The additional absorption lines introduced onto the stellar spectrum by the model telluric transmission function (Roe, 2002).

I convolved the stellar model with a 1 km s^{-1} rotational broadening kernel before shifting it by an input radial velocity, multiplying it by the telluric transmission model, multiplying it by the 10 interferometer transmission combs corresponding to the 10 phase steps in a phase set, and finally convolving it with a Gaussian profile to simulate the TripleSpec line spread function. I matched the signal-to-noise of the simulated spectra to that of the GJ 699 data, and added Poisson noise to simulate photon noise. After this, I fed the spectra into the current data reduction algorithm described in Section 4, using the same wavelength regions of 1.48 to 2.15 μm for measuring the change in radial velocity. The simulated data does not contain fluctuations due to telescope pointing and guiding, nor ThAr lines, and the delays are assumed to be known exactly. **The only changing parameter in the simulated data is the expected radial velocity of GJ 699 due to the motion of the telescope around the Solar System barycenter.**

The expected radial velocities of the GJ 699 measurements were used as inputs, including the bulk radial velocity of the star relative to the Solar System barycenter of -106.8 km s^{-1}, previously measured by Evans (1996). Figure 6.2 plots the resulting residuals and 1σ uncertainties based on photon noise for simulations with telluric contamination and calibration, and for simulations without any telluric contamination or calibration. The RMS of the simulated residuals with telluric effects is 45 m s^{-1}, roughly a factor of 2 higher than that expected from photon noise, whereas the RMS of the simulated residuals without telluric effects is 13 m s^{-1}, matching that expected from photon noise. The residuals show slow fluctuations, which correlate strongly with the expected radial velocities from the motion of the telescope relative to the Solar System barycenter. I interpret these errors as arising from the combination of uncalibrated mixing

of stellar and telluric lines in the simulated data, combined with large radial velocity shifts. It is not certain whether this is the source of the systematic noise in the TEDI measurements, since the stellar and telluric models are not perfect representations of GJ 699 nor the true telluric transmission spectrum, but this analysis suggests it is a plausible explanation.

Figure 6.1 plots the simulated performance on various timescales using the binning technique described in Chapter 5 and plotted in Figure 5.2. The simulated residuals are consistent with white noise for bin widths shorter than several days. For longer bin widths there is a rise in the mean sample standard deviation consistent with correlated noise. Unlike the measured GJ 699 residuals, the simulated residuals do not show an obvious plateau and are not as obviously stationary. Since the only changing parameter in the simulation is the input radial velocity of the star, I repeated the simulations for an array of ΔRV shifts, evenly distributed from -30 km s^{-1} to 30 km s^{-1}, matching the range of expected ΔRV shifts from the motion of the telescope around the Solar System barycenter. Figure 6.1 plots the residuals versus input radial velocity shift, for simulations with and without telluric interference and calibration. The behavior of the residuals is linear near 0, but becomes non-linear for shifts of more than 5 km s^{-1}. The residuals peak at roughly 400 m s^{-1} for ΔRV shifts of 3 km s^{-1}. This severely limits the performance of TEDI.

Uncalibrated mixing of telluric lines can be illustrated by considering the effect in Fourier space. Figure 6.5 is identical to Figure 2.2, showing the TEDI response in Fourier space, but includes the Fourier transform of the model telluric spectrum used in the simulations. Multiplying the stellar and telluric spectra together corresponds to a convolution in Fourier space. That will lead to high and

64
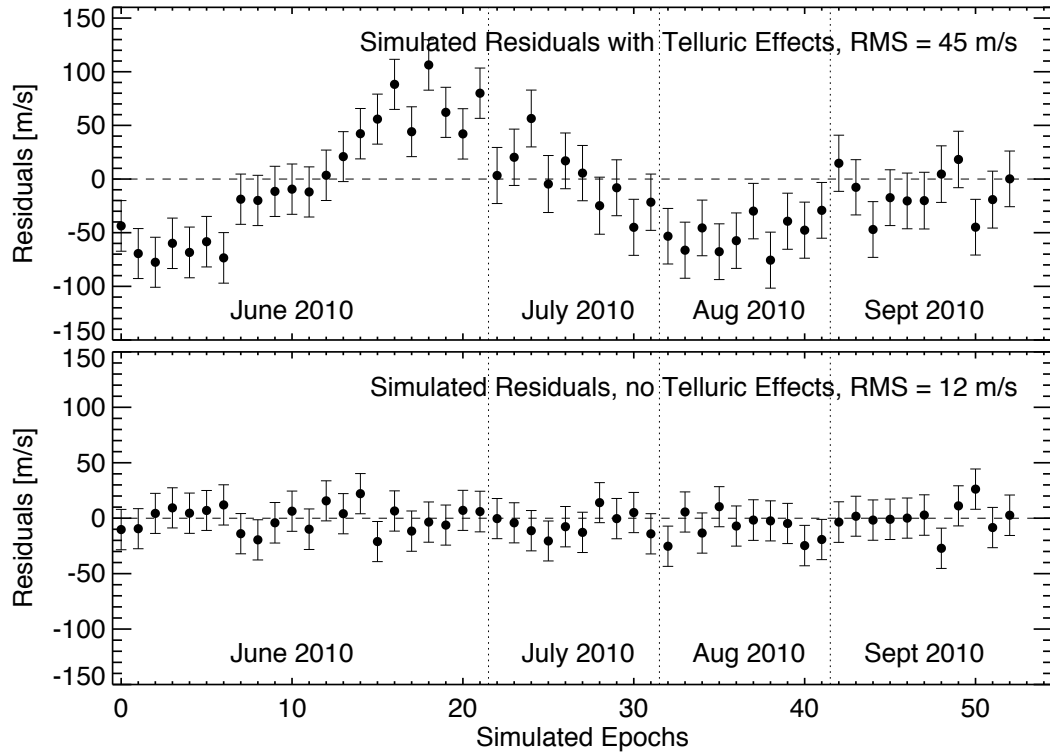
Figure 6.2 – Simulated TEDI measurements of GJ 699 including calculated 1σ uncertainties based on photon noise. *Top*: Simulated residuals including telluric contamination and calibration, versus epoch number, showing an RMS of 45 m s^{-1} despite a median 1σ uncertainty of 25 m s^{-1}. *Bottom:* The same, but without telluric contamination or calibration, and the RMS matches that expected from photon noise of 13 m s^{-1}. The simulations suggest that insufficient calibration of the telluric contamination is currently limiting TEDI performance. The 1σ uncertainties are significantly smaller for the simulations without telluric contamination because the telluric transmission reduces the photon counts at the edges of H and K bands.
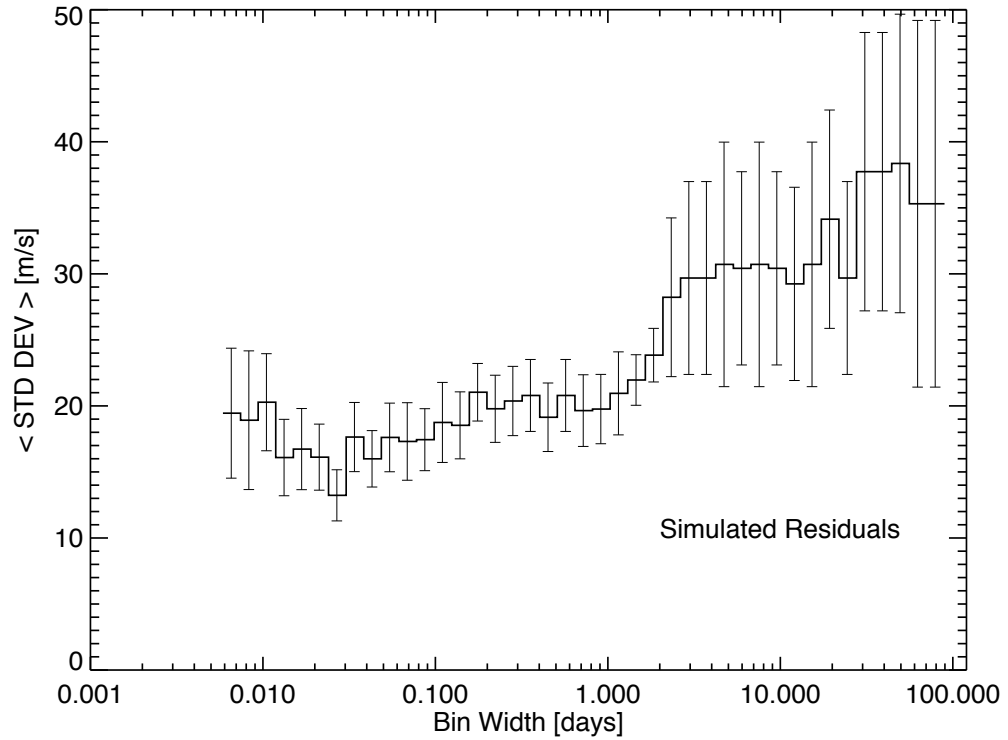
Figure 6.3 – Plot of the simulated performance of TEDI ΔRV on GJ 699 for different timescales, identical to Figure 5.2 but with simulated residuals. The simulated residuals are consistent with white noise, up until timescales of 2-3 days at which point there is a rise in the mean sample standard deviation consistent with correlated noise. Unlike the actual GJ 699 data, the simulated residuals at not as obviously stationary, without a clear plateau.
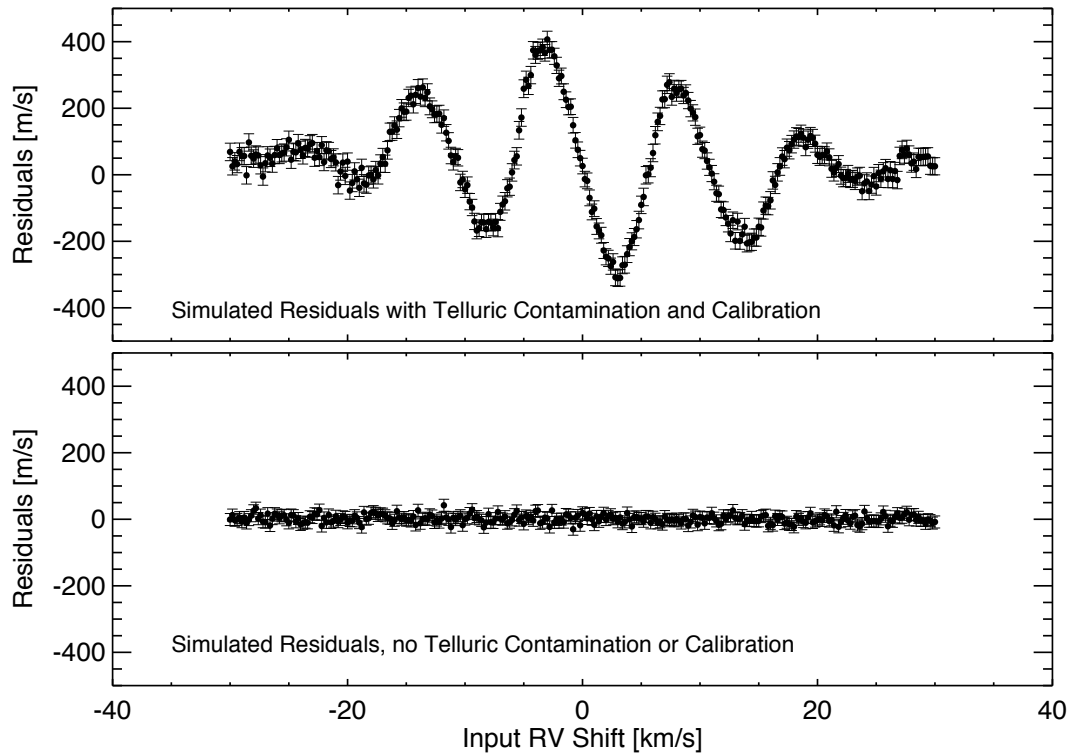
Figure 6.4 – Simulated TEDI residuals versus input ΔRV, spanning -30 to 30 km s^{-1}, matching the range of expected ΔRVs from the motion of the telescope around the Solar System barycenter. *Top*: Simulated residuals including telluric contamination and calibration. The residuals are linear near 0, but become nonlinear for shifts greater than 5 km s^{-1}. *Bottom*: Simulated residuals without telluric contamination or calibration. The residuals are consistent with photon noise.

low resolution features aliasing into the TEDI window. The aliased features will add an aliased component to the TEDI data product which cannot be calibrated by TEDI measurements alone. For small changes in the Doppler shift, the effect on the TEDI data product will be linear as a consequence of a Taylor series expansion. But, for large changes in radial velocity, due to the barycentric motion of the Earth, the aliased component introduces non-linear errors. This is consistent with the simulations, which show smaller ΔRV residuals for smaller barycentric motions (< 100 m s^{-1}), but larger residuals for large barycentric motions (Figure 6.1).

The conventional R=10^5 spectrograph has a significantly larger window, and captures much more of the high resolution features in both the stellar and telluric Fourier transforms. Bean et al. (2010) found a 5 m s^{-1} noise floor when using the R=10^5 CRIRES spectrograph to measure precise radial velocities, and attributed to the noise to uncalibrated telluric lines. Fully forward-modeling the TEDI data product using stellar and telluric models could account for this component, but current stellar and telluric models do not appear to be accurate enough to reproduce the aliased effect. This is evidenced by the fact that the simulated residuals in Figure 6.2 do not accurately reproduce the measured residuals in Figure 5.2, although they are qualitatively similar.

6.2   Fiber Illumination Errors

TEDI does not currently have a mechanism for supplemental scrambling of the output of the fibers, as discussed in Section 3.4. This could result in slightly different cavity illumination between the ThAr calibration lamp and the starlight,
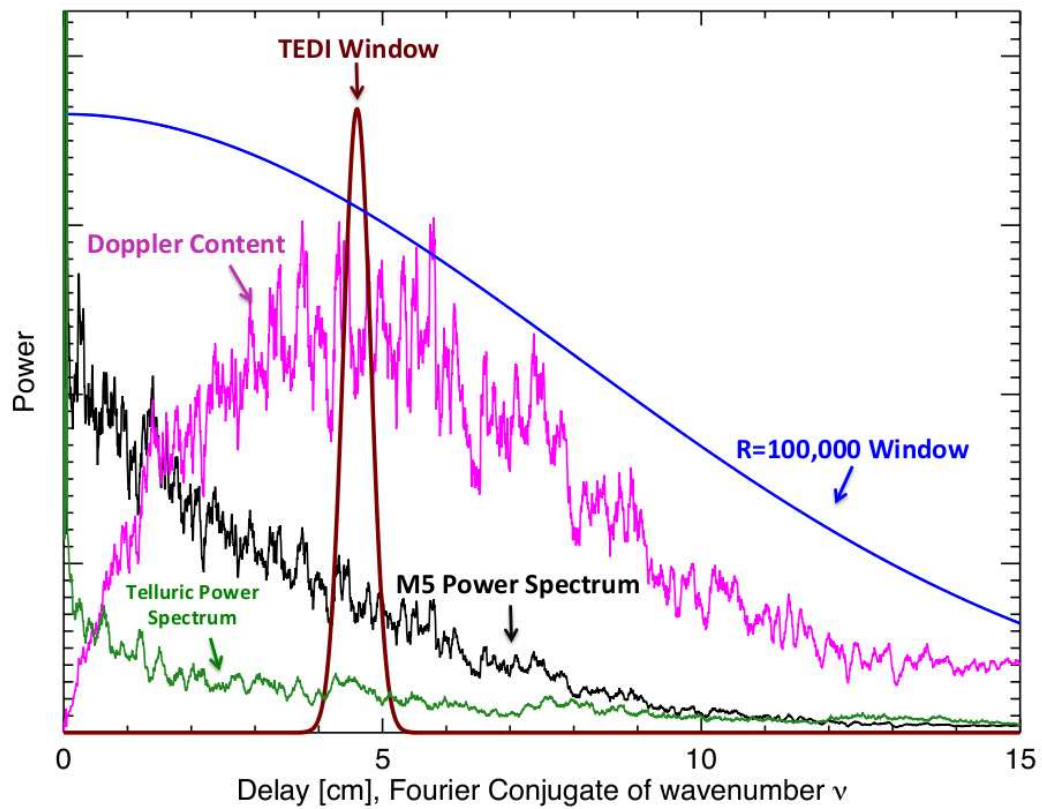
Figure 6.5 – Fourier response of TEDI, identical to Figure 2.2, but including the Fourier transform of the model telluric transmission spectrum (in green). The stellar and telluric Fourier transforms are convolved when the spectra are multiplied, leading to aliasing of high and low resolution features into the TEDI window. The aliased features cannot be measured by TEDI alone, and require either forward modeling or much higher resolution to resolve.

and can potentially introduce errors into the measured ΔRV. The effect was tested by moving an artificial source on the input fiber tip. To do this, Jerry Edelstein and I built a fiber-fed telescope which we mounted on the top of TEDI to recreate a 1 arcsecond "star" at nearly the same etendue as the 200" telescope. We illuminated the fiber with a krypton gas discharge lamp, which has infrared emission lines in H and K bands. Moving the illumination of the TEDI input fiber by 0.5 arcseconds was found to introduce a 45 m s^{-1} systematic offset in the measured ΔRV (Figure 6.6). This could potentially introduce stellar radial velocity offsets if the internal TEDI guider were guiding the starlight to the edge of the fiber core, rather than the center. However, when the fiber is illuminated 0.5 arcseconds off-axis, the images of the krypton emission lines on the spectrograph detector show a clear double-peaked slit profile, due to an annular shape of the output fiber illumination combined with slit-losses (Figure 6.7). The slit profiles of GJ 699 data do not show double-peaked slit profiles, and therefore I do not believe this effect is contributing significantly to the residuals.

6.3   TEDI Error Budget

With an understanding of the noise sources in the TEDI ΔRV measurements, I can estimate the error budget of the instrument. Simulating TEDI data indicates that the largest source of error is from insufficient calibration of telluric lines, and that these errors depend strongly on the ΔRV introduced by the motion of the telescope around the Solar System barycenter. In the case of the GJ 699 data, evidence suggests the effect introduces roughly 30 m s^{-1} of correlated stationary errors into the measurements, but that is specific to the barycentric corrections for that data set. If the data had a different set of barycentric corrections, I ex-

pect the telluric effects to have a different contribution to the error budget. The contribution could be smaller or larger, and possibly exceed 100 m s^{-1} based on Figure 6.1.

Assuming the effects of insufficient telluric calibration can be overcome, the next largest contributor to the TEDI error budget is photon noise. Carrying photon noise through the TEDI data analysis pipeline, we expect it to contribute 21 m s^{-1} of error to each measurement. The errors in the ΔRV measurements due to photon noise are expected to be white, as opposed to correlated. GJ 699 is a very bright M dwarf, and achieving a similar performance on fainter M dwarfs requires significantly more observing time. The next chapter discusses an M dwarf survey with TEDI, and the expected and measured RMS ΔRV performance of TEDI on fainter targets.
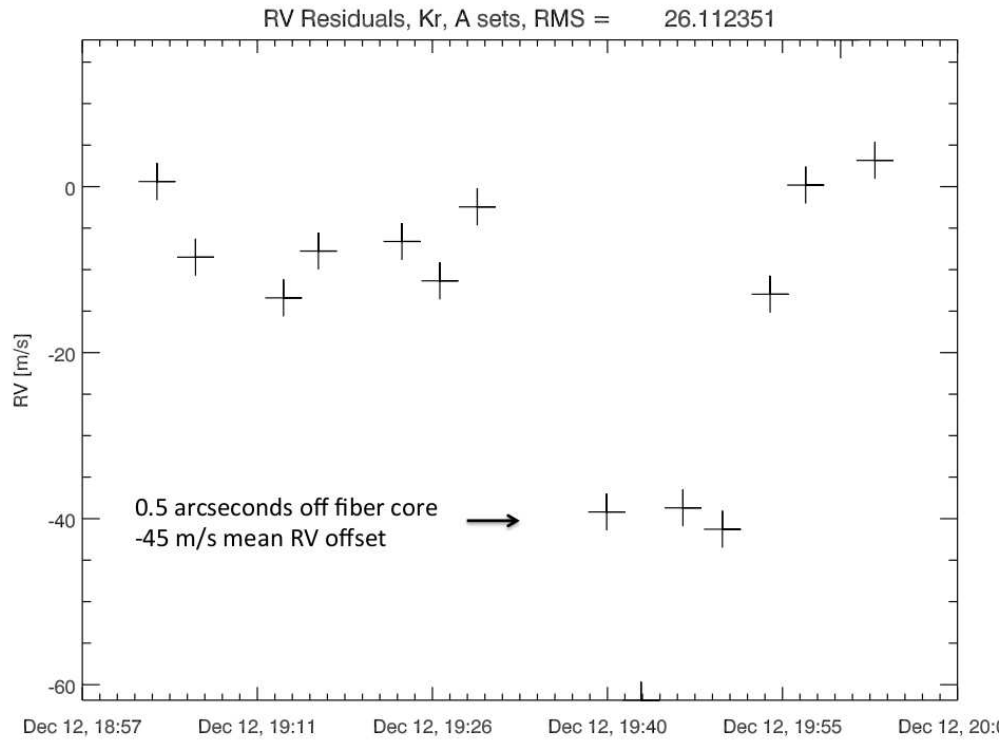
Figure 6.6 – ΔRV of a Krypton emission lamp through TEDI. When the focus of the lamp was adjusted to by the equivalent of 0.5 arcseconds away from the fiber core, it introduced of 45 m/s offset into the measured radial velocities.
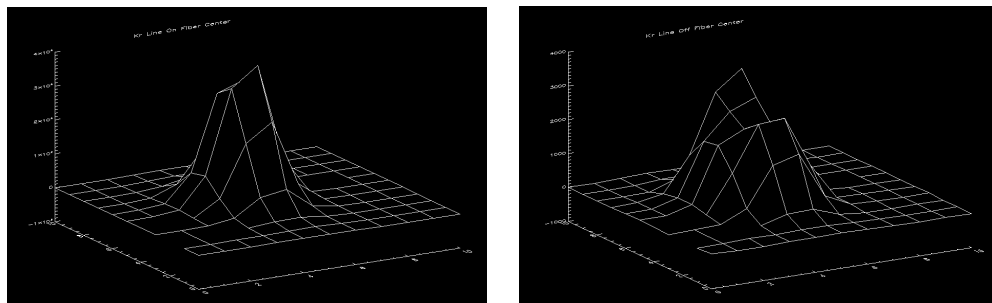
Figure 6.7 – Images of Krypton emission lines on the TripleSpec detector. *Left:* Image with the light focused on the fiber core. *Right:* Image with the light focused 0.5 arcseconds away from the fiber core, corresponding to the offset ΔRV measurements.

CHAPTER 7

SURVEY OF NEARBY M DWARFS

In February of 2011 I performed a radial velocity survey of metal-rich nearby M dwarfs with TEDI, with the goal of either detecting or ruling-out the presence of short-period orbiting exoplanets. The motivation for TEDI is to enable detection and mass-measurement of terrestrial extrasolar planets; however, the current performance limits detection to close-in gas giant planets, and only around very bright M dwarfs. Visible-wavelength radial velocity surveys indicate that gas-giant planets are rare around M dwarfs, with less than 20% of M dwarfs harboring planets greater that 0.8 M_{Jup} within 2.5 AU (Johnson et al., 2007). Recently, new techniques to measure accurate metallicities of M dwarfs indicate that those M dwarfs which host gas-giant planets are systematically metal-rich, extending the planet-metallicity correlation to M dwarfs (Johnson & Apps, 2009; Rojas-Ayala et al., 2010). We systematically bias our survey towards metal-rich M dwarfs, where detections or non-detections have higher scientific impact.

7.1 Survey Sample

I restrict the survey to M dwarfs within 8 parsecs of the Sun, without nearby stellar companions, with metallicity measurements that that are super-Solar ([Fe/H] > 0.0) and are available for observations in February from Palomar (declination $\delta > -30°$, right ascension α between 3 and 17 hours). The 8 Parsec Sample is a census of all stars within 8 parsecs of the sun, compiled by Reid & Cruz (2002) by combining the Catalogue of Nearby Stars (CNS3; Gliese & Jahreiss, 1991) with spectroscopy from the Palomar/Michigan State University survey (e.g. Reid et al., 1995), and stars identified by 2MASS (Skrutskie et al., 2006). The

8 Parsec Sample is estimated to be complete for stars with $M_V < 14$, corresponding to dwarfs earlier than M5. The 8 Parsec Sample contains 84 dwarf systems later than M0 with declination $\delta > -30°$. Of these, I removed M dwarfs with known planets and those with published non-detections in Endl et al. (2003).

Many of the remaining M dwarfs are part of multiple systems, which are mostly binary but also triple, quadruple and even quintuple systems. Oppenheimer et al. (2001) compiled a list of all of the known multiple systems in the nearest 8 parsecs, as part of a coronagraphic survey for nearby companions. Many are visual binaries, but some are also radial velocity binaries, and coronagraphic binaries discovered in their survey. Removing all M dwarfs with stellar companions with separations of less than 500 AU, the survey count reduces to 47.

Rojas-Ayala et al. (2010) developed a technique for measuring M dwarf metallicities using TripleSpec spectra. The technique has been used to measure metallicities of many M dwarfs in the 8 Parsec Sample. Techniques for measuring metallicities of Sun-like stars using visible-wavelength high-resolution spectroscopy have produced notoriously unreliable measurements for M dwarfs, due mainly to their lower flux at visible wavelengths. The Rojas-Ayala et al. (2010) technique uses medium-resolution spectra in K band, where M dwarfs are significantly brighter. Of the 47 M dwarfs in the sample, 34 have metallicity measurements using this technique. Of those with measurements, 14 have super-Solar metallicities. Of those 14, 10 are available in February. These are listed in Table 7.1.

In addition to the 10 metal-rich M dwarfs, I also observed two radial velocity standards, GJ 281 and GJ 411, which have both shown less than 10 m s^{-1} of long

Table 7.1. – February 2011 TEDI Targets

CNS3 Name	V	H	Spectral Type	Expected $\sigma_{\Delta RV}$ [m s^{-1}]	$V_{rot} \sin i$ [km s^{-1}]
RV Standard Stars					
GJ 411	7.48	3.64	M2	22	< 1.0[c]
GJ 281	9.61	6.09	M0	67	
Survey Targets					
GJ 3323	12.16	7.07	M4	105	< 3.2[a]
GJ 205	7.92	4.15	M1	27	
GJ 251	9.89	5.53	M3	52	
GJ 285	11.12	6.00	M4.5	64	4.6[b]
GJ 388	9.43	4.84	M4.5	37	12.42[b]
GJ 402	11.66	6.71	M4	89	< 2.5[b]
GJ 406	12.54	6.48	M6.5	80	< 2.5[b]
GJ 555	11.35	6.26	M4	73	
GL 628	10.12	5.34	M3.5	48	
GJ 643	11.70	7.06	M3.5	105	< 2.7[a]

[a]Jenkins et al. (2009)

[b]Browning et al. (2010)

[b]Marcy & Chen (1992)

term variation as part of the Endl et al. (2003) survey for exoplanets orbiting M dwarfs. The radial velocity standards serve as a consistency check, to monitor the radial velocity performance of TEDI.

Table 7.1 lists the February 2011 targets, with brightnesses, stellar parameters, and expected TEDI radial velocity precision for 5 minutes of integration time.

7.2 Observations

The targets were observed over an 8-night observing run in February of 2011, with 3.5 of the nights lost to high humidity or clouds. Several of the targets were also observed over 2 nights in January of 2011. Those targets with $V_{rot} \sin i$ measurements have values typically between 1 and 5 km s^{-1}, corresponding to the same bulk delay τ_0 used in the analysis of GJ 699. The only exception is GJ 388, or AD Leo, a particularly active M dwarf, with a rotation of over 12 km s^{-1}. Nominally, I would choose an interferometer delay more appropriate for the higher rotational broadening. However, changing delays requires significant observational overhead, so instead I used the same delay of 4.57 cm for all of the targets. This will result in a performance loss for GJ 388.

Since telluric calibration appears to be the largest source of radial velocity error, I used very bright telluric calibration stars. I performed a SIMBAD search for all stars brighter than V of 5, with $V_{rot} \sin i$ measurements greater than 100 km s^{-1}. High $V_{rot} \sin i$ are needed to broaden the stellar absorption lines such that the only contributors to the complex visibility are the telluric lines. The search turned up roughly 50 stars spread across the sky, and the list was used to find a calibration star nearby to any particular target.

All phase sets were taken in the same mode as the performance verification on GJ 699: Each exposure was 30 seconds long, with a phase set taking 5 minutes of total exposure time, plus an extra minute for overhead. This was done to avoid introducing unexpected effects from longer or shorter exposure times.

7.3   Radial Velocity Measurements

Changes in the radial velocities of the targets were analyzed in the same manner as those of GJ 699. The ΔRV measurements were passed through a sigma-clipping filter, which removed any measurements which deviated from the median measurement by more than 3 times the standard deviation. Figure 7.1 plots the *H* band magnitude of the targets in the TEDI survey versus the RMS of the ΔRV measurements, and the expected RMS based on the σ_F and σ_W fit to the GJ 699 residuals in Figure 5.7, assuming σ_W scales with photon noise. The plot indicates that the white noise in the GJ 699 residuals does not scale simply with photon noise, and includes other components.

7.4   Analysis of Radial Velocities

A standard method for determining the presence of an exoplanet from *RV* data is to construct a Lomb-Scargle periodogram of the measurements (Press & Rybicki, 1989), fit a Keplerian orbit to the peak, and then assess the false-alarm probability of the detection (e.g. Wright & Howard, 2009). Of the 10 stars in the TEDI survey, 8 are being observed as a part of the California Planet Search program, a visible-wavelength radial velocity survey for exoplanets spanning over a decade. The California Planet Search program has detected several exoplanets orbiting M dwarfs, with radial velocity semiamplitudes significantly less than the best attainable precision with TEDI. I do not expect to detect any exoplanets in this data set, and instead intend to rule out the presence of planets. This requires a different approach than the Lomb-Scargle technique, and instead I use a Bayesian approach based on Cumming & Dragomir (2010).
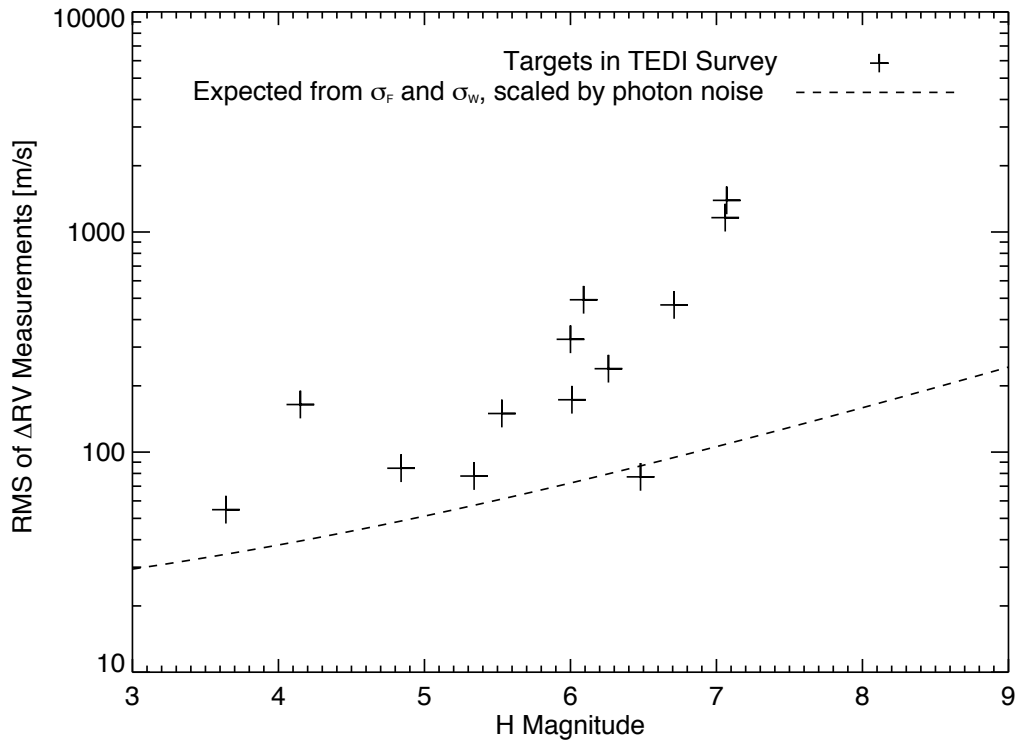
Figure 7.1 – Plot of the RMS of the ΔRV measurements for each star in the TEDI survey versus the *H* band magnitude, including the expected residuals scaling the white noise and noise floor measured in the GJ 699 data. The RMS residuals rise faster than expected from just scaling the white noise component with photon noise. This indicates the presence of addition noise components which are unidentified.

The objective is to rule out planets within a range of masses and orbital distances with 99% certainty, equivalent to 3σ-confidence. I consider only 2 possible models for the ΔRV measurements of a particular star: A single planet orbiting in a circular orbit, and no planet. This is formulated in Bayesian terms as:

$$P(0\,|\,D,\,I) + P(1\,|\,D,\,I) = 1 \qquad (7.1)$$

where 0 indicates no planet, 1 indicates a planet, D is the data, I is the assumptions, and $P(x\,|\,y,\,z)$ is the probability of x given y and z. The probabilities in Equation 7.1 are called *posteriors*. The data is taken over a finite time and with finite precision, and obviously cannot detect or rule out all possible planetary configurations. I consider the posteriors over a specific range of semiamplitude radial velocities and periods:

$$P(0\,|\,D,\,I) + \int_{\Delta Per}\int_{\Delta K} P(Per,\,K\,|\,D,\,I)\,dPer\,dK = 1 \qquad (7.2)$$

where ΔPer is the range of periods, ΔK is the range of semiamplitude radial velocities, $P(Per,\,K\,|\,D,\,I)$ is the probability density function as a function of Per and K. Integrating over a specified ΔPer and ΔK is called *marginalizing*. Period and semiamplitude radial velocity are the relevant quantities, as they relate to the minimum mass and semi-major axis of an orbiting exoplanet. Ruling out the existence of planets within the period and semiamplitude radial velocity phase space, one can convert that to a statement about the presence of planets within a range of masses and orbital distances.

I can rearrange Equation 7.1 to read:

$$P(0|D, I) = \cfrac{1}{1 + \cfrac{\int P(Per, K|D,I)}{P(0|D,I)}} \tag{7.3}$$

This is effectively the same as Equation 9 in Cumming & Dragomir (2010) and corresponds to the *false alarm probability* (FAP) of a detection. If this number is less than 1%, that is a 3σ-confidence detection of an orbiting planet with the ranges ΔPer and ΔK. If this number is greater than 99%, that is a 3σ-confidence non-detection of a planet within the ranges ΔPer and ΔK. The advantage to writing the FAP in this way is that the ratio in the denominator cancels out any common normalization factors. For instance, if the uncertainties associated with the ΔRV measurements are incorrectly estimated by some factor, that factor will cancel in the ratio. The ratio is called the *odds ratio*.

To calculate the posteriors $P(0|D)$ and $P(Per, K|D)$, we use Bayes' theorem (Bayes & Price, 1763; Laplace, 1774; Stigler, 1986):

$$P(M|D, I) = \frac{P(M|I)\, P(D|M)}{P(D|I)} \tag{7.4}$$

where $P(M|I)$ is the *prior*, which weights the posterior based on prior assumptions. For instance, we can be confident that planets do not orbit at distances at or less than the radius of the stellar host. The prior is used to eliminate the likelihood of such a planet. $P(D|I)$ is a normalization factor, which is same for both the planet and no-planet model and cancels out in the calculation of the FAP, so we do not calculate it. $P(D|M)$ is the *likelihood function*, which represents the likelihood of the data given a particular model. For Gaussian errors, the log-likelihood function relates to the more standard $\chi^2(D, M)$ goodness-of-fit statistic:

$$\log \mathrm{P}(D\,|\,M) \propto \left[\sum_i^N \left(\frac{D_i - M_i}{\sigma_i}\right)^2\right]^{N/2} \tag{7.5}$$

where i indexes the data point (D_i) and the model's prediction for that data point (M_i), and σ_i is the uncertainty corresponding to that data point (e.g. Gregory, 2005). For circular orbits, the model is a function of the period Per, the time of the observation t_i, the semiamplitude radial velocity K, orbital phase ϕ, and the offset radial velocity γ:

$$M_i = \gamma + K \sin\left(\frac{2\pi}{P}t_i + \phi\right) \tag{7.6}$$

The orbital phase ϕ and offset radial velocity γ are not relevant to the question of whether planets exist, so they are deemed *nuisance parameters*. To calculate the posterior P(Per, $K\,|\,D$, I) in Equation 7.3, I first calculate the posterior on a grid for all 4 model parameters P(Per, K, ϕ, γ, $|\,D$, I), and then integrate (or marginalize) that over the nuisance parameters γ and ϕ. I assume a Jeffreys prior for Per and K, which evenly weights decadal increments (Jeffreys, 1945), and a uniform prior for γ and ϕ. The model for no planet has one parameter, the offset radial velocity: $M_i = \gamma$. Marginalizing over γ in both the planet and no planet posteriors can be done analytically. After marginalizing over γ, the posterior for no planet, P($0\,|\,D$, I), is a scaler and is independent of K or Per. Combining Equations 7.6 and 7.5, and plugging that into Equation 7.3, we can calculate the FAP for a specified range of periods and semiamplitude radial velocities.

To calculate the FAP, I create a grid of Per, K and ϕ, since these variables cannot be marginalized analytically. The Per array is chosen to go from 10 hours

to the maximum time space of the observations of a given target. The spacing in the *Per* array is chosen so that with each increment of the period, the phase of does not change by more than 1/20th of a cycle across the entire time span of the observations. This can be expressed analytically as:

$$\Delta Per\ N_{\text{cycles}} = \frac{Per}{20} \tag{7.7}$$

where the number of cycles is the time span of the observations divided by the period, or Per_{max}/Per. This can be rewritten as first-order ordinary differential equation, where x is the index of the *Per* array:

$$\frac{dPer}{dx} = \frac{Per^2}{20\,Per_{max}} \tag{7.8}$$

Solving this equation for *Per(x)*, including a boundary condition for the minimum desired period Per_{min} yields the *Per* array:

$$Per(x) = \left(\frac{1}{Per_{min}} - \frac{x}{20Per_{max}} \right)^{-1} \tag{7.9}$$

This results in 200 to 1500 elements in the *Per* array, depending on the target. The *K* array is chosen to scale logarithmically from 10 m s^{-1} to 1000 m s^{-1} with 100 elements. The ϕ array is linear from 0 to 360 degrees with increments of 5 degrees, resulting in 72 elements. Increasing the resolution of the *K* and ϕ was not found to dramatically effect the results of the analysis.

To determine the region of *Per* and *K* phase space where I can rule out the presence of planets with 99% certainty, I first marginalize over γ and ϕ, then sort

the posterior grid in order of increasing probability, then perform a cumulative sum on the sorted posterior, calculating the FAP for each element. I then take all of the points in the cumulative sum with FAP of 99% and higher, and find their positions on the *Per* and *K* grid. This leaves a contour in *Per* and *K* phase space where I can rule out the presence of planets.

Figures 7.5 through 7.5 plot the ΔRV measurements, the corresponding Lomb-Scargle periodogram, the odds ratio after marginalizing over *K*: P(*Per*|*D*, *I*)/P(0|*D*, *I*), the odds ratio after marginalizing over *Per*: P(*K*|*D*, *I*)/P(0|*D*, *I*), the *Per* and *K* contour with an FAP > 99%, and the *a* and $M_P \sin i$ contour with an FAP > 99%, all for a simulated planet, simulated noise, and the targets in the TEDI survey. The Lomb-Scargle periodogram was calculated using a routine available as part of the *rvlin* package for fitting Keplerian curves to radial velocity measurements (Wright & Howard, 2009), and includes an estimation of the FAP of the peak, which I call the LSFAP so as not to confuse it with the Bayesian FAP in Equation 7.3.

The Lomb-Scargle periodograms are consistent with the odds ratio plots vs *Per*. This is expected since the Lomb-Scargle periodogram measures the power at different periods, and the odds ratio vs *Per* measures the probability density of various planet models with different period orbits. The main difference between the two is the scaling, and a downward trend with increasing *Per* in the odds ratio. This is because the odds ratio includes the influence of the Jeffreys prior. The odds ratio after marginalizing over *Per* compares the likelihoods of a models with different values for *K*. The curves tend downward for larger *K*, which is expected because larger *K* values are more easily detected, and therefor more easily ruled out if undetected. The final plots indicate the phase space

where the FAP > 99%. Unsurprisingly, this corresponds to regions with high K and high $M_P \sin i$. To calculate $M_P \sin i$, I assumed a mass based on the published spectral type of the object, scaling the calibrated physical parameters of MK spectra types available in Allen's Astrophysical Quantities (Cox, 2004).

Included on the final plot is the FAP calculated by marginalizing P(Per, $K | D$, I) over all Per and K considered. For the simulated planet in Figure 7.5, this value is roughly in agreement with the LSFAP of the peak in the Lomb-Scargle periodogram, both less than 1 %, indicating a detection. For simulated noise and no planet in Figure 7.5, the LSFAP and FAP are slightly different estimators. The LSFAP estimates the probability that the peak in the Lomb-Scargle periodogram is due to noise, whereas the FAP estimates the probability that the data represents the no-planet model.

7.5   Discussion

None of the targets have an FAP < 1%, which would indicate the presence of a planet in a circular orbit. As indicated in Figure 7.1, the ΔRV precision achieved for each exposure is dramatically different between targets, because of the spread in brightnesses. It is difficult to make a statistical statement about the presence of gas-giant planets orbiting these metal-rich targets. I can, however, rule out the presence of short-period planets upwards of 1 Jupiter-mass around GJ 411, GJ 388 and GJ 406. Although GJ 411 is in the Endl et al. (2003) survey, they did not have cadences to detect short period planets. The results are not surprising given the attention bright M dwarfs have received from visible-wavelength radial velocity surveys. The other targets in the survey are simply

too faint to make a similar statement about, although none appear to have a 10 Jupiter-mass or larger companion in a short period orbit.
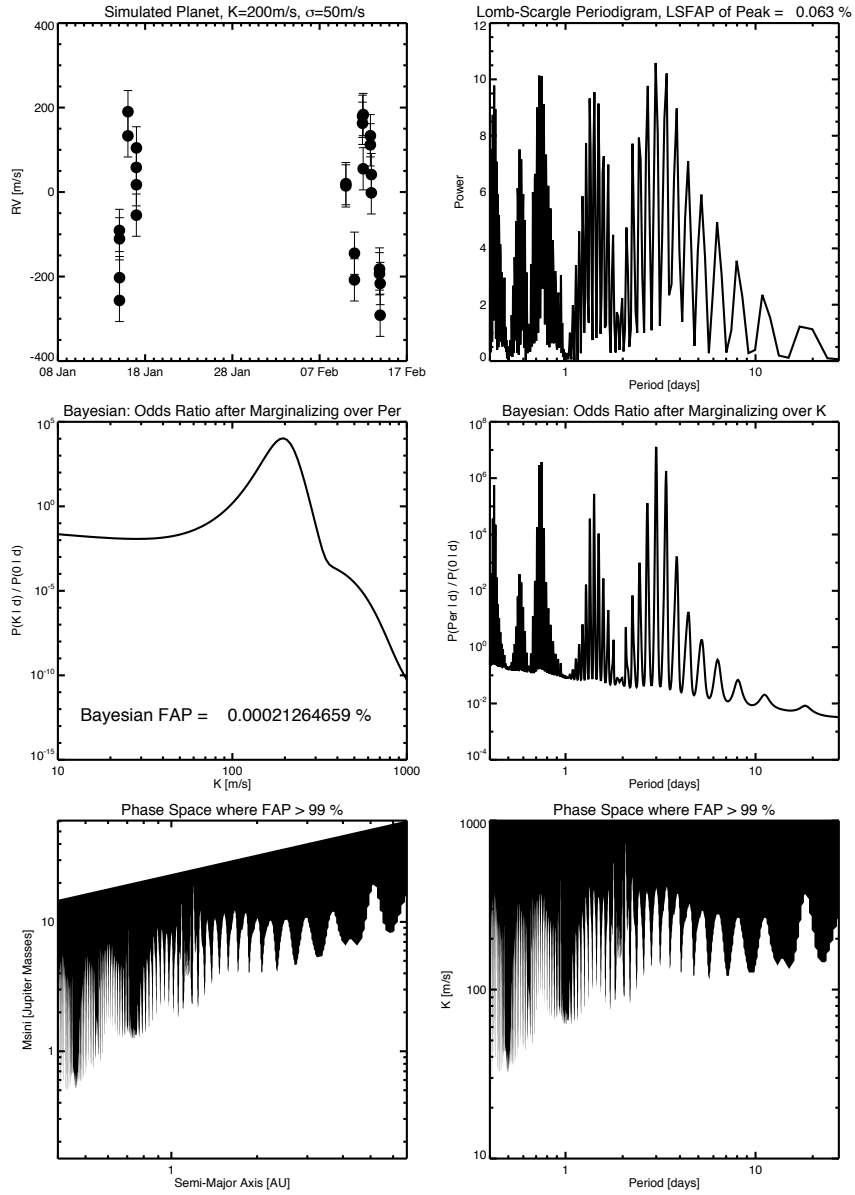
Figure 7.2 – Analysis of ΔRV measurements for a simulated exoplanet host (K = 200 m s^{-1}, *Per* = 3 days, σ_i = 80 m s^{-1}). *Top left*: ΔRV measurements vs. UT time. *Top right*: Lomb-Scargle periodogram of the ΔRV measurements, showing a peak at 3 days with an LSFAP of < 1 %. *Middle left*: The odds ratio after marginalizing over *Per*, showing the presence of a planet with K = 200 m s^{-1}. The fully marginalized odds parameter also yields an FAP of < 1 % by Equation 7.3. *Middle right*: The odds ratio after marginalizing over *K*, showing similar structure to the Lomb-Scargle periodogram. *Bottom left*: Contour in $M_P sini(i)$ vs. Semi-major axis *a* with FAP > 99 %, indicating the regions where planets in circular orbits can be ruled out with high confidence. *Bottom right*: Same, but for *K* vs. *Per*.
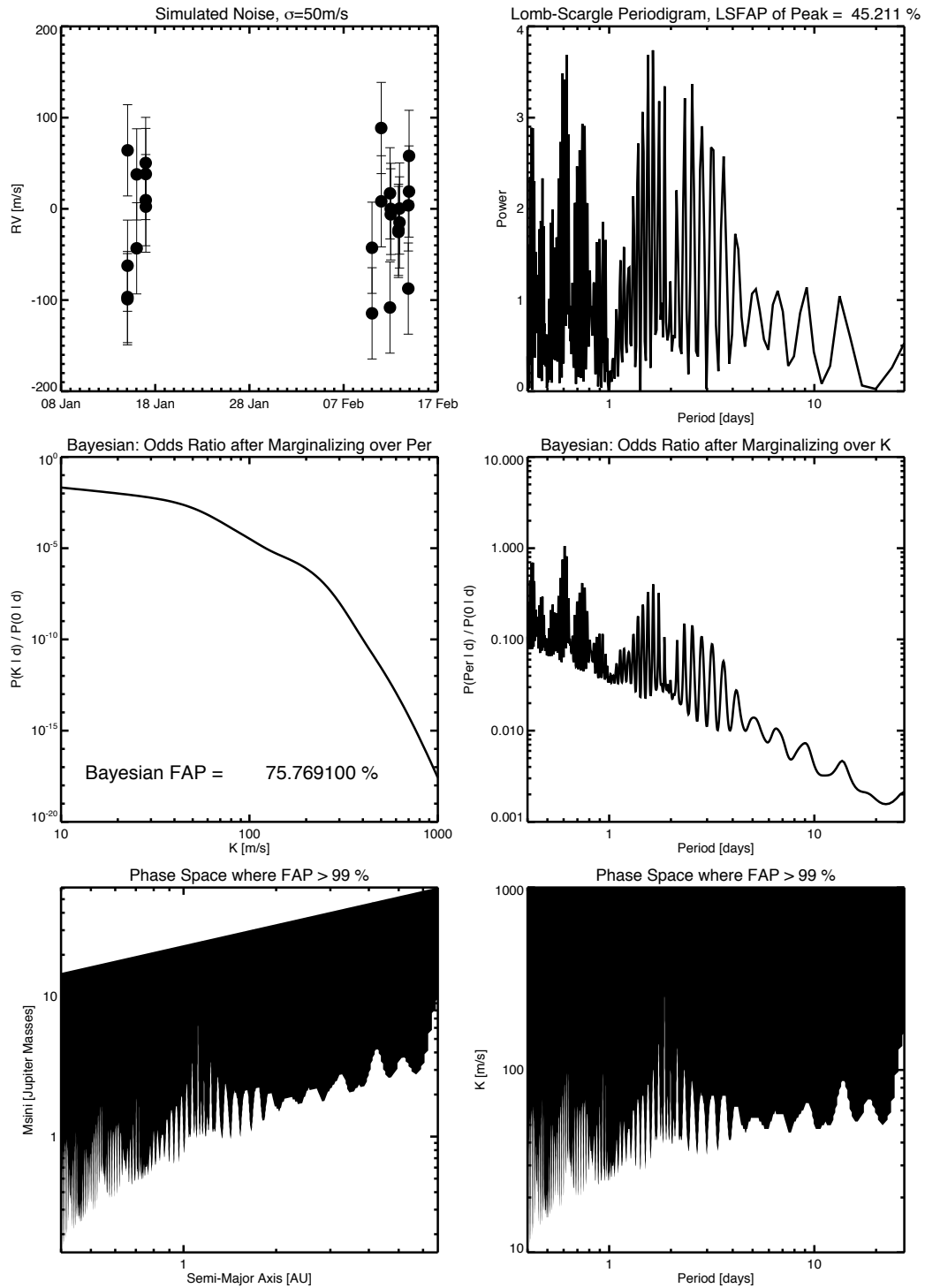
Figure 7.3 – Analysis of ΔRV measurements for simulated noise (no planet) with $\sigma_i = 80$ m s^{-1}. See Figure 7.5 for an explanation of the panels. The FAP after marginalization is 97.25%, not high enough to rule out a planet within the considered K and *Per* phase space. However, if we reduce the phase space, we can rule out planets with high K.
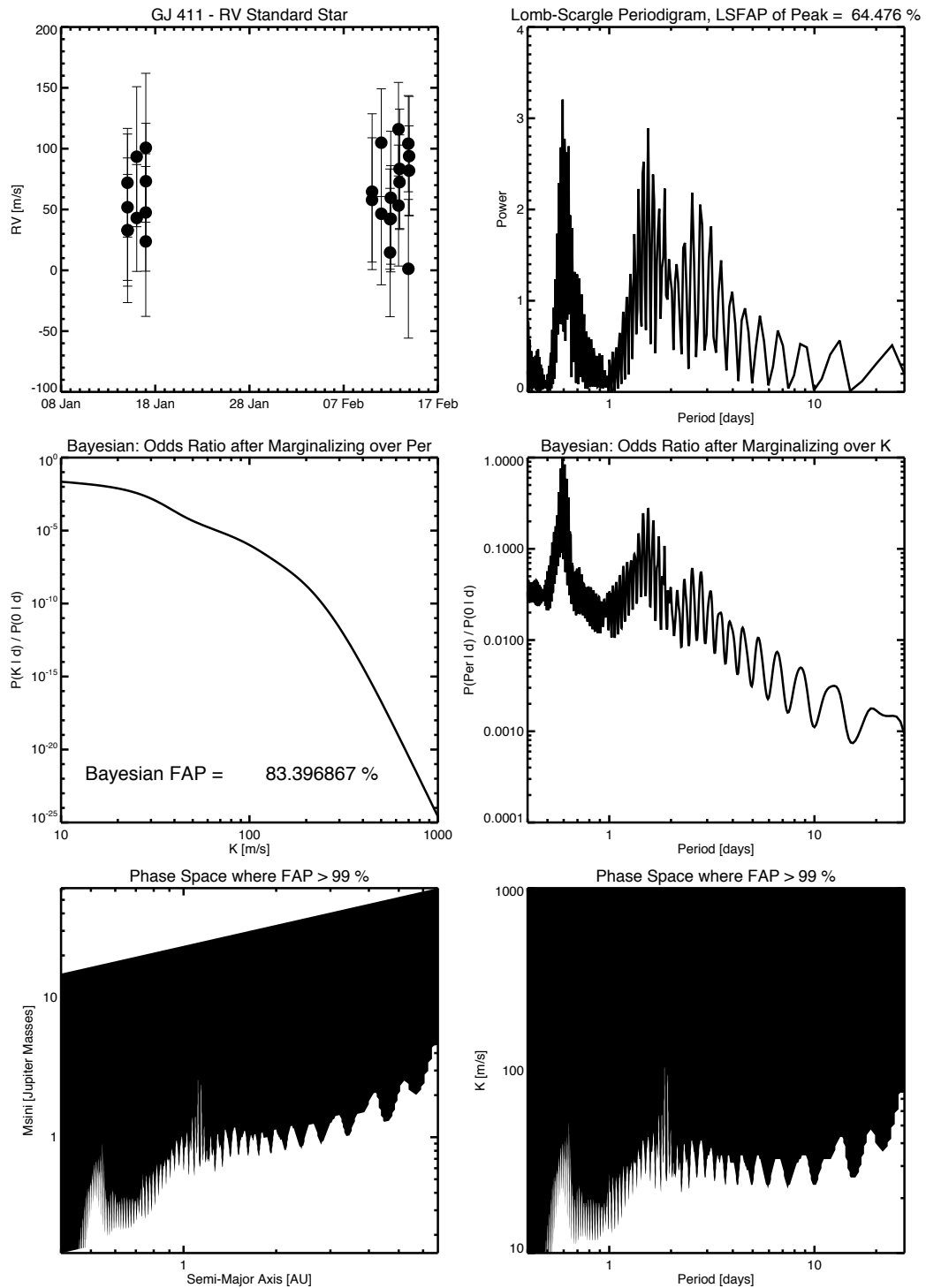
Figure 7.4 – Analysis of ∆RV measurements for GJ 411, a radial velocity standard. See Figure 7.5 for an explanation of the panels.
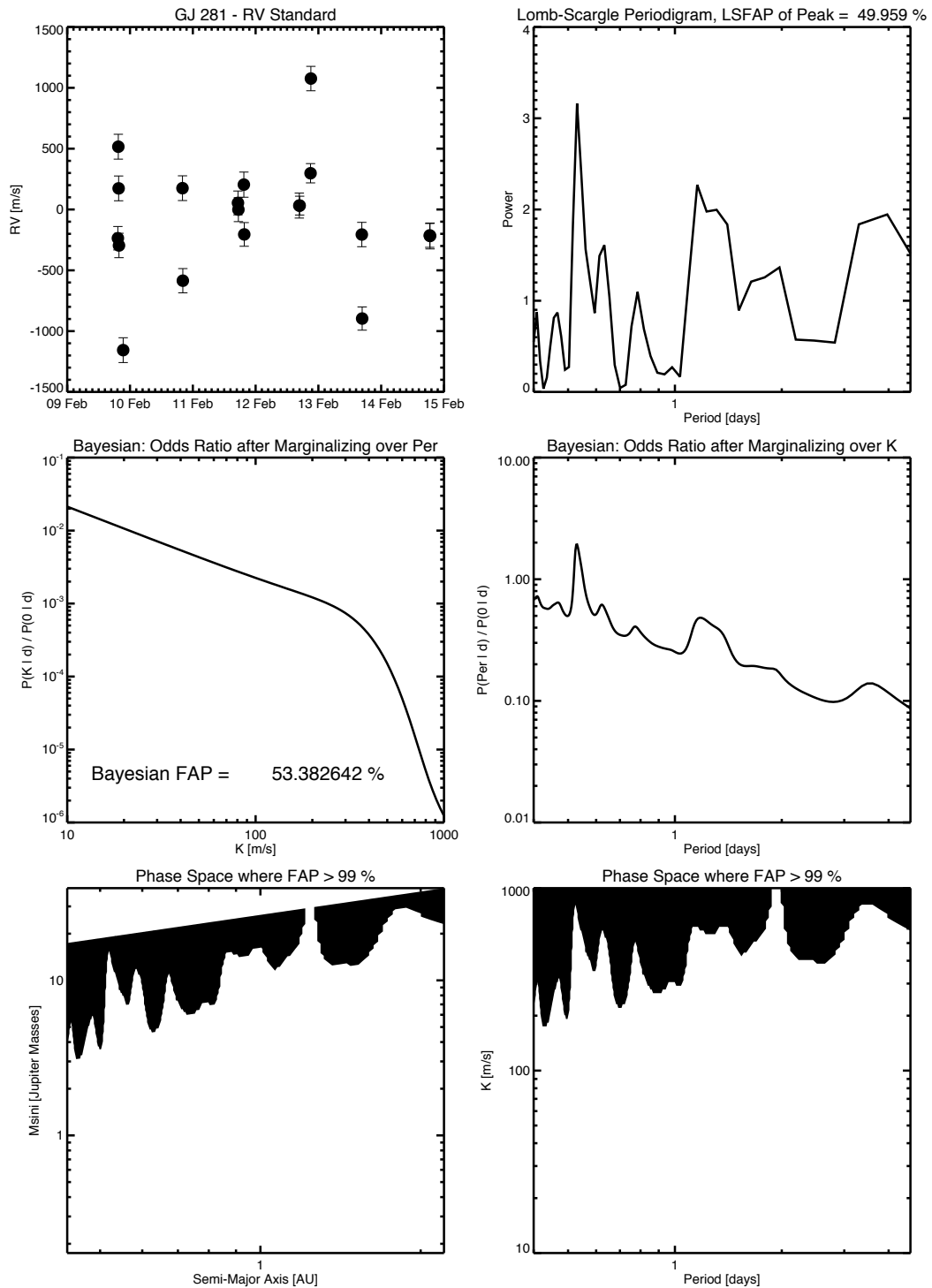
Figure 7.5 – Analysis of ΔRV measurements for GJ 281, a radial velocity standard. See Figure 7.5 for an explanation of the panels.
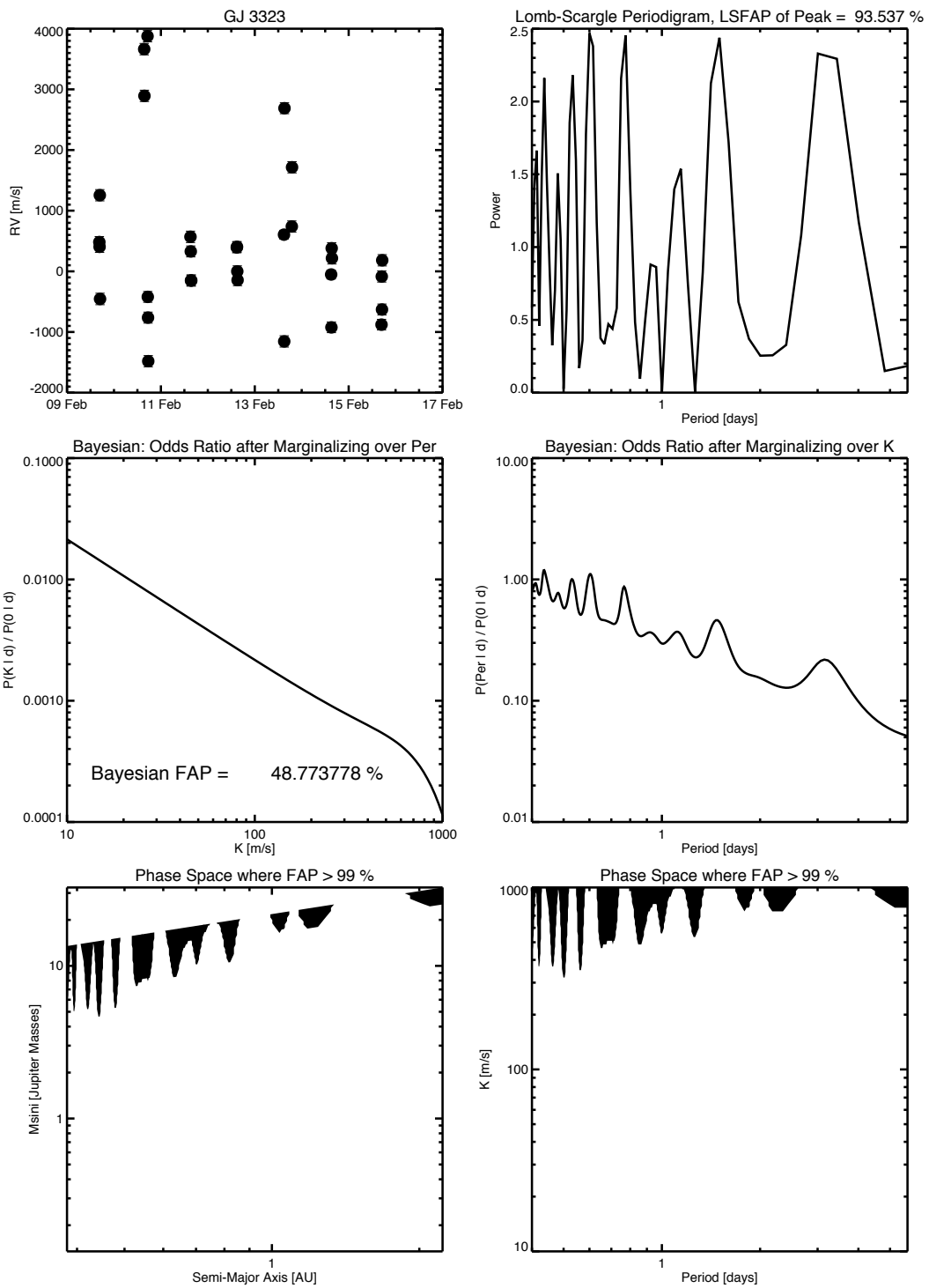
Figure 7.6 – Analysis of ΔRV measurements for GJ 3323. See Figure 7.5 for an explanation of the panels.
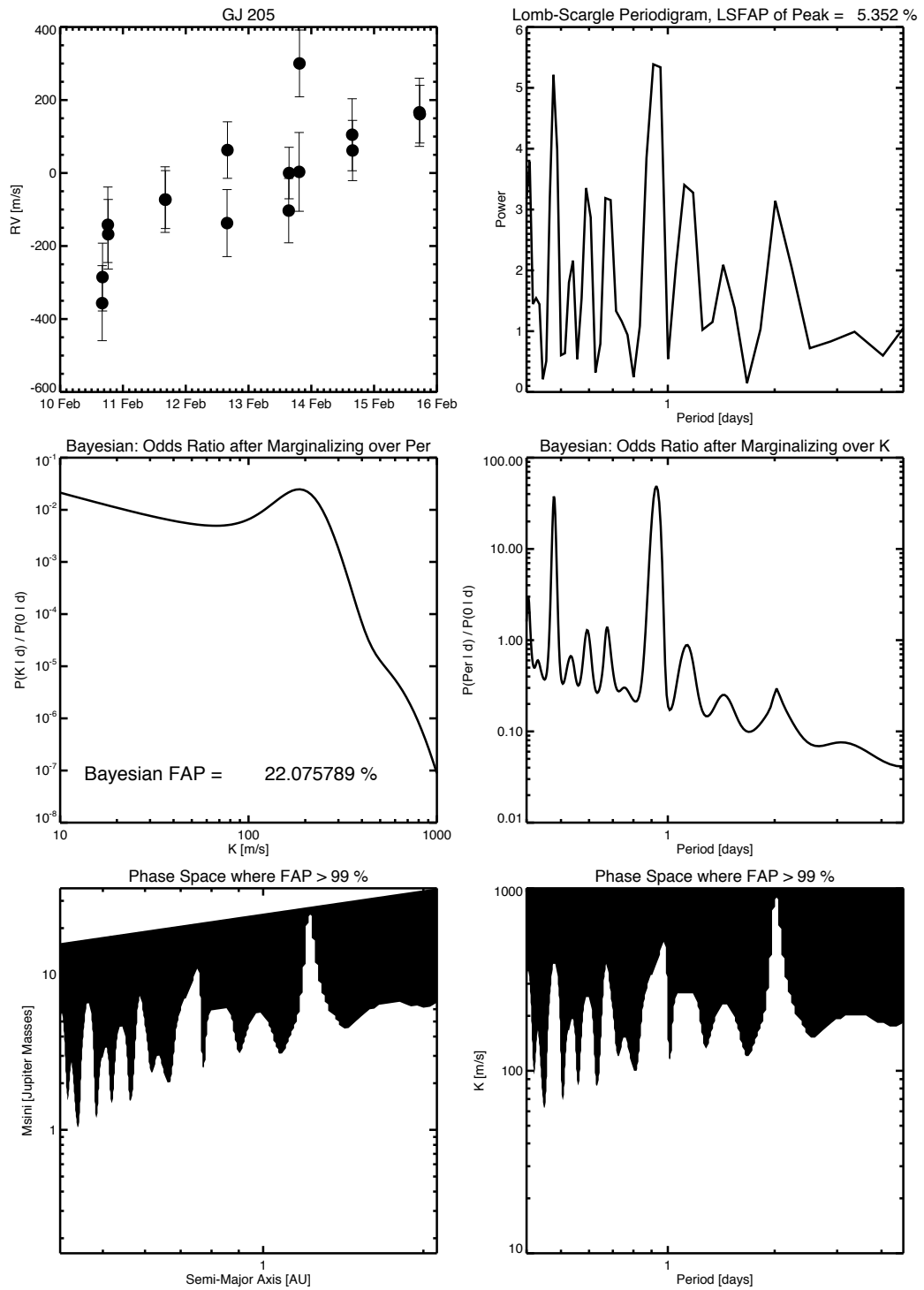
Figure 7.7 – Analysis of ΔRV measurements for GJ 205. See Figure 7.5 for an explanation of the panels.
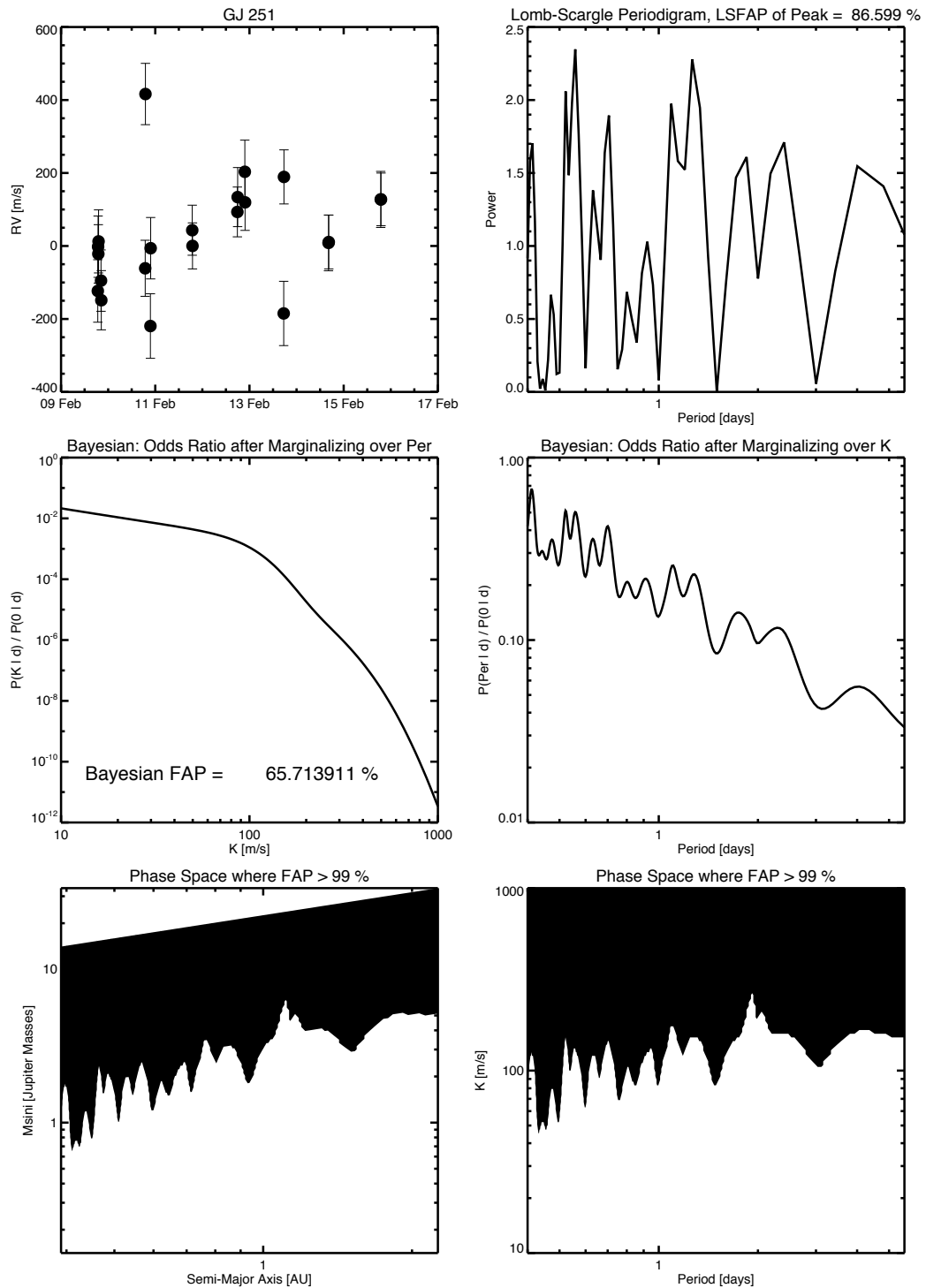
Figure 7.8 – Analysis of ΔRV measurements for GJ 251. See Figure 7.5 for an explanation of the panels.
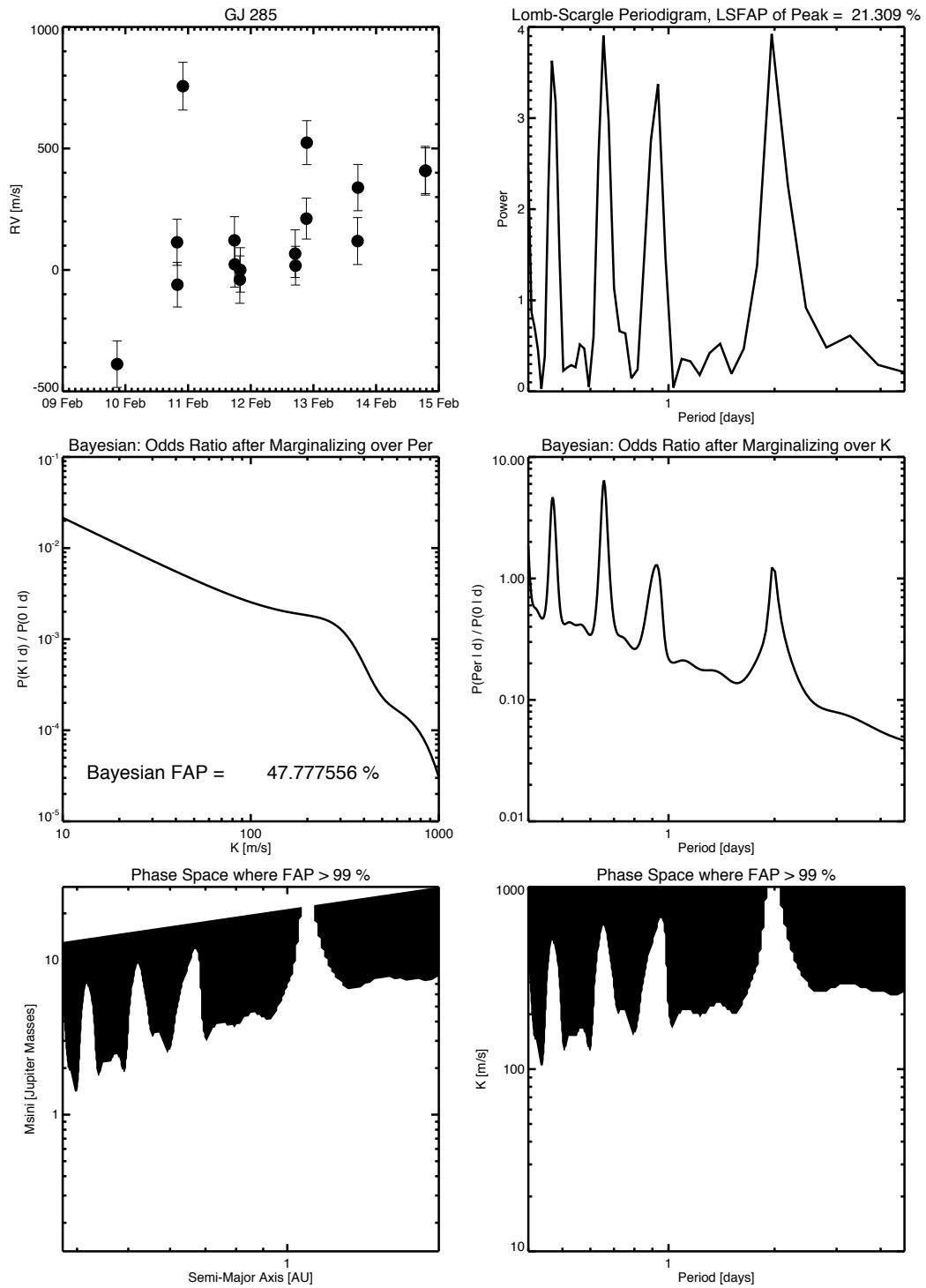
Figure 7.9 – Analysis of ΔRV measurements for GJ 285. See Figure 7.5 for an explanation of the panels.
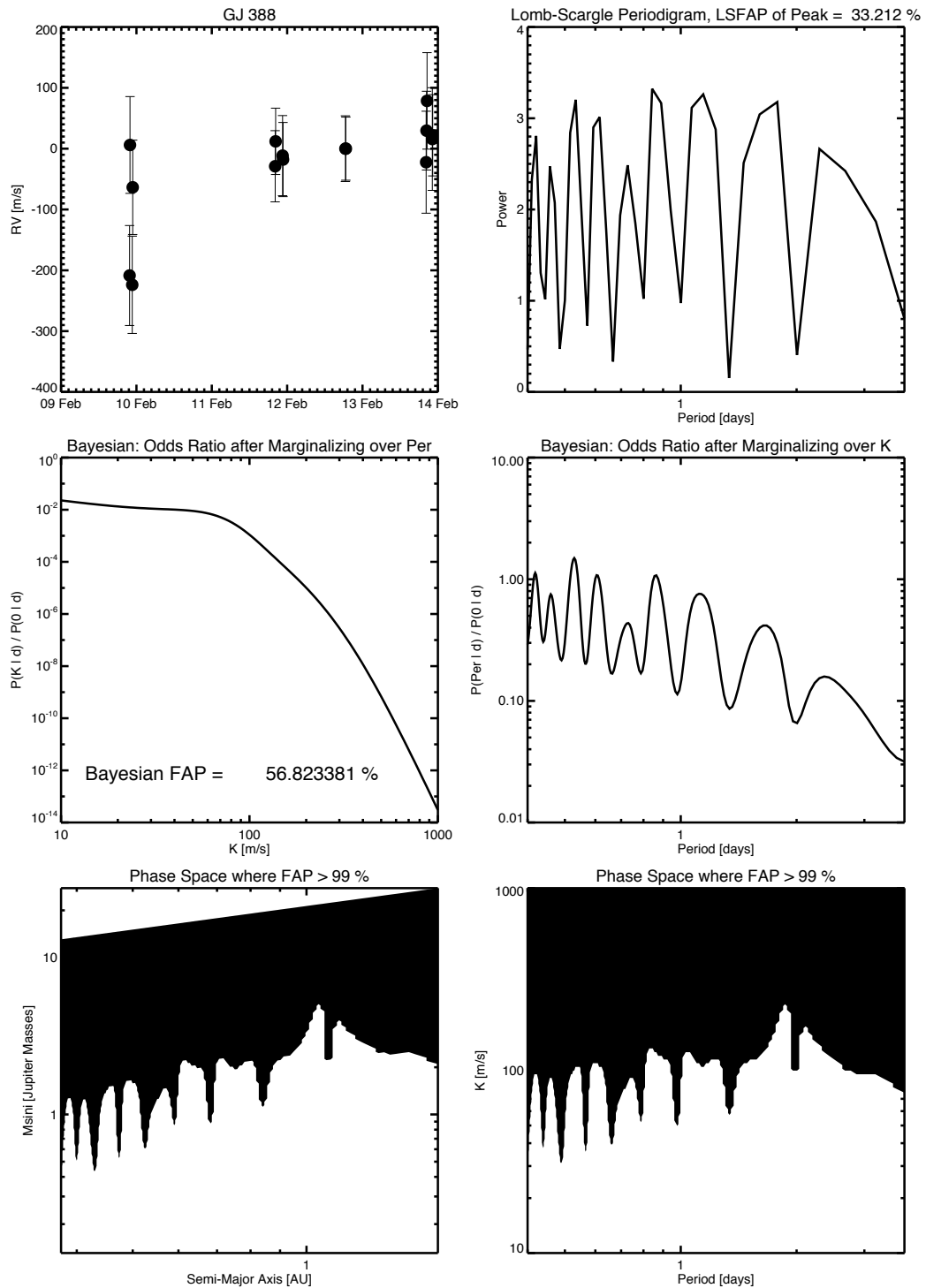
Figure 7.10 – Analysis of ΔRV measurements for GJ 388. See Figure 7.5 for an explanation of the panels.
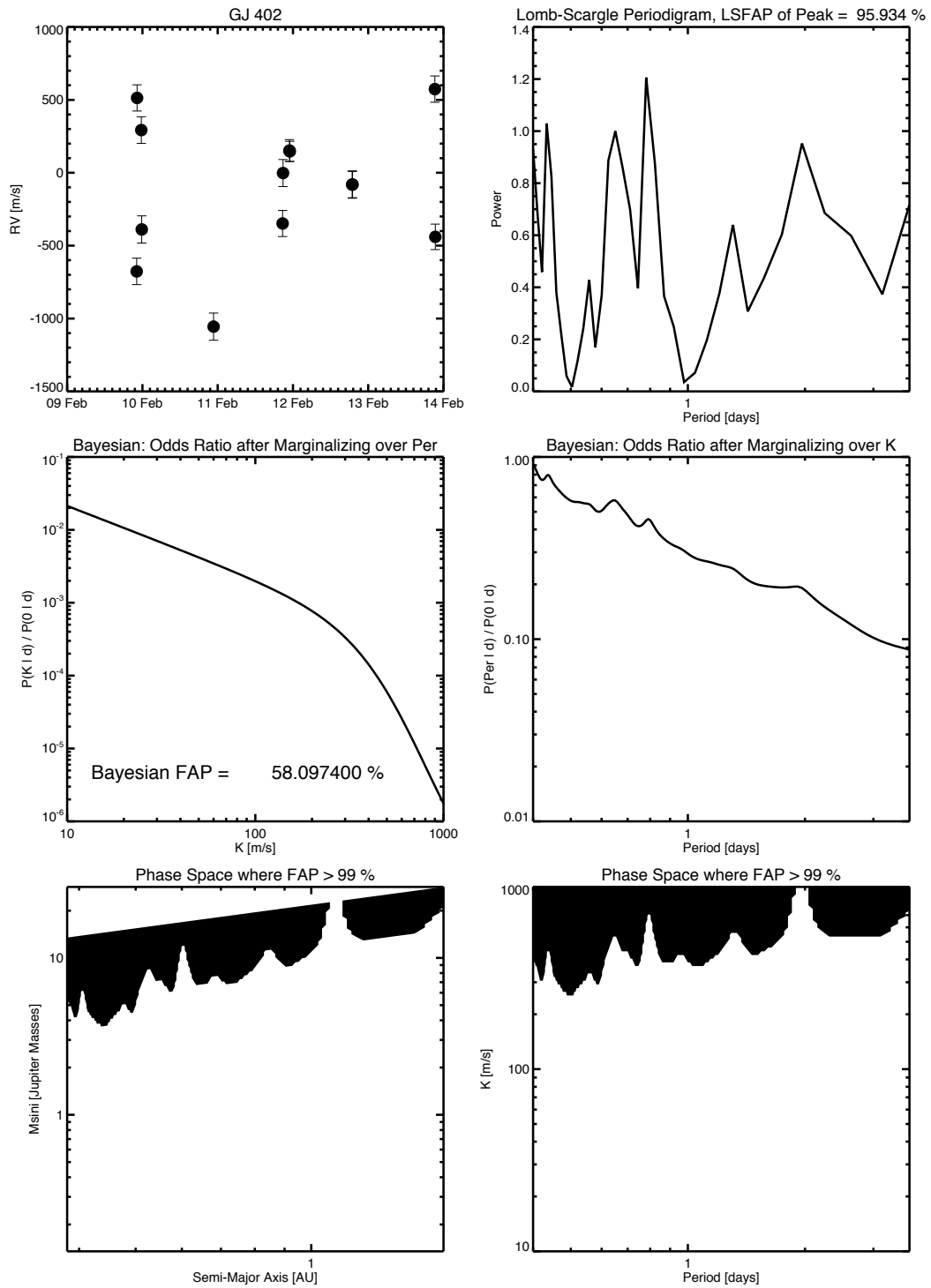
Figure 7.11 – Analysis of ΔRV measurements for GJ 402. See Figure 7.5 for an explanation of the panels.
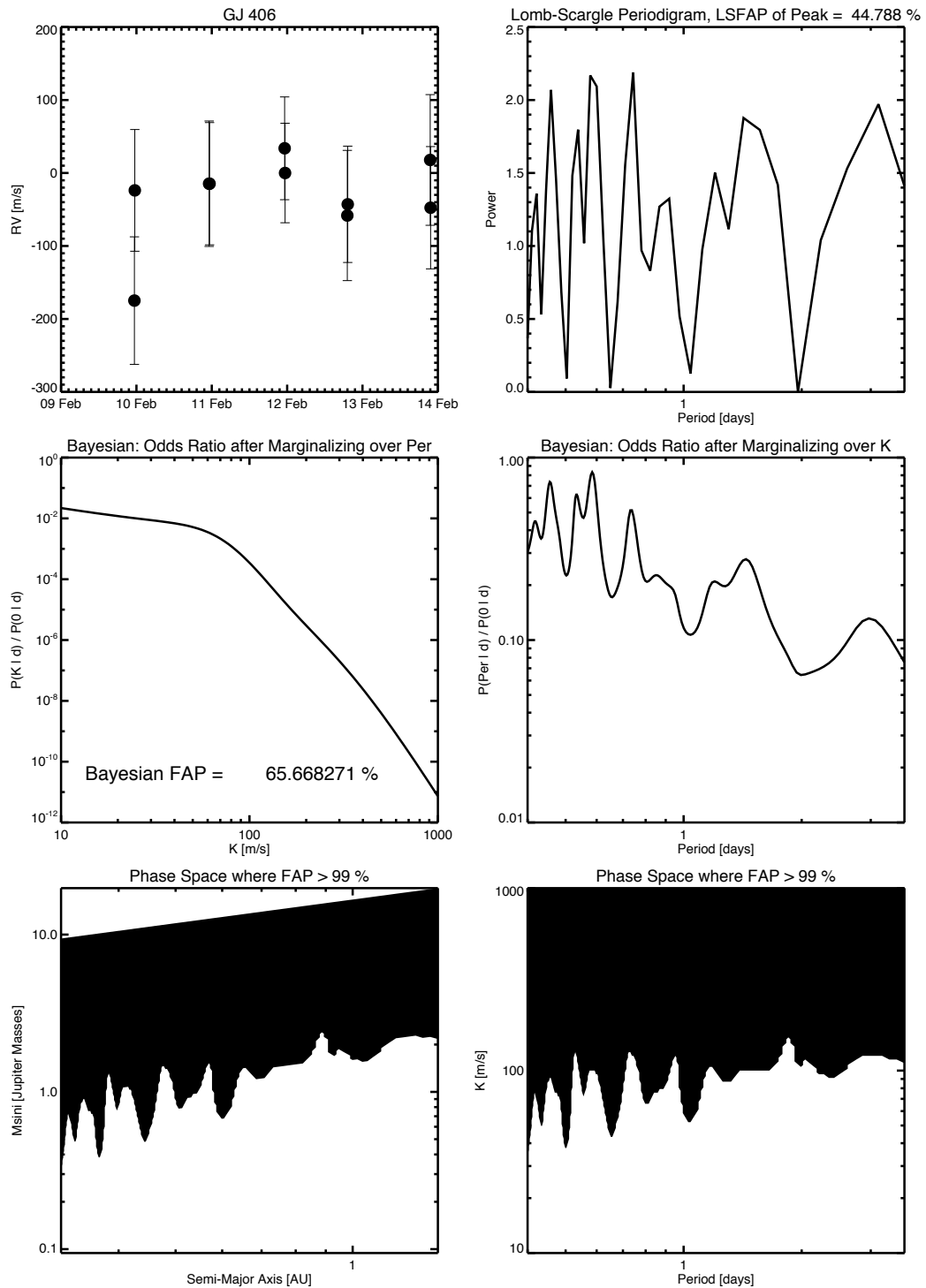
Figure 7.12 – Analysis of ΔRV measurements for GJ 406. See Figure 7.5 for an explanation of the panels.
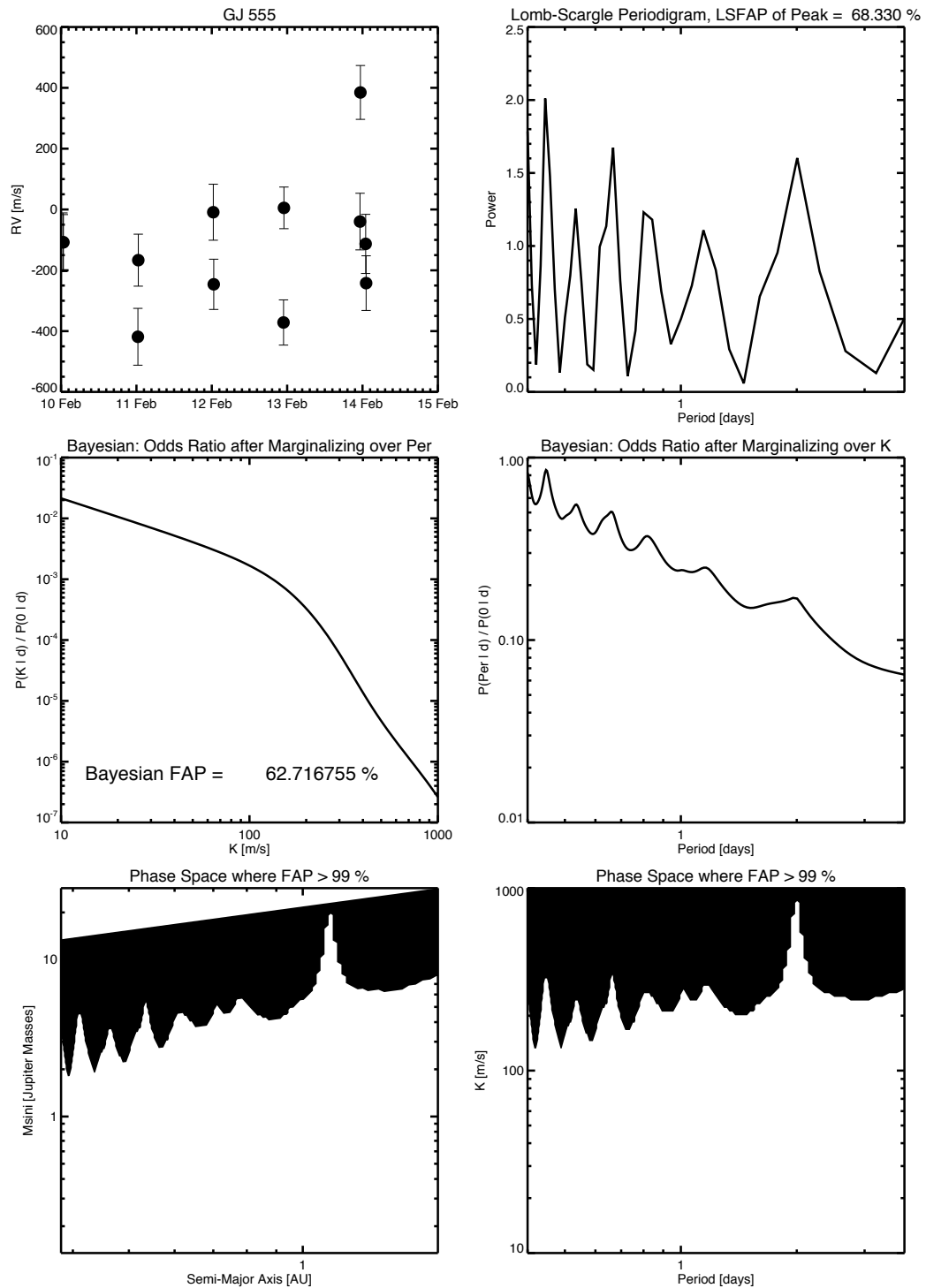
Figure 7.13 – Analysis of ΔRV measurements for GJ 555. See Figure 7.5 for an explanation of the panels.
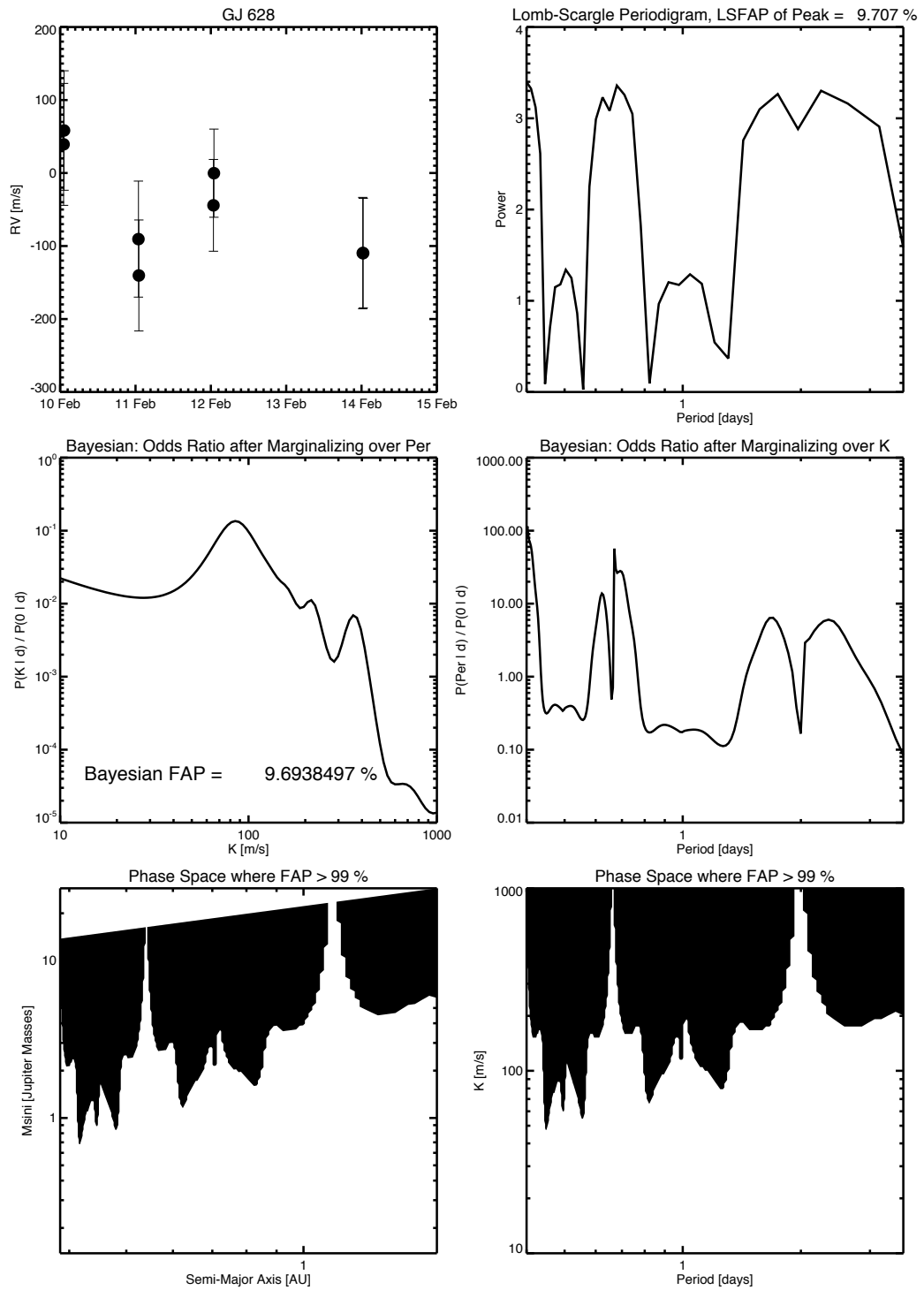
Figure 7.14 – Analysis of ΔRV measurements for GJ 628. See Figure 7.5 for an explanation of the panels.
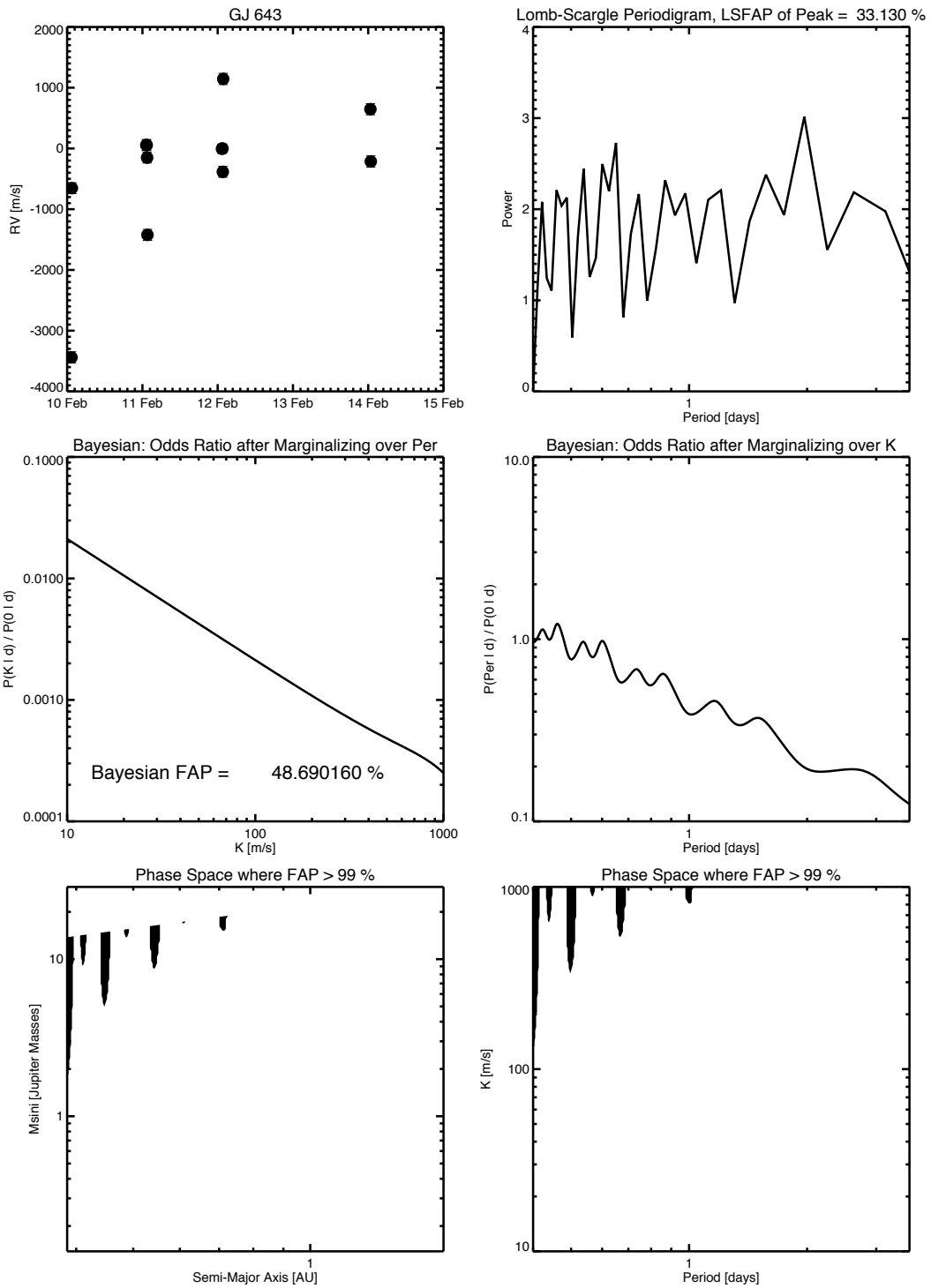
Figure 7.15 – Analysis of ΔRV measurements for GJ 643. See Figure 7.5 for an explanation of the panels.

CHAPTER 8

CONCLUDING REMARKS

I have demonstrated that the combination of a variable delay interferometer and a resolution 2700 near-infrared spectrograph can achieve better than 37 m s^{-1} of precision with 5 minutes of total integration time per observation on a nearby M dwarf, and that the largest source of error is insufficient calibration of telluric lines. I have used this performance to undertake a survey for short-period, gas-giant exoplanets orbiting nearby metal-rich M dwarfs, and ruled out the presence of Jupiter-mass planets orbiting within 1 AU of a few of the targets.

At the current performance level, TEDI is not strongly competitive with current visible-wavelength Doppler surveys of M dwarfs, and cannot detect terrestrial exoplanets. Nevertheless, the demonstration of better than 40 m s^{-1} of precision represents an important milestone in the effort to achieve precise radial velocities at infrared wavelengths, especially considering that the spectrograph involved has a resolution of only 2700.

Though unsuccessful at detecting exoplanets, the results of the TEDI experiment strongly influence future exoplanet instrumentation. Telluric lines clearly play a significant role in measuring precise radial velocities in the near-infrared. In order to develop successful near-infrared radial velocity programs capable of detection and mass measurement of terrestrial exoplanets orbiting M dwarfs, the effects of telluric interference must be accommodated. The results of the TEDI program motivate future near-infrared radial velocity programs in three directions: (1) toward modeling spectral data products with accurate high resolution stellar and telluric spectral models, including the effects of mixing and

aliasing, (2) toward high-resolution spectrographs capable of resolving stellar and telluric lines enough to reduce or eliminate the effects of mixing and aliasing, and (3) toward limiting radial velocity measurements to spectral regions devoid or nearly-devoid of telluric lines.

8.1 Forward Modeling

Forward modeling the spectral data product requires accurate high-resolution stellar and telluric models. Late-type photospheres have complicated near-infrared spectra, being dominated by *line opacity* rather than *continuum opacity*. Unlike Sun-like stars, near-infrared late-type stellar spectra show no obvious continuum with superimposed absorptions lines. Rather, the opacity at any given near-infrared wavelength is a combination of the opacities of various molecules, which depend on the temperature, pressure, density, convection and relative abundances in the star, many of which change significantly with depth into the photosphere. Modeling late-type spectra requires assumptions about local thermal equilibrium, and mixing length theory. As such, it has been difficult to reproduce the observed late-type near-infrared spectra with models at *low* resolution, much less high resolution, due to their complex photospheres (Pavlenko et al., 2006).

Modeling the Earth's atmosphere is also challenging. Unlike stellar absorption lines, telluric transmission lines are not broadened by rotation or pressure and are extremely narrow. Many of them are saturated. More importantly, the true telluric transmission spectrum is constantly changing throughout the night, as the airmass of a target and atmospheric humidity change. Accurately modeling the high resolution features of the Earth's transmission spectrum would

require simultaneous weather monitoring.

8.2   High Resolution Spectroscopy

Building spectrographs with very high resolution and sufficient bandwidth is itself challenging. Consider CRIRES, a high-resolution infrared spectrograph on the 8.1 m VLT telescope (Kaeufl et al., 2004). As explained in Chapter 1, CRIRES achieves a resolution of 10^5, but with limited simultaneous bandwidth: only 80 nm in K band. This limits the efficiency of the instrument for exoplanet surveys, to the extent that HARPS is more efficient for mid-M dwarfs, despite being deployed on a 3.5 m telescope. Although, even with CRIRES, Bean et al. (2010) found a 5 m s^{-1} noise floor which they attributed to telluric interference. The noise floor is less than TEDI, but to detect terrestrial exoplanets, 1 m s^{-1} of ΔRV precision is required.

8.3   Telluric Free Regions: Y Band

The third approach appears to be the most promising: avoid the telluric regions altogether. A relatively ignored spectral region is Y band, or roughly 1.0 to 1.1 μm (Hillenbrand et al., 2002). Figure 6.1 in Chapter 6 plots a model stellar spectrum and a model telluric spectrum. Figure 8.1 is the same, but specifically for the region near the CO band, used by Blake et al. (2010), Bean et al. (2010) and Crockett et al. (2011) for precise radial velocimetry, and Y band.

Y-band is an exciting region to develop high-precision near-infrared radial
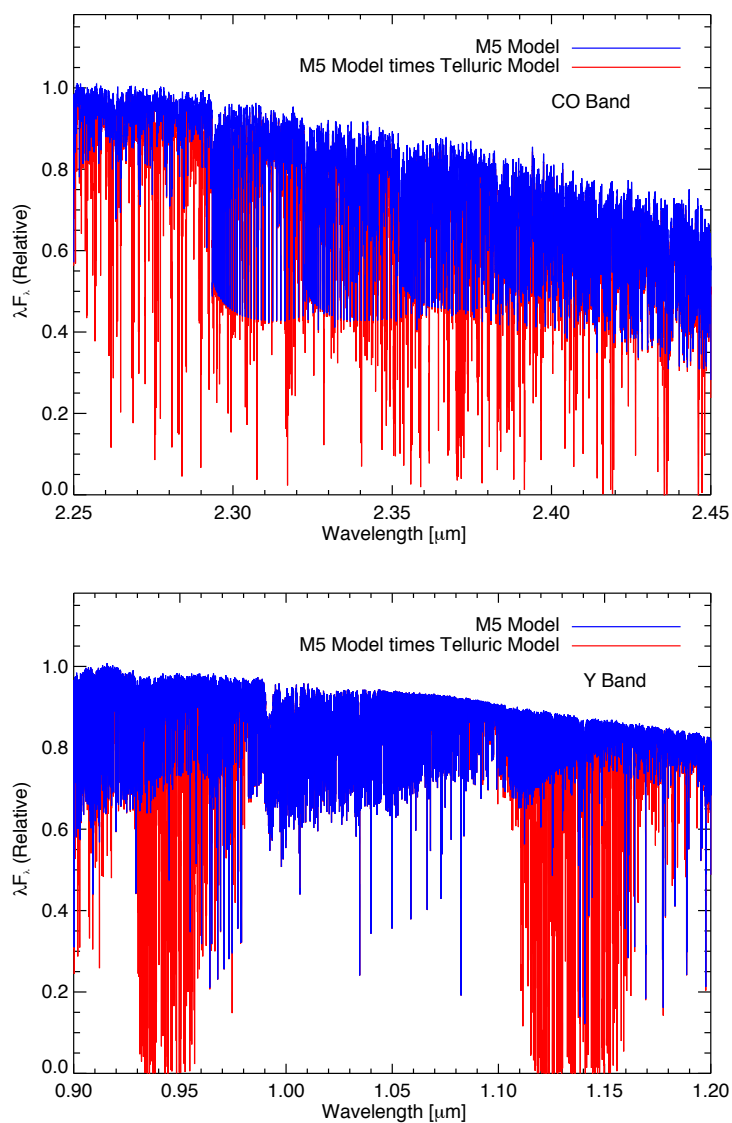
Figure 8.1 – High resolution model spectra for the CO band and Y band. *Top*: Model M5 spectrum with and without telluric lines for the CO band. Blake et al. (2010), Bean et al. (2010) and Crockett et al. (2011) use this spectral region for precise radial velocities because of the narrow stellar absorption lines from the CO band head, which begin at 2.29 μm. *Bottom*: Same, but for Y band, which has little telluric contamination from 1.0 to 1.1 μm.

velocimetry. Only 100 nm wide, it still suffers from limited bandwidth, but Y band contains significantly more flux than K band for mid-M dwarfs without the added thermal background noise. TEDI does not utilize Y band because of reduced throughput towards shorter wavelengths (Figure 4.2 in Chapter 4) and because TEDI requires large bandwidth to achieve high radial velocity precision. However, a well-calibrated, high-resolution spectrograph optimized for Y band could could efficiently achieve m s^{-1} of ΔRV precision, and detect or characterize terrestrial-mass planets orbiting M dwarfs.

To investigate the feasibility of Y band for radial velocity performance on M dwarfs, I performed identical simulations to those in Chapter 6, but instead of a resolution 2700 spectrograph, I simulated a resolution 50000 spectrograph. A resolution 50000 spectrograph with an interferometer would sample significantly more Fourier space than TEDI, and provide more adequate calibration of telluric lines. Figures 8.2 plots the Fourier transform of the late-type stellar model used in the simulations and its expected Doppler content, the Fourier transform of the telluric transmission model and the windows of TEDI and a theoretical R=50000 spectrograph with an interferometer, for both the CO band (2.3 to 2.4 mm) and Y band (1.0 to 1.1 μm). A theoretical R=50000 spectrograph captures most of the Doppler content for both cases, but the telluric lines have significantly more power in the CO band.

Figure 8.3 plots simulated radial velocity residuals for the same barycentric motions as the data on GJ 699 from Chapter 5, and the TEDI simulations in Chapter 6, but with a resolution 50000 spectrograph, and a delay of 4.6 cm for the CO band simulation, and a delay of 2.6 cm for the Y band simulation. I have scaled the signal-to-noise of the individual spectra to match the equivalent
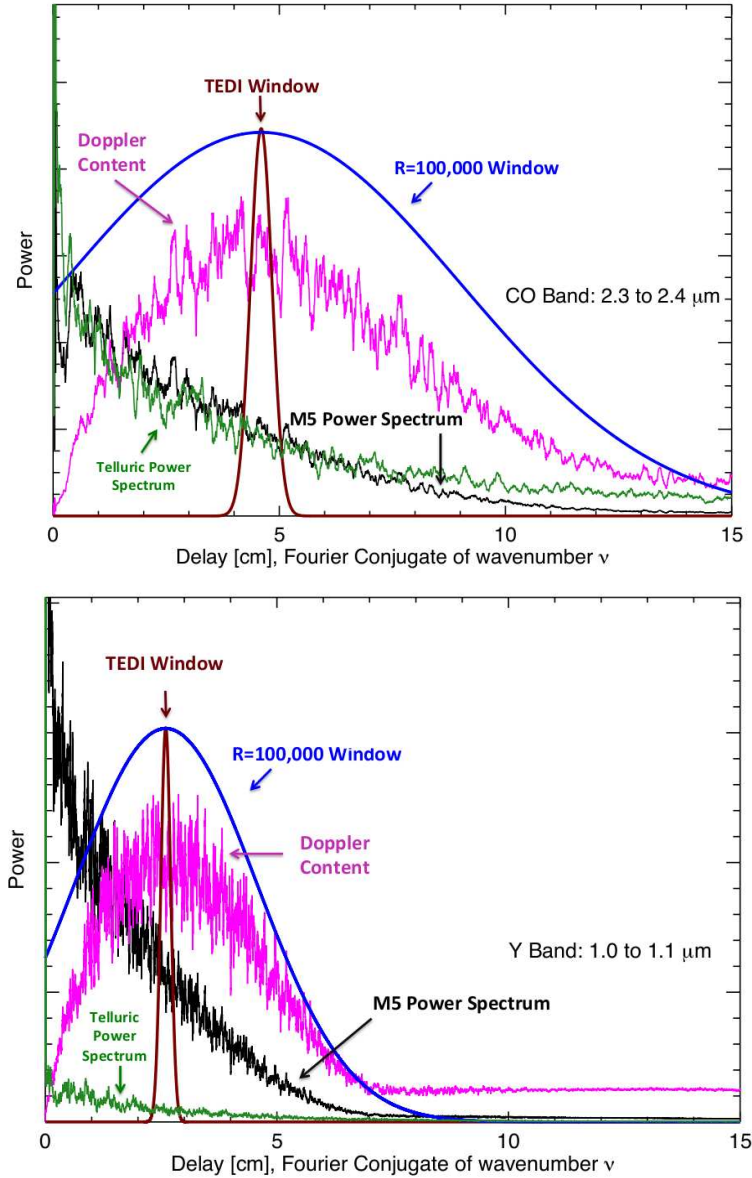
Figure 8.2 – Fourier transform of the late-type stellar model and its expected Doppler content, the Fourier transform of the telluric transmission model and the windows of TEDI and a theoretical R=50000 interferometer-spectrograph combination. *Top*: Fourier space for the CO band: 2.3 to 2.4 μm. The instrument windows correspond to an interferometer delay of 4.6 cm. *Bottom*: Fourier space for Y band: 1.0 to 1.1 μm. The instrument windows correspond to an interferometer delay of 2.6 cm. A theoretical R=50000 spectrograph captures most of the Doppler content for both cases, but telluric lines play are much larger role for the CO band.

throughput of TEDI, but without any wavelength dependence: 1.5% through-put for both bands. TEDI suffers from significantly lower throughput in both the Y and CO bands (Figure 4.2 in Chapter 4), but for theoretical spectrographs it is safe to assume they would be throughput optimized for their respective bands. Unlike the simulated TEDI residuals, both the CO band and the Y band simulations show RMS residuals roughly consistent with photon noise. At higher resolution, the mixing of the telluric lines is reduced, and 10 m s^{-1} of precision is achieved on a star like GJ 699.

To investigate the fundamental limitation to these theoretical instruments, I also simulated the residuals without photon noise. Figure 8.4 plots the residuals without any noise added to the measurements. The effect of telluric interference is significantly stronger in the CO band than in the Y band. The RMS of the CO band residuals is strikingly similar to the performance achieved by Bean et al. (2010) of 5 m s^{-1} using the same band. The Y band residuals, however, show a significantly smaller RMS performance of less than 1 m s^{-1}.

A theoretical R=50000 spectrograph with an interferometer operating in Y band, with the same throughput as TEDI, could achieve roughly 10 m s^{-1} of RMS performance in 5 minutes of integration on GJ 699, with a 1 m s^{-1} noise floor. Scaling this performance to 40 minute exposures on GJ 1214, a factor of 60 fainter, the theoretical instrument could achieve 30 m s^{-1}. This is 6 times worse than the precision achieved by HARPS, and 2 times worse than the precision that could be achieved with CRIRES, scaling the Bean et al. (2010) result.

Clearly, throughput is also important. To be competitive with HARPS, the theoretical instrument would need to a throughput of peak throughput of 50 %, versus TEDI's 1.5 %, and be deployed on a 5 meter-class telescope. To be more
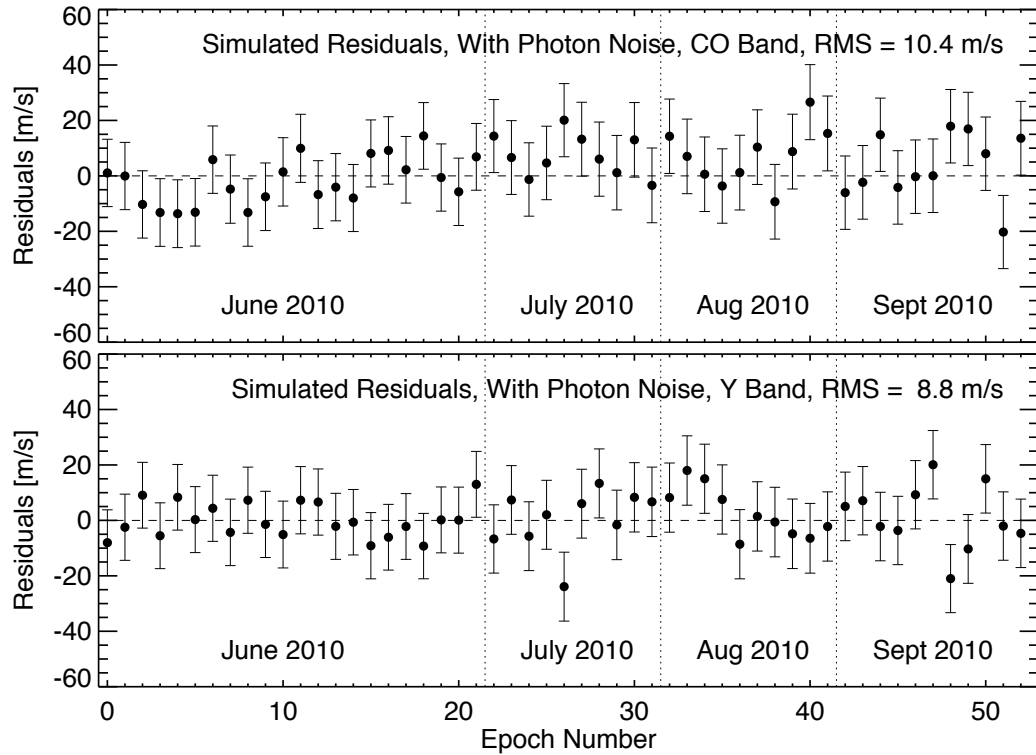
Figure 8.3 – Simulated residuals for a resolution 50000 spectrograph with an interferometer, with barycentric motions matched to the barycentric motions of the TEDI measurements on GJ 699. The simulations include photon noise, assuming 5 minute exposures on GJ 699 with the Palomar 200″ Hale Telescope and 1.5 % throughput at all wavelengths. *Top*: Simulated residuals for the CO band (2.3 to 2.4 μm), with a 4.6 cm delay in the interferometer. *Bottom*: Simulated residuals for the Y band (1.0 to 1.1 μm), with a 2.6 cm delay in the interferometer. Both RMS residuals are consistent with photon noise, and do not show significant effects from mixing with telluric lines.
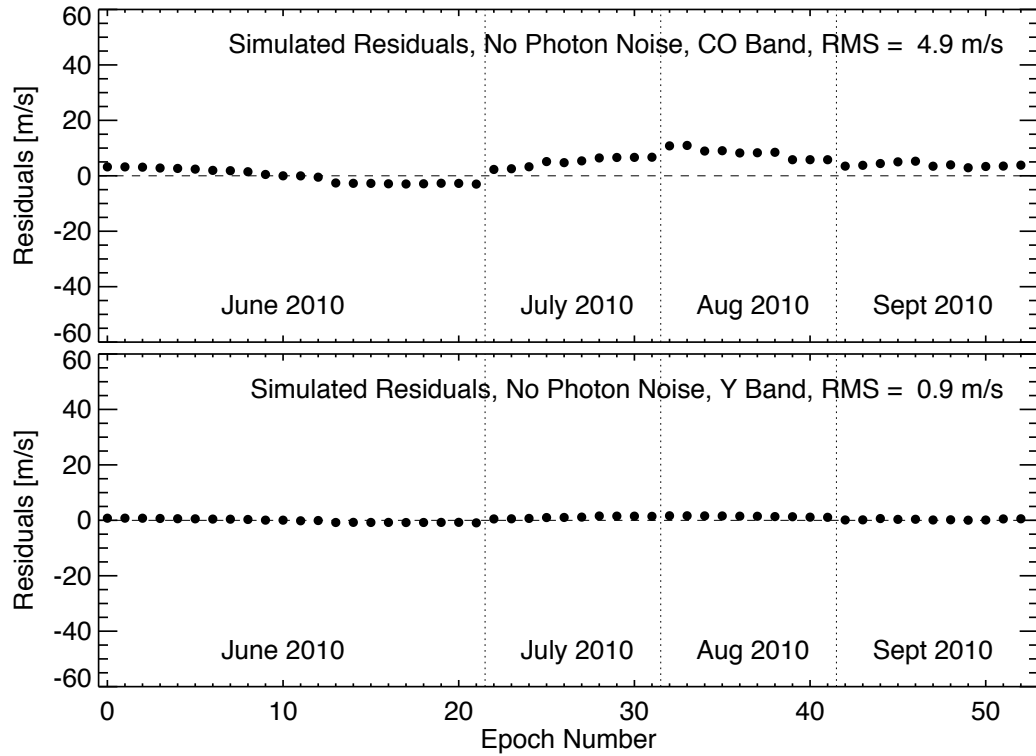
Figure 8.4 – Simulated residuals for a resolution 50000 spectrograph with an interferometer, with barycentric motions matched to the barycentric motions of the TEDI measurements on GJ 699. No noise has been added. *Top*: Simulated residuals for the CO band (2.3 to 2.4 μm), with a 4.6 cm delay in the interferometer. Insufficient removal of telluric lines limits radial velocity RMS precision to 4.9 m s^{-1}, strikingly similar to the limiting performance achieved by Bean et al. (2010) using the same band. *Bottom*: Simulated residuals for the Y band (1.0 to 1.1 μm), with a 2.6 cm delay in the interferometer. Simulated RMS is significantly less than the CO band, with less than 1 m s^{-1} achieved.

efficient that visible-wavelength radial velocity surveys, near-infrared survey will also need more bandwidth. Z band, near 0.9μm, is also a compelling region with little to no telluric contamination. Unfortunately, the telluric models used in my analysis do not include Z band.

To conclude, the results of the TEDI experiment motivate instruments towards higher resolution, operating in spectral regions with little to no telluric interference, with high throughput, and with large bandwidth. With these conditions met, near-infrared radial velocimetry can significantly broaden the capacity for terrestrial exoplanet detection and transit verification.

APPENDIX A

TEDI 2007-2009

Here I describe the results from the first implementation of TEDI, and the experiment which revealed how non-common path errors between the starlight and ThAr calibration source limited radial velocity precision to several km s^{-1}.

TEDI was commissioned in Dec of 2007 on the Hale telescope, and was subsequently awarded a total of 28 nights through the Cornell-Caltech Palomar agreement until Dec of 2009, with roughly half the time lost to bad weather. The nights were used primarily to characterize TEDI performance on bright M dwarfs known to have low radial velocity variation from optical measurements. In this paper, we discuss our results on the star GJ 411. GJ 411 is a nearby, bright (K=3.2) M2 dwarf known to have less than 7.2 m s^{-1} of radial velocity jitter (Endl et al., 2003) and less than 1 km s^{-1} of stellar rotation (Marcy & Chen, 1992), providing narrow lines for precise Doppler measurements.

Observations of GJ 411 showed systematic radial velocity errors which varied as a function of wavelength. To understand these effects, we built a fiber-fed "star simulator" which recreates a telescope beam through TEDI with similar illumination across the entire TripleSpec bandpass. Illuminating the simulator with a Kr gas discharge lamp, we simulated repeated epochs on a star while varying parameters such as telescope pointing and focus. The data analysis, results and discussion follow.

A.1   GJ 411 Results

Attempts to establish the intra-night and night-to-night radial velocity precision of TEDI on GJ 411 revealed systematic RV errors as a function of wavelength which fluctuated quickly with time. Figure A.1 shows three plots of radial velocity versus wavelength for 3 epochs taken back-to-back during the night of April 9th, 2009 (UT). Attempts to understand and correct these fluctuations focused at first on the data analysis. It was not until we built a 'star simulator' telescope allowing for extensive off-telescope tests that we realized the errors were due to variations in the interferometer delays as seen by the star due to seeing and guiding errors.

Nevertheless, an estimate of the radial velocity precision of TEDI was established. Figure A.1 plots the change in radial velocity of GJ 411 between 2 runs separated by one month. The regions of the spectrum dominated by stellar lines report the correct barycentric velocity of the Earth relative to GJ 411 of 16.6 km s^{-1}. Regions dominated by the Earth's telluric lines report 0 km s^{-1} as expected. Using the telluric dominated regions to calibrate the fluctuations, we estimate our night-to-night radial velocity precision to several km s^{-1}.

Initial attempts to simulate starlight through TEDI involved a single CaF_2 lens in a tube with a fiber feed. Simple lenses have inconsistent focal behavior across the bandwidth of TripleSpec, making it difficult to accurately simulate starlight from the telescope. To correct this, we constructed a star simulator telescope consisting of a 4-inch diamond-turned mirror with a fiber feed providing a consistent focus versus wavelength. This proved absolutely necessary to the discovery of TEDI's systematic errors, as they involve both dispersion

111

GJ 411 Radial Velocity vs Wavelength
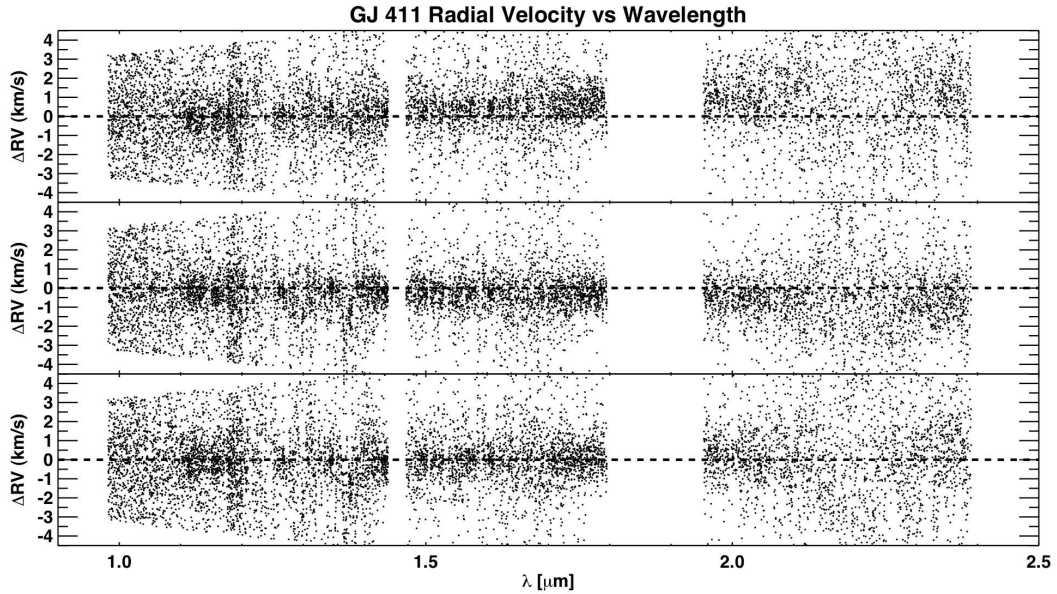
Figure A.1 – Radial Velocity versus wavelength as reported by each TEDI pixel for 3 epochs on GJ 411 taken back to back on the night of April 9th, 2009 (UT). Each epoch required roughly 6 minutes of observing time to complete. As expected, the values scatter about a ΔRV of 0 km s^{-1}, indicated on each plot with a dashed line. However there are clearly km s^{-1} fluctuations above and below 0, and the discrepancies are different for different wavelengths. The barycentric motion of the Earth relative to GJ 411 between these epochs was only 60m s^{-1}, which does not explain the fluctuations. Experiments with a Kr source revealed the errors correlated with seeing and pointing changes through the interferometer.

and focal behavior.

Feeding the star simulator with a Kr gas discharge lamp, we discovered that slightly shifting the Kr beam in the interferometer plane introduced fluctuations identical to those seen in starlight. Shifting the Kr source by the equivalent of one arcsecond introduced roughly a km s^{-1} of radial velocity error. The effect was also produced by sampling different parts of the image plane after the interferometer with TEDI's optical fibers. Figure A.1 plots the change in measured radial velocity introduced by moving the image of the Kr fiber tip by the equiv-

Radial Velocity vs Wavelength measured by TEDI of GJ 411
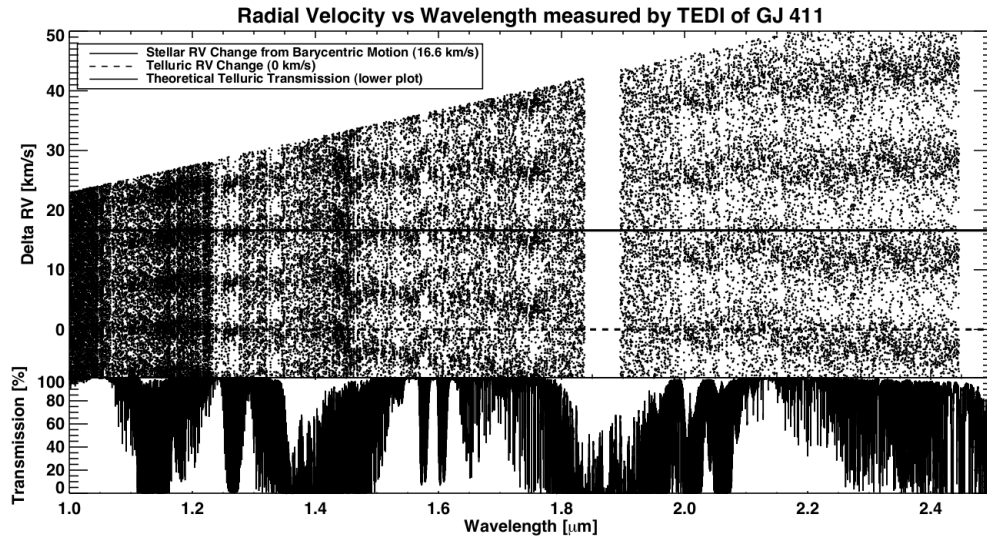
Figure A.2 – Plot showing the difference in measured radial velocity between two TEDI epochs of GJ 411 separated by about one month, along with a model of the telluric transmission lines introduced by the Earth's atmosphere provided by Henry Roe (Roe, 2002). The barycentric motion of the Earth relative to GJ 411 changed by 16.6 km s^{-1}, and the regions dominated by stellar lines report that radial velocity change. Regions dominated by telluric lines report 0 km s^{-1} as expected. The data is plotted several times to account for the 2π degeneracy in the radial velocity. Systematic errors are still present and are clearest in K band, where the values show fluctuate about the expected value.

alent of 0.5 arcseconds on the sky.

Kr Gas Lamp Radial Velocity vs Wavelength, 0.5 arcsecond Shift
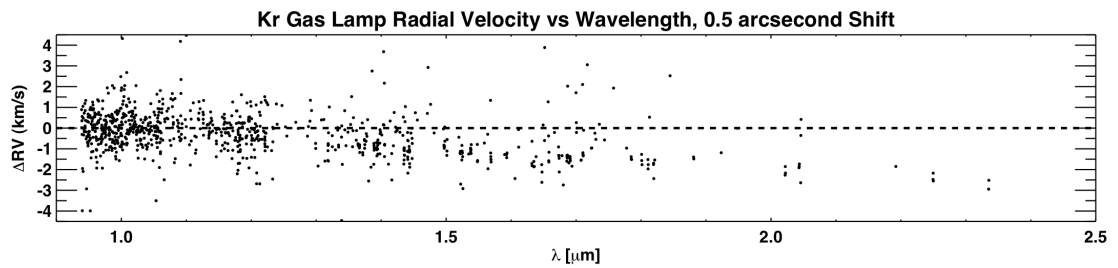
Figure A.3 – Plot showing the difference in measured radial velocity between two TEDI phase sets of a Krypton gas discharge lamp injected into TEDI with an illumination similar to starlight. Between phase sets the star simulator telescope was shifted to simulate a 0.5 arcsecond shift of starlight. The data points are rare longward of 1.5 μm because the Kr lamp has relatively few emission lines in this region. There is a clear deviation from 0 km s^{-1} (indicated in a dashed line) which was an effect isolated to translating the telescope.

Here I describe my algorithms and the IDL code for simulating EDI data.

B.1   Creating the Wavenumber Array

To simulate TEDI data, I first create a wavelength/wavenumber array which is spaced with constant resolution. To calculate the the array, I begin with the definition of a spectrograph's resolution:

$$R = \frac{\lambda}{\Delta\lambda} = \frac{\nu}{\Delta\nu} \tag{B.1}$$

where R is the resolution (2700 for TripleSpec), λ is wavelength, ν is wavenumber and $\Delta\nu$ and $\Delta\lambda$ represent the full-width-at-half-maximum (FWHM) of the spectrograph line-spread function. Solving for $\Delta\nu$, we can rewrite this as a first order ordinary differential equation, versus the array index i:

$$\frac{d\nu}{di} = \frac{\nu}{n_p R} \tag{B.2}$$

where n_p is the pixels per resolution element, or the number of pixels included in the FWHM of the line-spread function. TripleSpec samples the FWHM of the line-spread function with 2.7 pixels. Integrating $d\nu$ from $\nu_{\min}$ to ν, and i from 0 to i, we can solve for $\nu(i)$:

$$\nu(i) = \nu_{\min} \ \exp\frac{i}{n_p R} \tag{B.3}$$

To determine the number of elements needed for a given range from v_{min} to v_{max}, we input v_{max} for v and solve for i, which is i_{max}:

$$i_{max} = n_p \ R \ \ln \frac{v_{max}}{v_{min}} \qquad (B.4)$$

The solution is identical for wavelength, just substitute λ for v. In IDL, I can create an array of wavenumber of wavelength values which roughly match those of pixels for a constant resolution and n_P with the following code:

```
IDL> nu_array = nu_min * exp(dindgen(n_p * R * alog( nu_max /
nu_min )) / (n_p * R))
```

For the simulations used in my dissertation, I begin with a high resolution wavenumber array, nearly matched to the native resolution of the synthetic spectra. This is purely for putting the synthetic spectra onto a constant resolution grid, and not for simulating a spectrograph, so n_p is set to unity.

B.2 Interpolation and Convolution

With an array of nu values separated a constant resolution, I can interpolate a synthetic spectrum onto that array, and convolve the interpolated spectrum by a single kernel to smooth to another resolution. To interpolate a synthetic spectrum, I first create a wavenumber array at a resolution which is higher than the maximum resolution in the synthetic spectrum. I then use a cubic spline interpolation routine to interpolate the spectrum onto that array. I found the most reproducible cubic spline routine in IDL is `cspline`, in the IDL Astronomy

User's Library (Landsman, 1993). The synthetic spectra used in my dissertation have a maximum resolution of between 3×10^5 and 5×10^5.

Once the desired spectrum is interpolated onto the high resolution grid, I can create convolution kernels for smoothing the spectrum due to rotational broadening or from the spectrograph line-spread function. Since the wavenumber array is spaced with constant resolution, I only need a single kernel for smoothing the entire spectrum. The rotational kernel is calculated using the Astronomy IDL routine `lsf_rotate`, with the following code:

```
IDL> rotation_kernel = lsf_rotate( 3d5 / R , vsini )
```

where `R` is the resolution of the wavenumber array, `vsini` is the desired rotational broadening in km s^{-1}, and `3d5 / R` is the spacing of the kernel array in km s^{-1}.

To make a convolution kernel for the line-spread function of the spectrograph, I use a Gaussian. The FWHM in units of array index is given by the ratio of the resolution of the current wavenumber array to the resolution of the line-spread function. With this, a Gaussian is created using the Astronomy IDL routine `psf_gaussian`:

```
IDL> LSF = psf_gaussian( fwhm = R / R_LSF , npixel = 4 * R /
R_LSF )
```

Once convolved with the line-spread function of the simulated spectrograph, the spectrum is interpolated onto a new wavenumber grid with the resolution and n_P of the simulated spectrograph. Convolution of the synthetic spectrum with the rotational kernel and the line-spread function is performed in the

strict mathematical sense using the IDL routine `convol`. It is then scaled to a given signal-to-noise and noise can be added if desired.

BIBLIOGRAPHY

Agol, E., Cowan, N. B., Knutson, H. A., Deming, D., Steffen, J. H., Henry, G. W., & Charbonneau, D. 2010, ApJ , 721, 1861

Barnes, J. R., Jeffers, S. V., & Jones, H. R. A. 2010, ArXiv e-prints

Baudrand, J. & Walker, G. A. H. 2001, PASP , 113, 851

Bayes, T. & Price, R. 1763, Philosophical Transactions of the Royal Society of London, 53, 370

Bean, J. L., Seifahrt, A., Hartman, H., Nilsson, H., Wiedemann, G., Reiners, A., Dreizler, S., & Henry, T. J. 2010, ApJ , 713, 410

Behr, B. B., Hajian, A. R., Cenko, A. T., Murison, M., McMillan, R. S., Hindsley, R., & Meade, J. 2009, ApJ , 705, 543

Blake, C. H., Charbonneau, D., & White, R. J. 2010, ApJ , 723, 684

Brown, T. M., Charbonneau, D., Gilliland, R. L., Noyes, R. W., & Burrows, A. 2001, ApJ , 552, 699

Browning, M. K., Basri, G., Marcy, G. W., West, A. A., & Zhang, J. 2010, AJ , 139, 504

Burns, J. A. The evolution of satellite orbits, ed. Burns, J. A. & Matthews, M. S., 117–158

Burrows, A., Guillot, T., Hubbard, W. B., Marley, M. S., Saumon, D., Lunine, J. I., & Sudarsky, D. 2000, ApJL , 534, L97

Burrows, A., Hubeny, I., Budaj, J., & Hubbard, W. B. 2007, ApJ , 661, 502

Butler, R. P., Marcy, G. W., Williams, E., McCarthy, C., Dosanjh, P., & Vogt, S. S. 1996, PASP , 108, 500

Butler, R. P., Vogt, S. S., Marcy, G. W., Fischer, D. A., Wright, J. T., Henry, G. W., Laughlin, G., & Lissauer, J. J. 2004, ApJ , 617, 580

Chabrier, G. 2003, PASP , 115, 763

Charbonneau, D. 2009, in IAU Symposium, Vol. 253, IAU Symposium, 1–8

Charbonneau, D., Berta, Z. K., Irwin, J., Burke, C. J., Nutzman, P., Buchhave, L. A., Lovis, C., Bonfils, X., Latham, D. W., Udry, S., Murray-Clay, R. A., Holman, M. J., Falco, E. E., Winn, J. N., Queloz, D., Pepe, F., Mayor, M., Delfosse, X., & Forveille, T. 2009, Nature , 462, 891

Charbonneau, D., Brown, T. M., Latham, D. W., & Mayor, M. 2000, ApJL , 529, L45

Charbonneau, D., Brown, T. M., Noyes, R. W., & Gilliland, R. L. 2002, ApJ , 568, 377

Charbonneau, D. & Deming, D. 2007, ArXiv e-prints

Cox, A. N. 2004, Allen's Astrophysical Quantities, Fourth Edition, ed. A. N. Cox

Crockett, C. J., Mahmud, N. I., Prato, L., Johns-Krull, C. M., Jaffe, D. T., & Beichman, C. A. 2011, ArXiv e-prints

Cumming, A. & Dragomir, D. 2010, MNRAS , 401, 1029

Cumming, A., Marcy, G. W., Butler, R. P., & Vogt, S. S. 2003, in Astronomical Society of the Pacific Conference Series, Vol. 294, Scientific Frontiers in Research on Extrasolar Planets, ed. D. Deming & S. Seager, 27–30

Edelstein, J., Muirhead, P., Wright, J., Covey, K., Erskine, D., Muterspaugh, M., Lloyd, J., Halverson, S., Marckwordt, M., & Mondo, D. 2010, in Society of Photo-Optical Instrumentation Engineers (SPIE) Conference Series, Vol. 7735, Society of Photo-Optical Instrumentation Engineers (SPIE) Conference Series

Endl, M., Cochran, W. D., Tull, R. G., & MacQueen, P. J. 2003, AJ , 126, 3099

Erskine, D. J. 2003, PASP , 115, 255

Evans, D. S. 1996, VizieR Online Data Catalog, 3047, 0

Figueira, P., Pepe, F., Melo, C. H. F., Santos, N. C., Lovis, C., Mayor, M., Queloz, D., Smette, A., & Udry, S. 2010, A&A , 511, A55+

Fischer, D. A. & Valenti, J. 2005, ApJ , 622, 1102

Fuhrmeister, B., Schmitt, J. H. M. M., & Hauschildt, P. H. 2005, A&A , 439, 1137

Gaidos, E., Haghighipour, N., Agol, E., Latham, D., Raymond, S., & Rayner, J. 2007, Science, 318, 210

Garnett, J. D. & Forrest, W. J. 1993, in Society of Photo-Optical Instrumentation Engineers (SPIE) Conference Series, Vol. 1946, Society of Photo-Optical Instrumentation Engineers (SPIE) Conference Series, ed. A. M. Fowler, 395–404

Ge, J., van Eyken, J., Mahadevan, S., DeWitt, C., Kane, S. R., Cohen, R., Vanden Heuvel, A., Fleming, S. W., Guo, P., Henry, G. W., Schneider, D. P., Ramsey, L. W., Wittenmyer, R. A., Endl, M., Cochran, W. D., Ford, E. B., Martín, E. L., Israelian, G., Valenti, J., & Montes, D. 2006, ApJ , 648, 683

Gillon, M., Pont, F., Demory, B., Mallmann, F., Mayor, M., Mazeh, T., Queloz, D., Shporer, A., Udry, S., & Vuissoz, C. 2007, A&A , 472, L13

Gliese, W. & Jahreiss, H. 1991, NASA STI/Recon Technical Report A, 92, 33932

Goldreich, P. & Tremaine, S. 1980, ApJ , 241, 425

Gregory, P. C. 2005, ApJ , 631, 1198

Hajian, A. R., Behr, B. B., Cenko, A. T., Olling, R. P., Mozurkewich, D., Armstrong, J. T., Pohl, B., Petrossian, S., Knuth, K. H., Hindsley, R. B., Murison, M., Efroimsky, M., Dantowitz, R., Kozubal, M., Currie, D. G., Nordgren, T. E., Tycner, C., & McMillan, R. S. 2007, ApJ , 661, 616

Henry, G. W., Marcy, G. W., Butler, R. P., & Vogt, S. S. 2000, ApJL , 529, L41

Herter, T. L., Henderson, C. P., Wilson, J. C., Matthews, K. Y., Rahmer, G., Bonati, M., Muirhead, P. S., Adams, J. D., Lloyd, J. P., Skrutskie, M. F., Moon, D., Parshley, S. C., Nelson, M. J., Martinache, F., & Gull, G. E. 2008, in Society of Photo-Optical Instrumentation Engineers (SPIE) Conference Series, Vol. 7014, Society of Photo-Optical Instrumentation Engineers (SPIE) Conference Series

Hillenbrand, L. A., Foster, J. B., Persson, S. E., & Matthews, K. 2002, PASP , 114, 708

Howard, A. W., Marcy, G. W., Bryson, S. T., Jenkins, J. M., Rowe, J. F., Batalha, N. M., Borucki, W. J., Koch, D. G., Dunham, E. W., Gautier, III, T. N., Van Cleve, J., Cochran, W. D., Latham, D. W., Lissauer, J. J., Torres, G., Brown, T. M., Gilliland, R. L., Buchhave, L. A., Caldwell, D. A., Christensen-Dalsgaard, J., Ciardi, D., Fressin, F., Haas, M. R., Howell, S. B., Kjeldsen, H., Seager, S., Rogers, L., Sasselov, D. D., Steffen, J. H., Basri, G. S., Charbonneau, D., Christiansen, J., Clarke, B., Dupree, A., Fabrycky, D. C., Fischer, D. A., Ford, E. B., Fortney, J. J., Tarter, J., Girouard, F. R., Holman, M. J., Johnson, J. A., Klaus, T. C., Machalek, P., Moorhead, A. V., Morehead, R. C., Ragozzine,

D., Tenenbaum, P., Twicken, J. D., Quinn, S. N., Isaacson, H., Shporer, A., Lucas, P. W., Walkowicz, L. M., Welsh, W. F., Boss, A., Devore, E., Gould, A., Smith, J. C., Morris, R. L., Prsa, A., & Morton, T. D. 2011, ArXiv e-prints

Howard, A. W., Marcy, G. W., Johnson, J. A., Fischer, D. A., Wright, J. T., Isaacson, H., Valenti, J. A., Anderson, J., Lin, D. N. C., & Ida, S. 2010, Science, 330, 653

Huélamo, N., Figueira, P., Bonfils, X., Santos, N. C., Pepe, F., Gillon, M., Azevedo, R., Barman, T., Fernández, M., di Folco, E., Guenther, E. W., Lovis, C., Melo, C. H. F., Queloz, D., & Udry, S. 2008, A&A , 489, L9

Hunter, T. R. & Ramsey, L. W. 1992, PASP , 104, 1244

Jeffreys, H. 1945, Proceedings of the Royal Society of London. Series A, Mathematical and Physical Sciences, 186, 453

Jenkins, J. S., Ramsey, L. W., Jones, H. R. A., Pavlenko, Y., Gallardo, J., Barnes, J. R., & Pinfield, D. J. 2009, ApJ , 704, 975

Johnson, J. A., Aller, K. M., Howard, A. W., & Crepp, J. R. 2010, PASP , 122, 905

Johnson, J. A. & Apps, K. 2009, ApJ , 699, 933

Johnson, J. A., Butler, R. P., Marcy, G. W., Fischer, D. A., Vogt, S. S., Wright, J. T., & Peek, K. M. G. 2007, ApJ , 670, 833

Jones, H. R. A., Rayer, J., Ramsey, L., Dent, B., Longmore, A., Vacca, B., Liu, M., Webster, A., Wolscznan, A., & Barnes, J. 2009, in Science with the VLT in the ELT Era, ed. A. Moorwood, 415–+

Jones, H. R. A., Rayner, J., Ramsey, L., Henry, D., Dent, B., Montgomery, D., Vick, A., Ives, D., Egan, I., Lunney, D., Rees, P., Webster, A., Tinney, C., & Liu,

M. 2008, in Presented at the Society of Photo-Optical Instrumentation Engineers (SPIE) Conference, Vol. 7014, Society of Photo-Optical Instrumentation Engineers (SPIE) Conference Series

Kaeufl, H.-U., Ballester, P., Biereichel, P., Delabre, B., Donaldson, R., Dorn, R., Fedrigo, E., Finger, G., Fischer, G., Franza, F., Gojak, D., Huster, G., Jung, Y., Lizon, J.-L., Mehrgan, L., Meyer, M., Moorwood, A., Pirard, J.-F., Paufique, J., Pozna, E., Siebenmorgen, R., Silber, A., Stegmeier, J., & Wegerer, S. 2004, in Presented at the Society of Photo-Optical Instrumentation Engineers (SPIE) Conference, Vol. 5492, Society of Photo-Optical Instrumentation Engineers (SPIE) Conference Series, ed. A. F. M. Moorwood & M. Iye, 1218–1227

Kasting, J. F., Whitmire, D. P., & Reynolds, R. T. 1993, Icarus, 101, 108

Kerber, F., Nave, G., & Sansonetti, C. J. 2008, ApJS , 178, 374

Knutson, H. A., Charbonneau, D., Allen, L. E., Fortney, J. J., Agol, E., Cowan, N. B., Showman, A. P., Cooper, C. S., & Megeath, S. T. 2007, Nature , 447, 183

Koch, D. G., Borucki, W. J., Basri, G., Batalha, N. M., Brown, T. M., Caldwell, D., Christensen-Dalsgaard, J., Cochran, W. D., DeVore, E., Dunham, E. W., Gautier, T. N., Geary, J. C., Gilliland, R. L., Gould, A., Jenkins, J., Kondo, Y., Latham, D. W., Lissauer, J. J., Marcy, G., Monet, D., Sasselov, D., Boss, A., Brownlee, D., Caldwell, J., Dupree, A. K., Howell, S. B., Kjeldsen, H., Meibom, S., Morrison, D., Owen, T., Reitsema, H., Tarter, J., Bryson, S. T., Dotson, J. L., Gazis, P., Haas, M. R., Kolodziejczak, J., Rowe, J. F., Van Cleve, J. E., Allen, C., Chandrasekaran, H., Clarke, B. D., Li, J., Quintana, E. V., Tenenbaum, P., Twicken, J. D., & Wu, H. 2010, ApJL , 713, L79

Landsman, W. B. 1993, in Astronomical Society of the Pacific Conference

Series, Vol. 52, Astronomical Data Analysis Software and Systems II, ed. R. J. Hanisch, R. J. V. Brissenden, & J. Barnes, 246–+

Laplace, P. S. 1774, Mémoires de mathématique et de physique presentés à l'Académie royale des sciences, par divers savans, & lûs dan ses assemblées, 6, 621

Lin, D. N. C. & Papaloizou, J. 1986, ApJ , 309, 846

Lovis, C., Pepe, F., Bouchy, F., Lo Curto, G., Mayor, M., Pasquini, L., Queloz, D., Rupprecht, G., Udry, S., & Zucker, S. 2006, in Society of Photo-Optical Instrumentation Engineers (SPIE) Conference Series, Vol. 6269, Society of Photo-Optical Instrumentation Engineers (SPIE) Conference Series

Lovis, C., Ségransan, D., Mayor, M., Udry, S., Benz, W., Bertaux, J., Bouchy, F., Correia, A. C. M., Laskar, J., Lo Curto, G., Mordasini, C., Pepe, F., Queloz, D., & Santos, N. C. 2011, A&A , 528, A112+

Lunine, J. I., Macintosh, B., & Peale, S. 2009, Physics Today, 62, 050000

Mahadevan, S., Ramsey, L., Wright, J., Endl, M., Redman, S., Bender, C., Roy, A., Zonak, S., Troupe, N., Engel, L., Sigurdsson, S., Wolszczan, A., & Zhao, B. 2010, in Society of Photo-Optical Instrumentation Engineers (SPIE) Conference Series, Vol. 7735, Society of Photo-Optical Instrumentation Engineers (SPIE) Conference Series

Marcy, G., Butler, R. P., Fischer, D., Vogt, S., Wright, J. T., Tinney, C. G., & Jones, H. R. A. 2005, Progress of Theoretical Physics Supplement, 158, 24

Marcy, G. W. & Chen, G. H. 1992, ApJ , 390, 550

Martinache, F., Rojas-Ayala, B., Ireland, M. J., Lloyd, J. P., & Tuthill, P. G. 2009, ApJ , 695, 1183

Masset, F. S. & Papaloizou, J. C. B. 2003, ApJ , 588, 494

Miller, A. A., Hillenbrand, L. A., Covey, K. R., Poznanski, D., Silverman, J. M., Kleiser, I. K. W., Rojas-Ayala, B., Muirhead, P. S., Cenko, S. B., Bloom, J. S., Kasliwal, M. M., Filippenko, A. V., Law, N. M., Ofek, E. O., Dekany, R. G., Rahmer, G., Hale, D., Smith, R., Quimby, R. M., Nugent, P., Jacobsen, J., Zolkower, J., Velur, V., Walters, R., Henning, J., Bui, K., McKenna, D., Kulkarni, S. R., Klein, C. R., Kandrashoff, M., & Morton, A. 2011, ApJ , 730, 80

Miller-Ricci, E. & Fortney, J. J. 2010, ApJL , 716, L74

Monnier, J. D., Zhao, M., Pedretti, E., Thureau, N., Ireland, M., Muirhead, P., Berger, J., Millan-Gabet, R., Van Belle, G., ten Brummelaar, T., McAlister, H., Ridgway, S., Turner, N., Sturmann, L., Sturmann, J., & Berger, D. 2007, Science, 317, 342

Muirhead, P. S., Edelstein, J., Wright, J. T., Erskine, D. J., Muterspaugh, M. W., Covey, K. R., Marckwordt, M. R., Halverson, S., Mondo, D., & Lloyd, J. P. 2010, in Society of Photo-Optical Instrumentation Engineers (SPIE) Conference Series, Vol. 7735, Society of Photo-Optical Instrumentation Engineers (SPIE) Conference Series

Nutzman, P. & Charbonneau, D. 2008, PASP , 120, 317

Oppenheimer, B. R., Golimowski, D. A., Kulkarni, S. R., Matthews, K., Nakajima, T., Creech-Eakman, M., & Durrance, S. T. 2001, AJ , 121, 2189

Pavlenko, Y. V., Jones, H. R. A., Lyubchik, Y., Tennyson, J., & Pinfield, D. J. 2006, A&A , 447, 709

Peale, S. J. 1977, in IAU Colloq. 28: Planetary Satellites, ed. J. A. Burns, 87–111

Pollack, J. B., Hubickyj, O., Bodenheimer, P., Lissauer, J. J., Podolak, M., & Greenzweig, Y. 1996, Icarus, 124, 62

Prato, L., Huerta, M., Johns-Krull, C. M., Mahmud, N., Jaffe, D. T., & Hartigan, P. 2008, ApJL , 687, L103

Press, W. H. & Rybicki, G. B. 1989, ApJ , 338, 277

Quirrenbach, A., Amado, P. J., Mandel, H., Caballero, J. A., Mundt, R., Ribas, I., Reiners, A., Abril, M., Aceituno, J., Afonso, C., Barrado Y Navascues, D., Bean, J. L., Béjar, V. J. S., Becerril, S., Böhm, A., Cárdenas, M. C., Claret, A., Colomé, J., Costillo, L. P., Dreizler, S., Fernández, M., Francisco, X., Galadí, D., Garrido, R., González Hernández, J. I., Guàrdia, J., Guenther, E. W., Gutiérrez-Soto, F., Joergens, V., Hatzes, A. P., Helmling, J., Henning, T., Herrero, E., Kürster, M., Laun, W., Lenzen, R., Mall, U., Martin, E. L., Martín-Ruiz, S., Mirabet, E., Montes, D., Morales, J. C., Morales Muñoz, R., Moya, A., Naranjo, V., Rabaza, O., Ramón, A., Rebolo, R., Reffert, S., Rodler, F., Rodríguez, E., Rodríguez Trinidad, A., Rohloff, R. R., Sánchez Carrasco, M. A., Schmidt, C., Seifert, W., Setiawan, J., Solano, E., Stahl, O., Storz, C., Suárez, J. C., Thiele, U., Wagner, K., Wiedemann, G., Zapatero Osorio, M. R., Del Burgo, C., Sánchez-Blanco, E., & Xu, W. 2010, in Society of Photo-Optical Instrumentation Engineers (SPIE) Conference Series, Vol. 7735, Society of Photo-Optical Instrumentation Engineers (SPIE) Conference Series

Ramsey, L. W., Barnes, J., Redman, S. L., Jones, H. R. A., Wolszczan, A., Bongiorno, S., Engel, L., & Jenkins, J. 2008, PASP , 120, 887

Reid, I. N. & Cruz, K. L. 2002, AJ , 123, 2806

Reid, I. N., Hawley, S. L., & Gizis, J. E. 1995, AJ , 110, 1838

Reiners, A. 2009, A&A , 498, 853

Rieke, G. 2002, Detection of Light: from the Ultraviolet to the Submillimeter, Second Edition, ed. Rieke, G.

Roe, H. G. 2002, PhD thesis, UNIVERSITY OF CALIFORNIA, BERKELEY

Rogers, L. A. & Seager, S. 2010, ApJ , 716, 1208

Rojas-Ayala, B., Covey, K. R., Muirhead, P. S., & Lloyd, J. P. 2010, ApJL , 720, L113

Royer, F., Zorec, J., & Gómez, A. E. 2007, A&A , 463, 671

Saar, S. H., Butler, R. P., & Marcy, G. W. 1998, ApJL , 498, L153+

Saar, S. H. & Donahue, R. A. 1997, ApJ , 485, 319

Santos, N. C., Israelian, G., & Mayor, M. 2001, A&A , 373, 1019

Sato, B., Fischer, D. A., Henry, G. W., Laughlin, G., Butler, R. P., Marcy, G. W., Vogt, S. S., Bodenheimer, P., Ida, S., Toyota, E., Wolf, A., Valenti, J. A., Boyd, L. J., Johnson, J. A., Wright, J. T., Ammons, M., Robinson, S., Strader, J., McCarthy, C., Tah, K. L., & Minniti, D. 2005, ApJ , 633, 465

Seager, S. & Sasselov, D. D. 2000, ApJ , 537, 916

Setiawan, J., Henning, T., Launhardt, R., Müller, A., Weise, P., & Kürster, M. 2008, Nature , 451, 38

Shannon, R. M. & Cordes, J. M. 2010, ApJ , 725, 1607

Simcoe, R. A., Burgasser, A. J., Bochanski, J. J., Schechter, P. L., Bernstein, R. A., Bigelow, B. C., Pipher, J. L., Forrest, W., McMurtry, C., Smith, M. J., & Fishner, J. 2010, in Society of Photo-Optical Instrumentation Engineers (SPIE) Conference Series, Vol. 7735, Society of Photo-Optical Instrumentation Engineers (SPIE) Conference Series

Skrutskie, M. F., Cutri, R. M., Stiening, R., Weinberg, M. D., Schneider, S., Carpenter, J. M., Beichman, C., Capps, R., Chester, T., Elias, J., Huchra, J., Liebert, J., Lonsdale, C., Monet, D. G., Price, S., Seitzer, P., Jarrett, T., Kirkpatrick, J. D., Gizis, J. E., Howard, E., Evans, T., Fowler, J., Fullmer, L., Hurt, R., Light, R., Kopan, E. L., Marsh, K. A., McCallon, H. L., Tam, R., Van Dyk, S., & Wheelock, S. 2006, AJ , 131, 1163

Snellen, I. A. G., de Kok, R. J., de Mooij, E. J. W., & Albrecht, S. 2010, Nature , 465, 1049

Stigler, S. M. 1986, Statistical Science, 1, 359

Swain, M. R., Vasisht, G., & Tinetti, G. 2008, Nature , 452, 329

Udry, S., Mayor, M., & Santos, N. C. 2003, A&A , 407, 369

Vacca, W. D., Cushing, M. C., & Rayner, J. T. 2003, PASP , 115, 389

van Eyken, J. C., Ge, J., & Mahadevan, S. 2010, ApJS , 189, 156

Walkowicz, L. M. & Hawley, S. L. 2009, AJ , 137, 3297

Ward, W. R. 1997, ApJL , 482, L211+

West, A. A., Hawley, S. L., Walkowicz, L. M., Covey, K. R., Silvestri, N. M., Raymond, S. N., Harris, H. C., Munn, J. A., McGehee, P. M., Ivezić, Ž., & Brinkmann, J. 2004, AJ , 128, 426

Wielen, R., Jahreiß, H., & Krüger, R. 1983, in IAU Colloq. 76: Nearby Stars and the Stellar Luminosity Function, ed. A. G. D. Philip & A. R. Upgren, 163–170

Wilson, J. C., Henderson, C. P., Herter, T. L., Matthews, K., Skrutskie, M. F., Adams, J. D., Moon, D., Smith, R., Gautier, N., Ressler, M., Soifer, B. T., Lin, S., Howard, J., LaMarr, J., Stolberg, T. M., & Zink, J. 2004, in Society of Photo-Optical Instrumentation Engineers (SPIE) Conference Series, Vol. 5492, Society of Photo-Optical Instrumentation Engineers (SPIE) Conference Series, ed. A. F. M. Moorwood & M. Iye, 1295–1305

Wright, J. T. 2005, PASP , 117, 657

Wright, J. T. & Howard, A. W. 2009, ApJS , 182, 205

Zapolsky, H. S. & Salpeter, E. E. 1969, ApJ , 158, 809

Zhao, B., Ge, J., & Groot, J. 2009, in Society of Photo-Optical Instrumentation Engineers (SPIE) Conference Series, Vol. 7440, Society of Photo-Optical Instrumentation Engineers (SPIE) Conference Series